

SIMULATION BASED ANALYSIS OF A SEASONAL THERMAL STORAGE SYSTEM USING PCM

von

Heinz Stefan Moisi, BSc

als Masterarbeit der Kommission zur Abhaltung der
Masterprüfung der Studienrichtung Maschinenbau an der
Technischen Universität Graz über das Institut für Wärmetechnik
vorgelegt.

Betreuer:

Dipl.-Ing. Christoph Moser

Dipl.-Ing. Dr.mont. Hermann Schranzhofer

Beurteiler:

Ao. Univ.-Prof. Dipl.-Ing. Dr. techn. René Rieberer

Graz, April 2014

STATUTORY DECLARATION

I declare that I have authored this thesis independently, that I have not used other than the declared sources / resources, and that I have explicitly marked all material which has been quoted either literally or by content from the used sources.

Graz,

.....

(Signature)

Eidstattliche Erklärung

Ich erkläre an Eides statt, dass ich die vorliegende Arbeit selbstständig verfasst, andere als die angegebenen Quellen/Hilfsmittel nicht benutzt, und die den benutzten Quellen wörtlich und inhaltlich entnommenen Stellen als solche kenntlich gemacht habe.

Graz am,

.....

(Unterschrift)

ABSTRACT

Title: Simulation based analysis of a seasonal thermal storage system using PCM

Author: Heinz Stefan Moisi

1st keyword: Thermal Energy Storage

2nd keyword: Phase Change Material

3rd keyword: Energy and Exergy Analysis

Seasonal solar thermal systems provide a possibility to increase the fraction of sustainable energy within the building sector. In order to compensate the gap between solar supply and space heating and/or domestic hot water demand, large storage volumes up to 50 m³ and more are required, especially in seasonal applications. Therefore new, more compact storage technologies are desired. In this work, first performance estimations of a storage concept considering the phase change material (PCM) "Sodium Acetate Trihydrate" ($NaCH_3COO \cdot 3H_2O$) as storage medium in a systems context had been carried out. The transient calculations had been performed with the simulation environment TRNSYS 17.1. In terms of comparison, a conventional solar thermal system (including a conventional water storage) had been set up and analysed energetically and exergetically. The heat conversion of the solar collector field has been identified as the dominant loss factor both energetically and exergetically. On basis of the defined reference system three different integration strategies for the considered PCM storage concept had been investigated. In this regard an estimation of the PCM system behaviour in a solar thermal systems context could be given, improvement potentials could be shown and basic design recommendations could be made for further development.

KURZFASSUNG

Titel: Simulations unterstützte Analyse eines PCM- Energiespeichersystems für saisonale Anwendungen

Autor: Heinz Stefan Moisi

1. Stichwort: Thermischer Energiespeicher
2. Stichwort: Phasenwechsel-Material
3. Stichwort: Energie- und Exergieanalyse

Saisonale solar-thermische Systeme stellen eine Möglichkeit zur Steigerung des Anteils an erneuerbaren Energien im Gebäudesektor dar. Speziell bei saisonalen Anwendungen sind sehr große Speichervolumina (bis zu 50 m^3 und mehr) notwendig um die Diskrepanz zwischen Energiebereitstellung und Energieabnahme zu überbrücken. Daher sind neue, kompaktere thermische Speicherkonzepte erforderlich. Diese Masterarbeit dient als erste Abschätzung eines Phasenwechselmaterial basierten Speicherkonzeptes im Hinblick auf Systemeffizienz und Integrationsmöglichkeiten. Als Phasenwechselmaterial ist "Natrium Acetat Trihydrat" ($\text{NaCH}_3\text{COO}\cdot 3\text{H}_2\text{O}$) betrachtet worden. Die dafür erforderlichen Berechnungen wurden mit der Simulationsumgebung TRNSYS 17.1 durchgeführt. Für Vergleichszwecke wurde ein konventionelles Solar-thermisches System aufgebaut, simuliert und analysiert. Dabei konnte die Energieumwandlung im Solarkollektor als dominanter Verlustfaktor, sowohl energetisch als auch exergetisch, identifiziert werden. Auf Basis des Referenzsystems wurden drei grundlegende Einbindungsvarianten des PCM-Speichersystems untersucht. Daraufhin konnte das Verhalten des PCM- Speichers in einem solar thermischen System abgeschätzt, Verbesserungspotenziale aufgezeigt und grundlegende Empfehlungen für die weitere Konzeptionierung in Hinblick auf die Systemintegration gegeben werden.

PREFACE

I would really like to thank Christoph Moser for the great support in any regard during this work. Furthermore I would like to thank Hermann Schranzhofer for his guidance and advice during the past couple of years.

Most of all I want to thank my parents, Erna and Heinrich, for their support and patience throughout my studying. Without them this thesis would not exist. I also want to thank my sister Gabriela for helping me anytime.

CONTENTS

1	INTRODUCTION	1
1.1	Motivation and definition of objectives	1
1.2	State of the art	2
1.3	Procedural method	3
2	BASICS	5
2.1	Fundamental relations	5
2.1.1	Conservation of mass	5
2.1.2	First law of thermodynamics	5
2.1.3	Second law of thermodynamics	6
2.2	Exergy	8
2.2.1	General aspects of exergy	8
2.2.2	The reference environment	9
2.2.3	Exergy assessment of common energy forms	9
2.2.4	Exergy of solar radiation	10
2.2.5	Exergy of a phase change	12
2.2.6	Exergy balance and application	13
2.3	Component models and exergetic analysis	14
2.3.1	Solar flat plate collector	14
2.3.2	Conventional thermal storage with auxiliary heater	17
2.3.3	PCM storage system	21
2.3.4	Counter flow heat exchanger	28
2.3.5	Radiator	31
2.3.6	Hydraulics	34
2.4	Performance indicators	39
2.4.1	Energetic and exergetic efficiency	39
2.4.2	Storage density	41
2.4.3	Solar fraction and penalty functions	42
2.5	Simulation tool TRNSYS 17.1	43
2.5.1	Simulation Studio and TRNSYS-types	43
2.5.2	The EQUATION statement	45
2.5.3	Loads and structures with TRNBUILD	45
3	GENERAL ASPECTS AND BOUNDARY CONDITIONS	47
3.1	The reference building	47
3.1.1	Single family house	47
3.1.2	Domestic hot water demand and internal gains	49
3.2	Climate data and reference state	52
3.3	The phase change material	53
3.4	Simulation parameters and difficulties	56
3.4.1	Numerical stability problems	56
3.4.2	Problems in exergy calculations	58
4	THE REFERENCE SYSTEM	60
4.1	Solar unit	60
4.2	Domestic hot water supply	64
4.3	Space heating	66

4.4	Water based thermal energy storage	69
4.5	Results of the reference system	72
4.5.1	Quality of results	72
4.5.2	Energy and exergy considerations	73
4.5.3	Performance indicators	82
5	PCM SYSTEMS	91
5.1	The PCM storage	91
5.2	Version A: Direct integration	93
5.2.1	Results of Version A	95
5.3	Version B: Auxiliary water storage	98
5.3.1	Results of Version B	100
5.4	Version C: Auxiliary water storage and bypass	106
5.4.1	Results of Version C	108
6	CONCLUSION	113
	LITERATURE	115
	LIST OF FIGURES	118
	LIST OF TABLES	121
	A APPENDIX	122

NOMENCLATURE

Symbols

<p>A Area</p> <p>a parameter</p> <p>a_0 optical efficiency collector</p> <p>a_1 linear loss factor</p> <p>a_2 quadratic loss factor</p> <p>c specific heat capacity, flow velocity</p> <p>C heat capacity</p> <p>\dot{C} heat capacity flux</p> <p>$c_{w,FR}$ wind dependent factor for irradiation</p> <p>$c_{w,hl}$ wind dependent HTC</p> <p>d diameter</p> <p>d_{dp} parameter</p> <p>e specific exergy, external energy</p> <p>E Exergy, external energy</p> <p>\dot{E} exergy rate</p> <p>F factor</p> <p>f function of, factor</p> <p>f_{sol} solar fraction</p> <p>g gravity constant, solar transmittance</p> <p>G solar irradiation</p> <p>h specific enthalpy</p> <p>H enthalpy, height</p> <p>I irreversibility</p> <p>\dot{I} irreversibility rate</p> <p>K factor</p> <p>L length</p> <p>L^0 luminance of a black body</p>	<p>m mass</p> <p>\dot{m} mass flow</p> <p>N number of</p> <p>n radiator exponent</p> <p>NTU number of transfer units</p> <p>P power</p> <p>p pressure</p> <p>Q thermal energy</p> <p>\dot{Q} heat flux</p> <p>\dot{q} specific heat flux</p> <p>S Entropy, storage density</p> <p>s specific entropy, wall thickness</p> <p>T temperature in K</p> <p>U internal energy, heat transfer coefficient</p> <p>u specific internal energy</p> <p>u_w wind velocity</p> <p>v specific volume</p> <p>V Volume</p> <p>W work, width</p> <p>w specific work</p> <p>x position, penalty exponent</p> <p>z potential, distance</p> <p>Z weighted distance</p>
---	---

Greek letters

α	optical absorbtance, heat transfer coefficient internal and external flow
β	collector tilt angle
δ	general variation, mathematical switch, control signal
Δ	difference
Σ	sum
ε	heat exchanger effectiveness, mathematical switch
η	energetic efficiency
λ	thermal conductivity
μ	chemical potential
ψ	exergetic efficiency
ρ	density
σ	Stefan-Boltzmann constant
τ	time, optical transmittance
θ	incidence angle
ϑ	temperature in °C
ξ	mathematical switch

Subscripts and abbreviations

0	state 0, reference state, solar radiation	j	number of node, fluxes etc.
1	state 1, number 1	k	number of nodes
2	state 2, number 2	l	liquid
3	state 3, number 3	L	loss
362	Type 362	lat	latent
805	Type 805	lg	logarithmic
a	external, outside	low	lower limit
A	Case A	m	mean
act	actual	max	maximum
amb	ambient	med	medium
ap	arperture	$melt$	melting area or point
aux	auxiliary	min	minimum
avg	average	mod	module
b	beam, bottom	mon	monitoring
B	Case B	MV	mixing valve
BP	Bypass	n	perpendicular, enumeration
br	brine	N, nom	nominal
$build$	building	net	net amount
Ca	carnot	o	outlet
C	collector, Case C	OV	overall system
c	coldside	ow	outer wall
ch	charge	p	constant pressure, absorber plate, pipe
cap	top and bottom cap of water storage	pcm	phase change material
$cond$	conduction	pen	penalty
$cons$	consumption	per	periphery
$conv$	convergence	$pers$	person
$corr$	corrected	$phys$	physical

<i>cut</i>	cut-out value	<i>pu</i>	pump
<i>cv</i>	control volume	<i>Q</i>	heat
<i>cw</i>	fresh water	<i>R</i>	removal, radiator
<i>d</i>	diffuse	<i>SAT</i>	Sodium Acetate Trihydrate
<i>dis</i>	discharge	<i>rel</i>	relative
<i>D</i>	design, Case D	<i>remain</i>	remaining
<i>dem</i>	demand	<i>ret</i>	return
<i>DHW</i>	domestic hot water	<i>rev</i>	reversible
<i>dp</i>	double port	<i>roof</i>	roof
<i>EB</i>	energy balance	<i>room</i>	room
<i>eff</i>	effective, effort	<i>S</i>	sun
<i>el</i>	electrical	<i>s</i>	solid
<i>ex</i>	exergy transition	<i>set</i>	set point
<i>exch</i>	exchanged	<i>SH</i>	space heating
<i>ext</i>	external	<i>SL</i>	solar loop
<i>f</i>	fluid, final	<i>sol</i>	from the sun
<i>fr</i>	friction	<i>spec</i>	specific
<i>frame</i>	window frame	<i>st</i>	storage, steel
<i>G</i>	solar irradiation	<i>su</i>	stratifying unit
<i>gain</i>	gain	<i>sup</i>	supply
<i>gr</i>	gross	<i>sur</i>	surrounding
<i>h</i>	of enthalpy flux, hot side	<i>sw</i>	side wall
<i>heat</i>	for heating purpose	<i>sys</i>	system
<i>high</i>	higher control value	<i>t</i>	technical, top
<i>HTC</i>	heat transfer coefficient	<i>T</i>	temperature dependent
<i>HTF</i>	heat transfer fluid	<i>tr</i>	transition
<i>hx</i>	heat exchanger	<i>u</i>	internal energy
<i>i</i>	inlet, inside, initial	<i>un</i>	unusable
<i>ins</i>	insulation	<i>up</i>	upper limit
<i>IR</i>	long wave radiation	<i>use</i>	usable, useful
<i>irr</i>	irreversible	<i>v</i>	constant volume
<i>it</i>	iterations	<i>W</i>	work
<i>iw</i>	inner wall	<i>w</i>	wall, water

1 INTRODUCTION

1.1 Motivation and definition of objectives

Solar thermal systems are potential suppliers for space heating and domestic hot water preparation in order to increase the fraction of renewable energy in this sector. As the time period of demand and availability of thermal energy provided by solar systems differs, thermal storage systems (TES) are required. In order to significantly increase the solar fraction in domestic and public space heating and hot water supply, seasonal storage systems have to be applied. The problem with conventional water based seasonal storage amongst others might be the necessary large storage volumes to cover a seasonal demand. Furthermore, heat losses over large storage periods can be a significant factor in system performances. Meeting the requirements and problems of seasonal thermal storage efficiently, new storage materials and systems have to be identified and developed. Within the EU funded international project COMTES (Combined development of Compact Thermal energy Storage Technologies) such storage systems are investigated. The project is divided into three development lines with the objective to design, test and integrate the following storage technologies (COMTES, 2011):

- Line A, *Solid sorption heat storage*: thermal energy storage by adsorption of water vapour in a solid sorption material (Zeolite)
- Line B, *Liquid sorption heat storage*: thermal storage by absorption of water in a liquid (Sodium Hydroxide, $NaOH$)
- Line C, *Subcooling phase change material heat storage (PCM)*: thermal storage in a subcooling phase change material (Sodium Acetate Trihydrate (SAT), $NaCH_3COO \cdot 3H_2O$)

The content of this work deals with the PCM- storage system of Line C exclusively. To achieve a solar fraction up to 95 %, seasonal storage is necessary. The main advantage of PCM, in this case Sodium Acetate Trihydrate with 46 % *wt.* water fraction, is a higher density than water (about 20 %) and the possibility to use the heat of fusion in addition to the sensible heat during storage processes. These characteristics of PCM promise more compact storage systems. In seasonal storage the characteristics of PCM are especially useful since water storage can reach up to 50 m³ depending on collector area and required solar fraction. Sodium Acetate Trihydrate provides another beneficial characteristic, the metastable state of a subcooled liquid. Subcooling means that the material is cooled down under the crystallisation temperature and remains in liquid phase without releasing the heat of fusion. By triggering nucleation, the remaining latent heat can be released and removed from the storage for heating purposes. If the subcooled liquid is stored at ambient temperature, theoretically no losses to the surrounding occur. By taking a closer look, this is not exactly the case. A certain amount of latent heat corresponding to the specific heat capacity and the temperature difference between the melting temperature and the temperature of the subcooled liquid cannot be utilized. Nevertheless, the process of subcooling can be a significant advantage during long storage periods by reducing the heat losses and is therefore an interesting aspect for seasonal heat storage. A main problem of PCM in general is a rather low thermal conductivity and phase change temperature level. This displays the major challenge for the development of PCM thermal storage.

The main task of this work is to estimate the efficiency and performance of a seasonal solar system using a subcooling PCM as thermal storage compared to a conventional water

based reference system. By means of transient system simulation, first and second law analysis should show improvement potential, possible integration and control strategies as well as advantages or weak spots of a PCM based system. Furthermore system design and optimization can be supported by these estimations. Common performance indicators should provide comparability between the conventional and the PCM based system.

1.2 State of the art

Research on PCM for thermal energy storage applications has a long history. For over more than 30 years a vast variety of phase change materials and their applications are investigated. For example, PCM can be used in the building sector for increasing the thermal mass of light weight constructions (Kendrick and Walliman, 2007). Furthermore utilization in the car industry for preheating and cooling of the engine oil supply (Örtel, 2004) can be found.

In the field of thermal heat storage (Lane, 1983) and (Lane, 1986) provides thermophysical properties as well as a selection of PCM applications. A theoretical analysis of thermal energy storage in a solar combi system using encapsulated PCM within a conventional water tank had been performed by (Heinz and Schranzhofer, 2010). The conclusion of their theoretical approach showed that an increase of the solar fraction up to 100 % for large storage periods is possible. Furthermore (Heinz, 2007) had been dealing with theoretical and experimental investigations on a boiler coupled with a small PCM storage. (Heinz, 2007) showed that the efficiency of the boiler could be increased and the production of carbon monoxides and hydrocarbons could have been reduced. (Mehling and Cabeza, 2008) give a broad description on theoretical and design aspects of PCM storage applications. Information on thermal storage and applications in general including PCM storages can be obtained from (Dincer and Rosen, 2011) as well. Another useful literature review on PCM material, heat transfer and applications is provided by (Zalba et al., 2003). Earlier work in the COMTES project by (Fan et al., 2010) has been dealing with CFD simulations of a box shaped PCM storage module like those which had been considered in this thesis. The results showed that high heat exchange rates have to be achieved for discharging processes.

In terms of energetic and exergetic analysis of PCM Storage, Sole et al. (Sole et al., 2008) provided theoretical and experimental work. Therefore they compared a water tank with a included PCM volume and a conventional water storage. The results showed an increase in energetic and exergetic efficiency due to the use of PCM. Furthermore the method of energy and exergy analysis of domestic heating systems had been applied (Blanco, 2012) and (Gunerhan and Hepbasli, 2007) to assess system performances.

For a direct utilization of PCM in seasonal thermal energy storage (TES) and solar heating systems the company "bbsolar GMBH" (bbsolar, 2014) offers a paraffin based thermal storage system. The PCM containment of bbsolar is of cylindrical shape. Subcooling effects are not harnessed. With "Rubitherm GMBH" another known vendor of phase change materials and applications for latent heat and cold storages in HVAC systems can be found (Rubitherm, 2014). In November 2013 the company "Heizkörper GMBH" (Heizkörper, 2013) had been introducing a ready for production thermal energy storage system for domestic heating purposes based on a cylindrical storage geometry containing subcooling Sodium Acetate Trihydrate (SAT). The heat exchanger is realised as a finned tube within the PCM filled cylinder. In reference to the last point, the direct utilization of PCM in storages, this thesis is dealing with box shaped storage modules for seasonal heat storage and might contribute useful knowledge for system integration and design in an upcoming market.

1.3 Procedural method

In order to evaluate the behaviour and the effect of the aforementioned qualities of a TES using PCM integrated in a domestic solar system, a theoretical approach had been chosen. First and second law analysis had been found as appropriate tools to assess not only the energetic performance but as well as the exergetic quality of the examined domestic heating systems. By the fact that a seasonal storage and a whole heating system has to be considered to give a proper estimation of the performance within realistic boundary conditions, the **TRaNsient SYstem Simulation Program** (TRNSYS 17.1) (SEL, 2012) had been selected to carry out the calculations. TRNSYS gives the possibility to model entire energy systems considering weather data and building structures as boundary conditions and perform transient calculations. The boundary conditions such as the building structure, tapping profiles and internal gains had been defined within the COMTES project but had not been part of this thesis. In the project, it had been agreed on a certain standard reference system basically according to TASK 32 (Heimrath and Haller, 2007), this had not been part of this thesis as well.

In the beginning of this work a short literature research on first and second law analysis of domestic heating systems and their components had been carried out. Furthermore it had been necessary to get familiar with the selected boundary conditions and reference system. Subsequently the reference system was set up in TRNSYS. The first and second law analysis had been included into the TRNSYS calculations by using the EQUATION statement. The EQUATION statement of TRNSYS gives the possibility to implement arithmetic equations which are calculated every time step. By setting up the reference system the basis for the different PCM system layouts had been set. For the PCM systems the reference system had been adapted by including the PCM storage model and altering the hydraulic layout and/or control strategies for the different variations. Possible system variations which are meeting the requirements however, had not been exactly clear in the beginning and were emerging during the implementation and testing processes.

The method how the modelling of the system simulations had been performed is loosely based on the so called "waterfall model". This iterative design process might be known from software engineering. It can be roughly divided into the following steps:

1. *Problem analysis*: In this step, requirements to the solar heating systems for example the requested solar fraction as well as boundary conditions according to previous agreements within the project, are collected and/or determined. Load cases for domestic hot water demand, internal gain profiles and the considered building type are chosen. Basic system concepts are selected. Test and evaluation of possible component models with different levels of detail for system simulations.
2. *Design*: Selection of system concepts in terms of hydraulic layouts and control strategies. First dimensioning and parametrization of system components, for example storage volume or collector area. Test, evaluation and selection of possible component models with different levels of detail for system simulations. Definition of assumptions and simplifications.
3. *Implementation*: This part consists of setting up the considered solar systems by implementing the component models into the TRNSYS simulation environment. Considering different levels of detail. Integration of energy and exergy analysis for every component, subsystem and the overall system into the TRNSYS environment. Determining output variables. Test runs and troubleshooting.

4. *Verification*: Checking the energy and exergy balances serve as control mechanisms to determine the quality of the chosen assumptions and simplifications.

After finishing the above described process, appropriate system models had been found. Subsequently a parameter variation for the PCM systems in order to determine performance maps depending on different key parameters, had been carried out. The reference solar system remains the same during this procedures because it is not the goal of this thesis to optimize it. Finally the performance of the various PCM systems had been compared to the defined reference system. For processing and displaying the obtained data the spreadsheet program EXCEL 2010 had been used. The calculation of performance indicator such as efficiencies and storage densities had been carried out in EXCEL 2010 as well.

2 BASICS

Energy and exergy analysis are common tools to determine the efficiency of systems and components in mechanical engineering. This section should give an overview which theoretical basics and simulation tools had been applied in this work. In sections 2.1 and 2.2 the general basics of energy and exergy are introduced briefly. Especially the exergy of solar radiation and the exergy of a phase change is discussed because they might not be as well-known as for example the exergy of heat. The utilization of those basics in terms of a solar thermal system using water and PCM as storage materials and its components is shown in section 2.3. Characteristic parameters and performance indicators of solar thermal systems obtained from literature are given in section 2.4. A short description of the applied simulation tools follows in sections 2.5.

2.1 Fundamental relations

2.1.1 Conservation of mass

A closed control volume, permeable for mass transport should be considered. The rate, the mass changes inside the volume is the difference of mass entering and leaving the system. This is also valid for more than two mass flows over the volume boundary. Entering mass flows are considered mathematical positive and leaving mass flows are considered negative. The well-known empirical law can therefore be written as follows (Baehr and Kabelac, 2009).

$$\frac{dm_{cv}}{d\tau} = \sum_i \dot{m}_i(\tau) - \sum_o \dot{m}_o(\tau) \quad (2.1)$$

For a steady state process, equation (2.1) simplifies to following expression.

$$\sum_i \dot{m}_i(\tau) = \sum_o \dot{m}_o(\tau) \quad (2.2)$$

2.1.2 First law of thermodynamics

Basically, the first law of thermodynamics or the conservation of energy states that one form of energy cannot be destroyed or produced but transformed into another form. Incropera gives following definition:

"At its heart, the first law of thermodynamics is simply a statement that the total energy of a system is conserved, and therefore the only way that the amount of energy in a system can change is if energy crosses its boundaries". (Incropera et al., 2011, page 13)

Energies which can cross the boundaries are any form of work (e.g. mechanical, electrical or magnetic), thermal energy (e.g. heat conduction) or energy associated with mass transport across the system boundaries. Hence the first law of thermodynamics for an open non steady system can be expressed by the following equation.

$$\delta Q + \delta W_t + \sum_j dm_j \cdot (h_j + e_{a,j}) = dU + dE_a \quad (2.3)$$

with the external energy $e_{a,j}$ of the considered mass element given by:

$$e_{a,j} = \frac{c_j^2}{2} + g \cdot z_j \quad (2.4)$$

Where W denotes technical work. Heat is described with Q . h_j defines the enthalpy of a flow stream. The internal energy is denoted with U and the external energy of the system itself (e.g. kinetic, potential) is defined by E_a . The first law also applies for energy rates (Baehr and Kabelac, 2009).

$$\dot{Q} + P + \sum_j \dot{m}_j \cdot (h_j + e_{a,j}) = \frac{dU}{d\tau} + \frac{dE_a}{d\tau} \quad (2.5)$$

In this work the first law will be written in both forms.

2.1.3 Second law of thermodynamics

The link between energy and exergy analysis is the second law of thermodynamics. There are several interpretations of this empirical law. By not going into too much detail, one of these interpretations is that all natural processes are irreversible or in other words, energy dissipates during every natural process due to friction (Baehr and Kabelac, 2009). It also restricts in which direction processes can proceed and how energy forms can be converted in one another. Especially the latter statement is essential for exergy considerations. In order to quantify the second law an extensive state variable is defined which is called entropy S . The entropy, sometimes referred to as disorder of a thermodynamic system is defined as (Baehr and Kabelac, 2009):

$$dS = \frac{\delta Q_{rev}}{T} \quad (2.6)$$

With the reversible heat:

$$\delta Q_{rev} = \delta Q_a + \delta Q_{fr} \quad (2.7)$$

Where the subscripts "a" and "fr" describe the heat transported over the systems boundaries and the heat generated within the system due to friction respectively. The temperature T denotes the temperature at which the heat leaves the system. The consequences of these definitions amongst others are that in a closed adiabatic system the entropy never decreases. In the special case of an ideal or reversible process the entropy change remains zero. Hence the second law of thermodynamics can be quantified with the known expression:

$$dS \geq 0 \quad (2.8)$$

To explain the statement of a closed adiabatic system a short example might be helpful. If a thermodynamical system is considered, for example a water filled volume like a heat storage, a system boundary can be drawn (see figure 2.1 black boundary). It is assumed that the volume is cooled down against ambient temperature and no other change of state occurs. This change of state can be displayed with a T/s diagram. In figure 2.2 it can be seen that the entropy of the system decreases because of the heat removal. The change of state can be considered isochoric since it is assumed that the density and volume is constant over the temperature change.

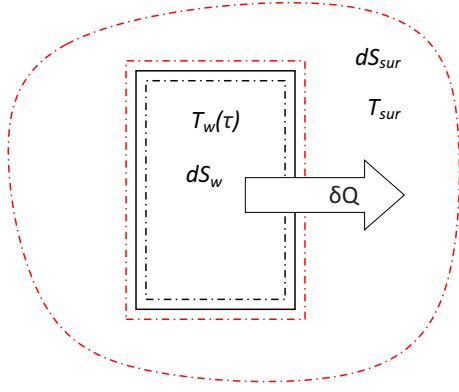


Figure 2.1: Simple thermodynamic system

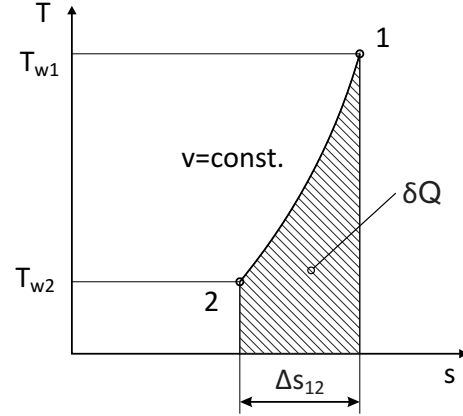


Figure 2.2: Change of state

The decrease of entropy in the system would imply a violation of equation (2.8) in the first place. But on the contrary the system cannot be denoted as adiabatic because of the heat removal. Therefore the system boundaries can be extended infinitely to include the surrounding until an adiabatic system is reached (figure 2.1 red boundary). Furthermore the surrounding serves as an infinite sink and does not change its state variables. By keeping in mind that entropy can only be transported by heat and with an associated mass element (Baehr and Kabelac, 2009) it is possible to form an entropy balance for the water volume and the surrounding.

For the water volume:

$$dS_Q = dS_w = dS_{sys} \quad (2.9)$$

Using equation (2.6) it can be written:

$$-\frac{\delta Q}{T_w} = dS_w = dS_{sys} \quad (2.10)$$

For the surrounding:

$$\frac{\delta Q}{T_{sur}} = dS_{sur} \quad (2.11)$$

And for the entire system the irreversible entropy generation can be obtained:

$$dS_{irr} = dS_{sys} + dS_{sur} = -\frac{\delta Q}{T_w} + \frac{\delta Q}{T_{sur}} = \delta Q \cdot \frac{T_w - T_{sur}}{T_w \cdot T_{sur}} \quad (2.12)$$

Since the temperature of water (T_w) has to be higher than the ambient temperature (T_{sur}) to drive the heat flux from the water tank to the surrounding until thermal equilibrium is reached, the integral of equation (2.12) is always positive and therefore follows the second law of thermodynamics. In the following section it is necessary to calculate exergies of a mass flow with a certain enthalpy and internal energies, hence the entropy change of those systems are needed. Using the entropy definition of equation (2.6) and the definitions for the reversible heat which can be retrieved from the first law of thermodynamics (Baehr and Kabelac, 2009), the entropy changes for a closed and an open system can be calculated.

With the definition of the reversible heat:

$$\delta Q_{rev} = dU + pdV = dH - Vdp \quad (2.13)$$

Furthermore it is assumed that the volume (V) and the pressure (p) is constant for liquids and the specific heat (c_v, c_p) is used for the internal energy and enthalpy changes, it can be written (Baehr and Kabelac, 2009):

$$\delta Q_{rev} = m \cdot c_v dT = m \cdot c_p dT = m \cdot c dT \quad (2.14)$$

Now the entropy change can be described under consideration of equation (2.6)

$$dS = m \cdot c \frac{dT}{T} \quad (2.15)$$

After integration of equation (2.15) between the states 0 and 1 and assuming that specific heat is not temperature dependent the following expression can be obtained:

$$S_1 - S_0 = m \cdot c \cdot \ln \left(\frac{T_1}{T_0} \right) \quad (2.16)$$

And of course for the specific entropy change:

$$s_1 - s_0 = c \cdot \ln \left(\frac{T_1}{T_0} \right) \quad (2.17)$$

Especially the last expression will be used in the following sections for exergetic assessment of enthalpy fluxes and internal energy.

2.2 Exergy

2.2.1 General aspects of exergy

The first law of thermodynamics as seen in section 2.1.2 shows that energy can only be converted into other energy forms. The second law gives restrictions to this conversion processes. Following the second law the complete conversion of every energy form into another arbitrary energy form is not possible (Baehr and Kabelac, 2009). A popular example is the conversion of heat into mechanical work with a heat engine. Even with a reversible process it is not possible to transform the heat completely into mechanical work. On the contrary, mechanical or electrical work can be fully converted into other energy forms. Therefore the completely convertible energy forms such as potential, kinetic, electrical and mechanical energy are called exergy.

$$\delta E_W = \delta W_j \quad (2.18)$$

Hence exergy is the part of an energy form which is fully convertible into every other energy form within a defined environment. In other words exergy is the maximum amount of work which can be retrieved reversibly from an energy form considering its environment (Baehr and Kabelac, 2009). The remaining part of the energy is called anergy and is absorbed by the considered environment. Anergy can also be seen as the entropy transporting part of the energy form. Since the first law is still valid energy can be defined as follows.

$$Energy = Exergy + Anergy$$

That means that every energy form is the sum of useable and unusable energy. Considering the mechanical work etc. the anergy part is zero.

2.2.2 The reference environment

In order to perform an exergy assessment of thermodynamic systems, a reference environment has to be defined. The environment in general represents a restriction to the amount of exergy which can be retrieved of an energy form. To define a reference environment, Dincer made the following statement:

"The exergy of a stream or system is zero when it is in equilibrium with the reference environment." (Dincer and Rosen, 2011, page 520)

Hence the exergy of the reference environment is considered zero. According to (Dincer and Rosen, 2011) the reference environment is working as an infinite sink with constant intensive state variables such as the thermodynamic temperature T_0 , pressure p_0 and the chemical potential $\mu_{0,i}$ of its i -th component. For the exergy analysis in this work the most important characteristic of the reference environment is its temperature T_0 (see section 3.2).

2.2.3 Exergy assessment of common energy forms

With equation (2.18) the exergy of work had already been defined. But what about the other forms of energy? Following the definitions from section 2.2.1 the exergy of heat can be quantified by considering an ideal heat engine where the heat is transformed into mechanical work. The reversible process can be displayed with the well-known Carnot cycle in a T/s diagram (see figure 2.3).

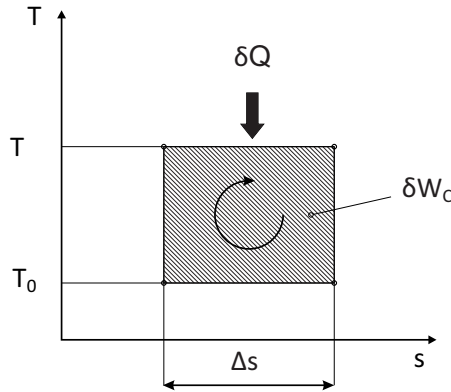


Figure 2.3: Carnot cycle of a heat engine (Baehr and Kabelac, 2009)

The heat in this process is applied isothermal at the temperature T and removed at the environment temperature T_0 to obtain the maximum amount of mechanical work. With the definition of entropy (equation (2.6)), an expression for the retrieved work can be found (Baehr and Kabelac, 2009).

$$dE_Q = \delta W_{Ca} = \delta Q \cdot \eta_{Ca} \quad (2.19)$$

With the Carnot factor given by:

$$\eta_{Ca} = \left(1 - \frac{T_0}{T}\right) \quad (2.20)$$

The maximum amount of work retrieved from the heat Q is per definition the exergy of heat. In order to assess the exergy of an enthalpy stream, an open steady state system

is considered. In this system the enthalpy stream is brought reversibly into equilibrium with the environment. Applying the first law with specific variables under consideration of equation (2.6) it can be written (Baehr and Kabelac, 2009):

$$e_h = w_{h,rev} = (h - h_0) - T_0 \cdot (s - s_0) \quad (2.21)$$

Using a constant specific heat for the enthalpy calculation and equation (2.17) for the entropy change the exergy of an incompressible fluid is defined as follows.

$$e_h = c_p \cdot \left[(T - T_0) - T_0 \cdot \ln \left(\frac{T}{T_0} \right) \right] \quad (2.22)$$

A similar expression can be found for the exergy of internal energy. Here a general closed system is considered and brought to equilibrium with the environment. Again the first law is applied. The reversible work retrieved has to be decreased by the work against the environment (Baehr and Kabelac, 2009).

$$e_u = w_{u,rev} = (u - u_0) - T_0 \cdot (s - s_0) + p_0 \cdot (v_0 - v) \quad (2.23)$$

Using a constant specific heat for calculating the internal energy and assuming a constant density and volume the exergy of the specific internal energy can be obtained.

$$e_u = c_v \cdot \left[(T - T_0) - T_0 \cdot \ln \left(\frac{T}{T_0} \right) \right] \quad (2.24)$$

2.2.4 Exergy of solar radiation

The exergy of radiation and solar radiation in particular, is a quite discussed topic. Several theoretical approaches can be found in literature, which are not always in agreement. In order to determine the exergy of solar radiation, a model has to be found how the radiation can perform reversible work. For example, (Zamfirescu and Dincer, 2009) used the classic model of a reversible heat engine where the hot side is in thermal equilibrium with the sun's surface and the cold side is in thermal equilibrium with the reference environment or the terrestrial surface, resulting in the already known expression for the Carnot factor. Furthermore in this approach the dilution of solar radiation due to scatter and absorption processes of the atmosphere had been accounted for. By leaving the dilution processes, one way to calculate the maximum work retrieved from solar radiation is shown by equation (2.25).

$$\dot{E}_G = A \cdot G_0 \cdot \left(1 - \frac{T_0}{T_S} \right) \quad (2.25)$$

Where A denotes the area of the a solar collector surface, G_0 denotes the irradiation, T_0 describes the reference temperature and T_S defines the sun's surface temperature. The Carnot expression had been used amongst others by (Farahat et al., 2009) for exergetic optimization of a flat plate collector. One of the most notable expressions had been originally developed by Petela (Petela, 2003) considering black body radiation. For modelling the conversion process, Petela considered a black body with the temperature T_S in a deformable enclosure where the expansion of a "photonic gas" performs the mechanical work (Zamfirescu and Dincer, 2009). The same expression had been derived by Candau (Candau, 2003) in a probably easier way to understand and therefore used for a short explanation. The theoretical

system used by Candau, as shown in figure 2.4, consists of an ideal collector (also a black body) with an infinitesimal lower temperature than the radiation source (in this case the sun with the temperature T), an ideal heat engine to perform the energy conversion and the reference environment serving as heat sink at the temperature T_0 .

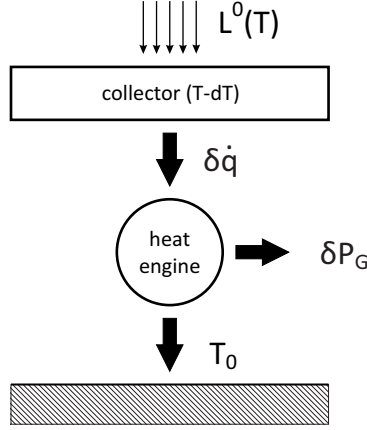


Figure 2.4: Conversion model for the exergy of solar radiation according to (Candau, 2003)

The luminance $L^0(T)$ emitted by the sun per unit area and time is received by the ideal collector with the temperature $(T - dT)$. The collector emits a luminance $L^0(T - dT)$ as well. Following Stefan-Boltzmann's law for black body radiation (the sun can be assumed a black body) the net heat flux received by the collector per unit area (\dot{q}) can be expressed with equation (2.26).

$$\delta \dot{q} = \frac{4 \cdot \sigma}{\pi} \cdot T^3 dT \quad (2.26)$$

Where σ denotes the Boltzmann constant. The collector at the same time, serves as the hot side of an ideal heat engine which converts the gained heat flux into mechanical work per unit time (P_G) or in other words into exergy. With the Carnot factor of the considered system an expression for the retrieved work per unit area and time can be found.

$$\delta P_G = \delta \dot{q} \cdot \left(1 - \frac{T_0}{T - dT}\right) dT \quad (2.27)$$

After integration of equation (2.27) between the T and T_0 an efficiency factor for solar radiation can be obtained.

$$\eta_G = \frac{P_G}{\left(\frac{\sigma \cdot T^4}{\pi}\right)} = 1 - \frac{4}{3} \cdot \left(\frac{T_0}{T}\right) + \frac{1}{3} \cdot \left(\frac{T_0}{T}\right)^4 \quad (2.28)$$

Finally, with the incident radiation G_0 , the area A and the temperature of the sun T_S the exergy of solar radiation can be expressed by the following equation (Candau, 2003).

$$\dot{E}_G = A \cdot G_0 \cdot \left[1 - \frac{4}{3} \cdot \left(\frac{T_0}{T_S}\right) + \frac{1}{3} \cdot \left(\frac{T_0}{T_S}\right)^4\right] \quad (2.29)$$

The difference between the simple Carnot approach from equation (2.25) and the radiation approach obtained from equation (2.29) to assess the exergy of radiation can be seen in figure

2.5 with a sun's temperature T_S of 5900 K and a reference temperature T_0 of 263 K. Figure 2.5 displays the exergy of the horizontal irradiation on a winter day, the red curve displays Petela's method and the blue curve shows the Carnot approach.

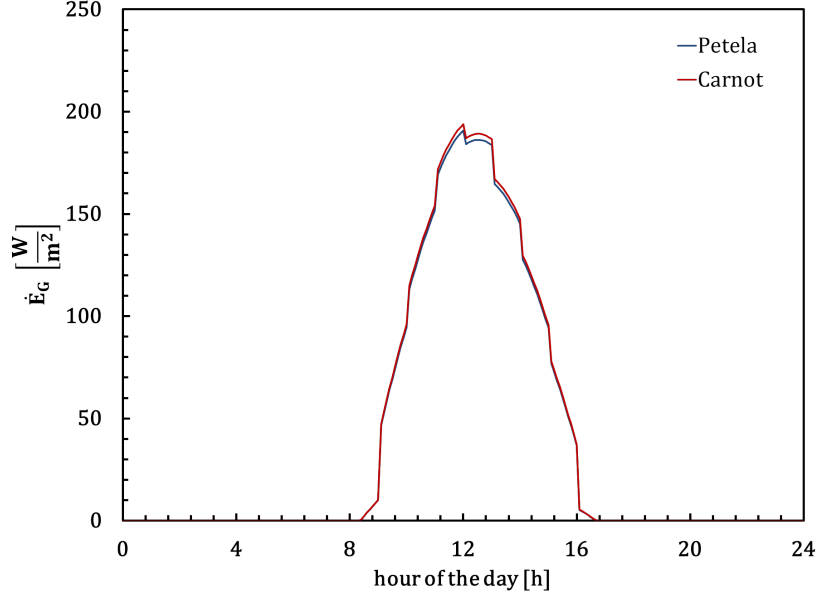
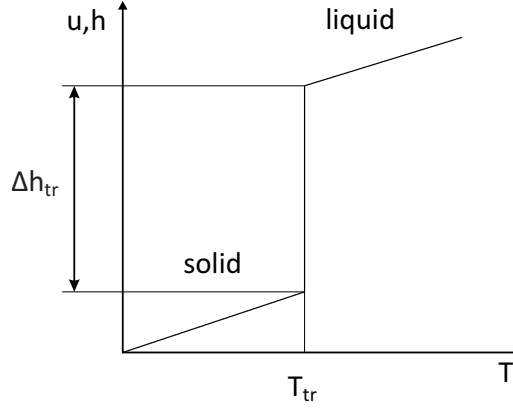


Figure 2.5: Comparison of exergy approaches for the total horizontal radiation during one day

In this work, Petela's approach had been used. The reason for this decision is that the derivation considers the radiative nature and basic thermodynamics. Another aspect is the small difference between the two methods where Petela's approach can be considered more pessimistic. Hence the exergy assessment of the solar system will not be overestimated. Equation (2.29) for example, had been used by (Gunerhan and Hepbasli, 2007) and (Blanco, 2012) in a solar system analysis context.

2.2.5 Exergy of a phase change

The starting point for modelling the exergy of a phase change can be the consideration of the internal energy. As shown in figure 2.6 the internal energy can be divided into three parts (the solid state, the phase transition and the liquid state).


 Figure 2.6: Ideal h/T -characteristic of a PCM

Therefore an expression for the change of the specific internal energy can be written as in equation (2.30) if a constant specific heat is assumed and the volume change between the solid and the liquid state is neglected (Ezan et al., 2010).

$$\Delta u_{pcm} = c_s \cdot (T_{tr} - T_{pcm,i}) + \Delta h_{tr} + c_l \cdot (T_{pcm,f} - T_{tr}) \quad (2.30)$$

Where the subscripts "s" and "l" denote "solid" and "liquid" respectively. Furthermore "i" and "f" denote the initial and final state of the PCM respectively. It is clear that if the material is only operated in the solid area the second and the third term of equation (2.30) disappear.

To receive the maximum amount of work a closed volume containing PCM with a transition temperature T_{tr} and a heat of fusion Δh_{tr} is brought to thermodynamic equilibrium with the environment. Since the heat of fusion can be considered as the amount of heat which can be removed at a temperature T_{tr} from the system, the equations (2.19) and (2.24) can be used to define the change of the specific exergy (Ezan et al., 2010).

$$\begin{aligned} \Delta e_{u,pcm} = & c_s \cdot \left[(T_{tr} - T_{pcm,i}) - T_0 \cdot \ln \left(\frac{T_{tr}}{T_{pcm,i}} \right) \right] + \Delta h_{tr} \cdot \left(1 - \frac{T_0}{T_{tr}} \right) \\ & + c_l \cdot \left[(T_{pcm,f} - T_{tr}) - T_0 \cdot \ln \left(\frac{T_{pcm,f}}{T_{tr}} \right) \right] \end{aligned} \quad (2.31)$$

2.2.6 Exergy balance and application

As stated before, exergy can be seen as a combination of the first- and second law of thermodynamics. Due to this, an exergy balance similar to the first law for every thermodynamic system can be formed. By considering the different exergies explained in the previous sections, a general formulation for an exergy balance can be found as follows (Baehr and Kabelac, 2009).

$$\delta E_Q + \delta E_W + \sum_i dm_i \cdot (e_{h,i} + e_{a,i}) = dE_U + dE_a + dI \quad (2.32)$$

Which of course is valid for exergy rates as well.

$$\dot{E}_Q + \dot{E}_W + \sum_i \dot{m}_i \cdot (e_{h,i} + e_{a,i}) = \frac{dE_U}{d\tau} + \frac{dE_a}{d\tau} + \dot{I} \quad (2.33)$$

In comparison to the energy balance in section 2.1.2 the additional term dI which can be referred to as irreversibility or exergy destruction can be observed. The irreversibility can be considered as a source term. According to the statements in section 2.2.1, dI is the exergy destruction or the energy absorbed by the environment because of the non-ideal energy conversion processes and the restrictions given by the second law in a general thermodynamic system. That means that the irreversibility of an thermal energy system or process, can be understand as a quantification to what extend this system or process strives to the ideal fully reversible system (Baehr and Kabelac, 2009; Dincer and Rosen, 2011). As a consequence of the second law the irreversibility can never decrease for a real system. Only in the case of an ideal system the irreversibility is zero.

$$\dot{I} \geq 0 \quad (2.34)$$

A direct connection between the irreversible entropy generation dS_{irr} and the irreversibility can be found by combining the entropy and energy balance for an open non steady system. Without derivation the well-known Gouy-Stodola relation is given by (Baehr and Kabelac, 2009):

$$\dot{I} = T_0 \cdot \dot{S}_{irr} \quad (2.35)$$

The reason why an exergy assessment is useful should have been pointed out in this section. It gives one the ability to compare and quantify real thermodynamic systems and processes to the ideal. Furthermore it is possible to compare different principles for the same application in terms of the more ideal process, like in the case of this work, two storage principles. System and layout optimization can be supported by identifying the components with the highest irreversibility and makes the exergy assessment to a useful tool in thermal energy system design.

2.3 Component models and exergetic analysis

A solar thermal system consists of various components, from thermal storages over collectors to heat exchangers, radiators and of course controller. In order to set up such systems in the TRNSYS simulation environment, mathematical models of these components, the so called "TRNSYS- types" are needed. Numerous types with different level of detail are available. A rough distinction can be made between "standard" and "non-standard types" which will be discussed in section 2.5 in more detail. This section however concentrates on the utilized active elements like heat exchangers and thermal storages, their mathematical models and the application of their exergetic assessment. This can be done by utilizing the in sections 2.1 and 2.2 acquired basic relations. Auxiliary components such as controller types are mentioned in section 4 but not described in detail.

2.3.1 Solar flat plate collector

In order to analyse a flat plate collector exergetic and performance wise, it is necessary to understand the basics of the used mathematical models. Since TRNSYS provides various types of one component, an appropriate model has to be chosen. Furthermore it is essential for exergetic considerations which are normally not included (or modelled) within the types, to understand the considered energy fluxes, simplifications and assumptions. The following derivations only cover the outlines, for detailed information it is referred to literature.

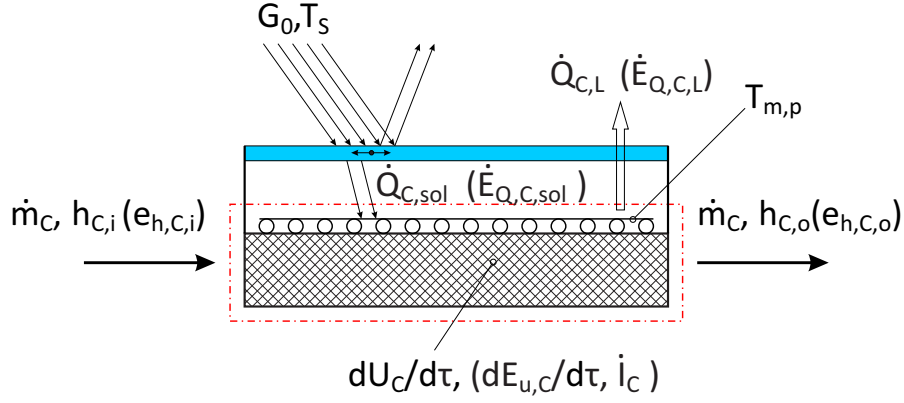


Figure 2.7: Energy and exergy fluxes of a flat plate collector

The starting point for a flat plate collector is a steady state energy balance according to figure 2.7. The internal energy and exergy (in brackets) are not accounted for at this point. Hence the energy balance can be written (Duffie and Beckman, 2006).

$$\dot{Q}_{C,u} = A_p \cdot \left[\underbrace{G_0 \cdot K \cdot \eta_0}_{\dot{q}_{C,sol}} - \underbrace{U'_L \cdot (T_{m,p} - T_{amb})}_{\dot{q}_{C,L}} \right] \quad (2.36)$$

Where $T_{m,p}$ denotes the mean absorber plate temperature and T_{amb} defines the ambient temperature. The optical efficiency (η_0) for incident radiation perpendicular (n) to the collector plane where τ describes the transmittance and α the absorptance of the collector glass cover, is given by equation (2.37)

$$\eta_0 = (\tau \cdot \alpha)_n \quad (2.37)$$

The incidence angle modifier K (AIM) describes the relation between the optical efficiency at normal incidence (test conditions) and an incidence angle θ and can be determined during standard collector tests. This factor accounts angle depending effects such as reflection and absorption dependencies (Duffie and Beckman, 2006).

$$K = \frac{(\tau \cdot \alpha)}{(\tau \cdot \alpha)_n}$$

The useful heat gain can also be obtained by equating the enthalpy fluxes.

$$\dot{Q}_{C,u} = \dot{m}_C \cdot (h_{C,o} - h_{C,i}) \quad (2.38)$$

And finally a collector efficiency according to figure 2.7 and equation (2.36) can be determined.

$$\eta_C = \frac{\dot{Q}_{C,u}}{A_p \cdot G_0} = 1 - \frac{\dot{Q}_{C,L}}{A_p \cdot G_0} \quad (2.39)$$

Where $\dot{Q}_{C,u}$ is the useful heat gain. A_p is the absorber plate area. G_0 denotes the incident solar radiation. U'_L can be considered as a combined heat transfer coefficient containing, conduction, convection and radiative losses to the environment and is derived in detail in (Duffie and Beckman, 2006). Determining the loss coefficient, the heat transfer from absorber to the fluid and time dependencies of all parameters is a very complex task. Therefore a

more practical model for the collector efficiency had been developed by Hottel and Whillier (Duffie and Beckman, 2006; SEL, 2012) and characterizes solar collectors by means of three parameters. These parameters can be obtained from standard collector tests and account for the aforementioned effects. In order to define those parameters, the next step is to combine equations (2.36) and (2.39) to yield a new expression for the collector efficiency (SEL, 2012).

$$\eta_C = F_R \cdot K \cdot \eta_0 - F_R \cdot U'_L \cdot \frac{(T_{m,p} - T_{amb})}{G_0} \quad (2.40)$$

The new factor F_R is introduced in equation (2.40) and is denoted as heat removal factor. It describes the ratio between the actual useful heat gain (see equation (2.38)) and the theoretical maximum possible heat gain if the absorber temperature is at collector inlet temperature ($T_{m,p} = T_{C,i}$) where the heat losses are at minimum (Duffie and Beckman, 2006). This factor contains effects like the non-ideal heat transfer between absorber and collector fluid (Stieglitz and Heinzl, 2012).

$$F_R = \frac{\dot{Q}_{C,u}}{A_p \cdot [G_0 \cdot K \cdot \eta_0 - U'_{C,L} \cdot (T_{C,i} - T_{amb})]} \quad (2.41)$$

Accounting the fact that the heat losses are temperature dependent, a linear dependency for U'_L is assumed (Duffie and Beckman, 2006; SEL, 2012).

$$U'_L = U_L + U_{L,T} \cdot (T_{m,p} - T_{amb}) \quad (2.42)$$

Combining equations (2.40) and (2.42) a second order characteristic for the collector efficiency can be found.

$$\eta_C = F_R \cdot K \cdot \eta_0 - F_R \cdot U_L \cdot \frac{(T_{m,p} - T_{amb})}{G_0} - F_R \cdot U_{L,T} \cdot \frac{(T_{m,p} - T_{amb})^2}{G_0} \quad (2.43)$$

Combining the factors the well-known efficiency model can be expressed as follows:

$$\eta_C = a_0 - a_1 \cdot \frac{(\Delta T_{amb})}{G_0} - a_2 \cdot \frac{(\Delta T_{amb})^2}{G_0} \quad (2.44)$$

Equation (2.44) sets the basis for the utilized collector types, for example the standard collector model "Type1b" (SEL, 2012) which had been used for the first simulation attempts. As mentioned in section 1.1 in seasonal applications high solar fractions are desired. Therefore required collector areas can reach up to 100 m². As a consequence of the transient system simulation, high collector areas and hence a higher thermal mass, a dynamic collector model had been selected. Therefore the non-standard type "type 832v5.00" developed by Bengt Perers et al. (Haller, 2012) had been used. This type follows equation (2.45).

$$\begin{aligned} \dot{q}_{C,u} = & (G_b \cdot K_b + G_d \cdot K_d) \cdot F_R \cdot (\tau \cdot \alpha)_n - c_{w,F_R} \cdot u_w \cdot (G_b + G_d) \\ & - c_{IR} \cdot (G_{IR} - \sigma \cdot T_{amb}^4) - a_1 \cdot \Delta T_{amb} - a_2 \cdot (\Delta T_{amb})^2 \\ & - c_{w,hl} \cdot u_w \cdot (\Delta T_{amb}) + \dot{q}_{lat} - c_{eff} \frac{dT_{m,p}}{d\tau} \end{aligned} \quad (2.45)$$

The core of this model is again provided by the efficiency characteristic of equation (2.44). Additionally, Type832v5.00 includes wind dependencies for incident radiation and heat losses, long wave radiation exchange with the surrounding, latent heat gains and the thermal mass of the collector. Simplifying the collector model for a further exergy analysis the latent

gain, wind dependencies and long wave radiation exchange had been neglected. Therefore the balance of the specific energy rates for the utilized collector type with respect to figure 2.7 is provided by equation (2.46). The simplification was carried out by just setting the respective parameters zero ($c_{w,FR}$, c_{IR} , $c_{w,hl}$, \dot{q}_{lat}).

$$\dot{q}_{C,u} = \underbrace{(G_b \cdot K_b + G_d \cdot K_d) \cdot F_R (\tau \cdot \alpha)}_{\dot{q}_{C,sol}} - \underbrace{a_1 \cdot \Delta T_{amb} - a_2 \cdot (\Delta T_{amb})^2}_{\dot{q}_{C,L}} - \underbrace{c_{eff} \frac{dT_{m,p}}{d\tau}}_{\frac{du_C}{d\tau}} \quad (2.46)$$

The indices "b" and "d" denote "beam" and "diffuse" with respect to the incident solar radiation. Now that the energy rate balance of the collector is found in equation (2.46) the exergy assessment can be carried out quickly. By just using the equations from section 2.2.3 for the different energy forms and considering that the heat loss, leaves the system (red system boundary in figure 2.7) at mean plate temperature $T_{m,p}$ and some minor rearrangements, an exergy rate balance for a flat plate collector can be defined with equation (2.47).

$$\dot{E}_{Q_{sol}} - \dot{m}_C \cdot [(h_{C,o} - h_{C,i}) - T_0 \cdot (s_{C,o} - s_{C,i})] - \dot{E}_{Q_{C,L}} - \frac{dE_{u,C}}{d\tau} = \dot{I}_C \quad (2.47)$$

The exergy of the internal energy can be computed if equation (2.24) is differentiated with respect to τ , c_v is replaced by the effective specific heat capacity of the collector c_{eff} and multiplied by the absorber area A_p . Furthermore it is assumed that the entire thermal mass has the mean absorber plate temperature $T_{m,p}$. Since transient simulations are performed, $T_{m,p}$ is a function of time and considering A_p , c_{eff} and T_0 as constant the following expression for the exergy of internal energy can be found.

$$\frac{dE_{u,C}}{d\tau} = A_p \cdot c_{eff} \cdot \frac{d}{d\tau} (T_{m,p} - T_0 \cdot \ln T_{m,p}) \quad (2.48)$$

In conclusion the exergy balance of the collector can be written as a function of temperature and time by applying the exergetic factor for solar radiation obtained from expression (2.28), the Carnot factor for the heat losses and equation (2.48) for the internal energy.

$$\begin{aligned} \dot{I}_C = & A_p \cdot \dot{q}_{C,sol} \cdot \left[1 - \frac{4}{3} \cdot \left(\frac{T_0}{T_S} \right) + \frac{1}{3} \cdot \left(\frac{T_0}{T_S} \right)^4 \right] - \dot{Q}_{c,L} \cdot \left(1 - \frac{T_0}{T_{mp}} \right) \\ & - \dot{m}_C \cdot c_f \cdot \left[(T_{C,o} - T_{C,i}) - T_0 \cdot \ln \left(\frac{T_{C,o}}{T_{C,i}} \right) \right] \\ & - A_p \cdot c_{eff} \cdot \frac{d}{d\tau} (T_{m,p} - T_0 \cdot \ln T_{m,p}) \end{aligned} \quad (2.49)$$

Similar expressions can be obtained from (Farahat et al., 2009). After the derivation in time is expressed in finite differences, equation (2.49) can be subsequently implemented in TRNSYS via the EQUATION statement.

2.3.2 Conventional thermal storage with auxiliary heater

In this work it is desired to compare a conventional water storage with a PCM based system. TRNSYS offers a couple of standard types with different level of detail. Due to the fact that the selected storage type has to have at least three double ports for the solar loop, the space heating and the hot water supply, a selection criterion was given. Another point

is the level of detail. For estimating seasonal storage applications, high storage volumes require an appropriate level of discretisation in order to display stratification effects sufficiently. Following this two premises the validated non-standard type "type 840" developed by Peter Puschnig and Hermann Schranzhofer (Heinz and Schranzhofer, 2007) at the Institute of Thermal Engineering (IWT) of the TU-Graz. This type was originally developed as a combined PCM-Water storage with enclosed PCM integrated in the water tank, but can also be utilized as a conventional water storage by setting the correspondent model parameters to zero. The outline of the mathematical approach of type 840 is described in the following part and obtained from (Heinz and Schranzhofer, 2007; Moser, 2012).

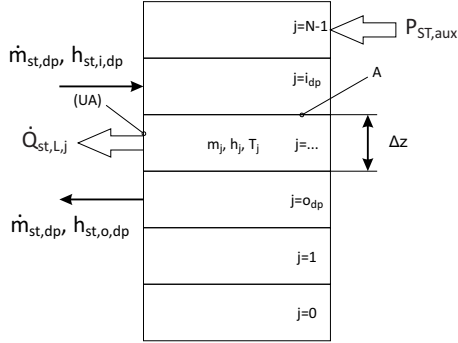


Figure 2.8: Mathematical approach of the Type840 model according to (Heinz and Schranzhofer, 2007)

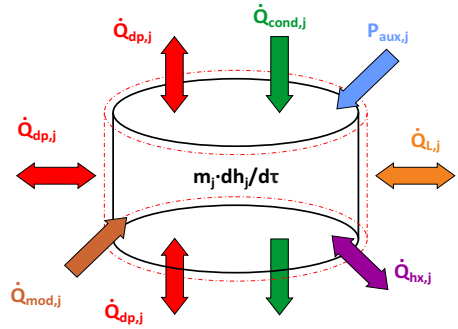


Figure 2.9: Energy balance of a considered storage node (Moser, 2012)

Figures and 2.8 and 2.9 show the one dimensional nodal approach of type 840. Therefore the storage is divided vertically into equally distributed sections. For each of this sections an energy balance can be defined according to figure 2.9 (Moser, 2012; Heinz and Schranzhofer, 2007).

$$m_j \cdot \frac{[h_j(\tau + \Delta\tau) - h_j(\tau)]}{\Delta\tau} = \dot{Q}_{dp}(\tau) + \dot{Q}_{aux}(\tau) + \dot{Q}_{cond}(\tau) + \dot{Q}_L(\tau) \quad (2.50)$$

Additional heat rates $\dot{Q}_{mod}(\tau)$ and $\dot{Q}_{hx}(\tau)$ had been deliberately neglected in equation (2.50). They account for the heat rate released by the aforementioned integrated PCM modules and the charge or discharge with internal heat exchangers respectively, which are not used in these investigations. Rearranging equation (2.50), the specific enthalpy of each node in the following time step can be calculated with an explicit method (Heinz and Schranzhofer, 2007). es and the charge or discharge with internal heat exchangers respectively, which are not used in these investigations. Rearranging equation (2.50), the specific enthalpy of each node in the following time step can be calculated with an explicit method (Heinz and Schranzhofer, 2007).

$$h_j(\tau + \Delta\tau) = h_j(\tau) + \frac{\Delta\tau}{m_j} \sum_k \dot{Q}_k(\tau) \quad (2.51)$$

To determine the temperature of each node a relation between the enthalpy and temperature is implemented according to the storage material characteristics. Once the enthalpy h_j is calculated with equation (2.51), the node temperature T_j can be obtained. In the following enumeration the different heat fluxes of expression (2.50) are explained briefly according to (Heinz and Schranzhofer, 2007) and in reference to figure 2.9:

a) *Power through double ports* (\dot{Q}_{dp}):

Double ports describe the hydraulic inlet and outlet connections of the storage. The applied heat rate to a storage node can then be computed by the following equation.

$$\dot{Q}_{dp,j} = \sum_{dp} \dot{m}_{dp,i} [(h_{dp,i} - h_j) \cdot \delta_{i_{dp},j} + (h_{j+d_{dp}} - h_j) \cdot \varepsilon_{i_{dp},j,o_{dp}}] \quad (2.52)$$

The in figure 2.9 displayed vertical red arrows should indicate the heat flux due to convection which is accounted for in equation (2.52) through the adjacent nodes until the outlet node is reached. The mathematical switch $\delta_{i_{dp},j}$ maintains the allocation of the inlet enthalpy flux to the right storage node and is defined as follows:

$$\delta_{i_{dp},j} = \begin{cases} 1 & \text{if } i_{dp} = j \\ 0 & \text{if } i_{dp} \neq j \end{cases}$$

With respect to the node temperatures, the direction of the heat fluxes from node to node are controlled by parameter d_{dp} .

$$d_{dp} = \begin{cases} +1 & \text{if } i_{dp} \geq o_{dp} \\ -1 & \text{if } i_{dp} \leq o_{dp} \end{cases}$$

It has also to be accounted for that only these nodes are considered, which are between the defined inlet and outlet nodes. This can be ensured with the switch $\varepsilon_{i_{dp},j,o_{dp}}$.

$$\varepsilon_{i_{dp},j,o_{dp}} = \begin{cases} 1 & \text{if } 0 < d_{dp} \cdot (i_{dp} - j) \leq d_{dp} \cdot (i_{dp} - o_{dp}) \\ 0 & \text{else} \end{cases}$$

In order to provide a better understanding of the used mathematical model displayed in figure 2.8 and the parameters described above, a short example should be given. A storage model with $N = 6$ nodes should be considered with an inlet height corresponding to the fifth node ($j = i_{dp} = 5$) and an outlet height corresponding to the second node ($j = o_{dp} = 2$) which describes, for example, a charging process. If now the heat flux of equation 2.52 has to be calculated the following mathematical switches and parameters are resulting in the values of table 2.1 according to the conditions given above.

Table 2.1: Resulting parameters for a Type840 example

j	d_{dp}	$d_{dp} \cdot (i_{dp} - j)$	$d_{dp} \cdot (i_{dp} - o_{dp})$	$\varepsilon_{i_{dp},j,o_{dp}}$	$\delta_{i_{dp},j}$
-	-	-	-	-	-
1	1	4	3	0	0
2	1	3	3	1	0
3	1	2	3	1	0
4	1	1	3	1	0
5	1	0	3	0	1
6	1	-1	3	0	0

Table 2.1 shows for example that only the nodes between the inlet and the outlet are considered for the charging heat flux (see column with $\varepsilon_{i_{dp},j,o_{dp}}$) and that the inlet charging enthalpy flux is allocated to node 5 as can be seen in the $\delta_{i_{dp},j}$ column. It also can be seen that the heat is transported from the upper nodes downwards which is indicated by a positive value of d_{dp} .

b) *Auxiliary heater* (\dot{Q}_{aux}):

The auxiliary power is provided by an electrical heater. The electrical power is directly converted into heat at the defined nodal position.

$$\dot{Q}_{aux,j} = P_{aux,j} \quad (2.53)$$

c) *Conduction between adjacent nodes* (\dot{Q}_{cond}):

To account for conduction effects in vertical direction because of the thermal conductivity of the storage medium, the containment walls, heat exchangers and other built-in components, an effective thermal conduction can be provided by the user in form of parameter λ_{eff} . The heat flux between adjacent nodes is computed with the following equation.

$$\dot{Q}_{cond,j} = \lambda_{eff} \cdot \frac{A}{\Delta z} \cdot (T_{j-1} - 2 \cdot T_j + T_{j+1})$$

d) *Heat losses* (\dot{Q}_L):

The heat losses of the thermal storage to its surrounding is calculated for each node (j) by the following simple expression.

$$\dot{Q}_{L,j} = (U \cdot A)_{st} \cdot (T_{amb} - T_j)$$

The heat transfer coefficient $(U \cdot A)_{st}$ can be again provided by the user and remain constant or temperature difference dependent. In this case the heat transfer coefficient had been left as a fixed value.

The basis for the exergy analysis is always the energy balance. By learning which energy fluxes are considered by the storage model their exergetic assessment can be executed.

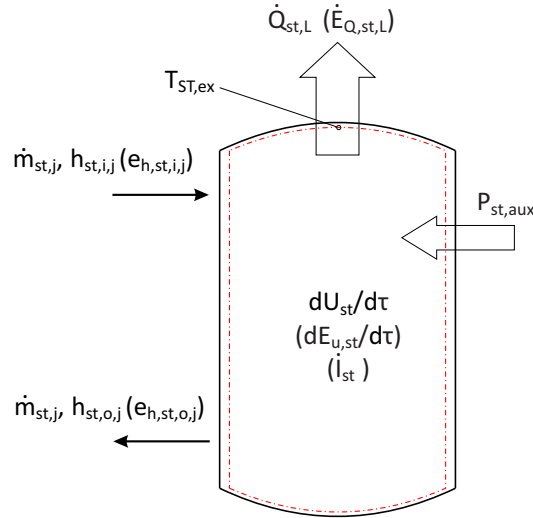


Figure 2.10: Global energy and exergy fluxes of a water storage

According to figure 2.10 and applying the fundamentals of section 2.2, the irreversibility of the thermal energy storage can be found as follows.

$$\dot{I}_{st} = P_{st,aux} + \sum_{dp} \dot{m}_{st,dp} \cdot (e_{h,st,i,dp} - e_{h,st,o,dp}) - \dot{Q}_{st,L} \cdot \left(1 - \frac{T_0}{T_{st,ex}}\right) - \frac{dE_{u,st}}{d\tau} \quad (2.54)$$

Replacing $e_{h,st}$ with equation (2.22) and expressing $\frac{dE_{u,st}}{d\tau}$ analogous to equation (2.48) the final exergy balance can be found.

$$\begin{aligned} \dot{I}_{st} = & P_{st,aux} + \sum_{dp} \dot{m}_{st,dp} \cdot c_f \cdot \left[(T_{st,i,dp} - T_{st,o,dp}) - T_0 \cdot \ln \left(\frac{T_{st,i,dp}}{T_{st,o,dp}} \right) \right] \\ & - \sum_j \dot{Q}_{st,L,j} \cdot \left(1 - \frac{T_0}{T_{st,j,ex}} \right) - \sum_j m_{st,j} \cdot c_f \cdot \frac{d}{d\tau} (T_j - T_0 \cdot \ln T_j) \end{aligned} \quad (2.55)$$

The fact that the number of nodes has to be defined rather high due to the large storage volumes makes the calculation of the internal energy with an average storage temperature impossible. To achieve a sufficient accuracy the calculation has to be performed for every single storage node j as stated in equation (2.55). Unfortunately, not every node temperature is accessible as an output from Type840. Hence this calculation had to be implemented into the TRNSYS type source code. The same problem occurs with the temperature $T_{st,ex}$ at which the heat losses leave the system reversibly. Since the losses are calculated for each node, the exergy of heat losses had to be calculated within the TRNSYS type as well. Therefore $T_{st,ex,j}$ had been defined as the temperature on the inner wall of the storage containment and calculated under consideration of a constant heat transfer coefficient α_{iw} with the following relation.

$$T_{st,ex,j} = T_j - \frac{\dot{Q}_{st,L,j}}{A_j \cdot \alpha_{i,w}} \quad (2.56)$$

The programming work had been done by Christoph Moser at the IWT.

2.3.3 PCM storage system

The storage concept within Line C of the COMTES project is a flat, box shaped PCM containment with heat exchangers arranged on the top and the bottom of the box. Prototype designs can also be found in (Fan et al., 2010) and (Furbo et al., 2012). In order to carry out TRNSYS simulations, a new non-standard type which accounts for the box shape design, had to be developed. The new PCM-storage model "Type8888" had been in parallel development with this thesis and implemented by Christoph Moser at the IWT. Figure 2.11 shows a scheme of the utilized node concept (left) and the energy fluxes which had been considered within the PCM storage model (right). Type8888 provides the possibility to define properties like the thickness of the PCM layer, the channel height of the heat exchanger, the number of storage modules as well as material characteristics of the containment and the PCM.

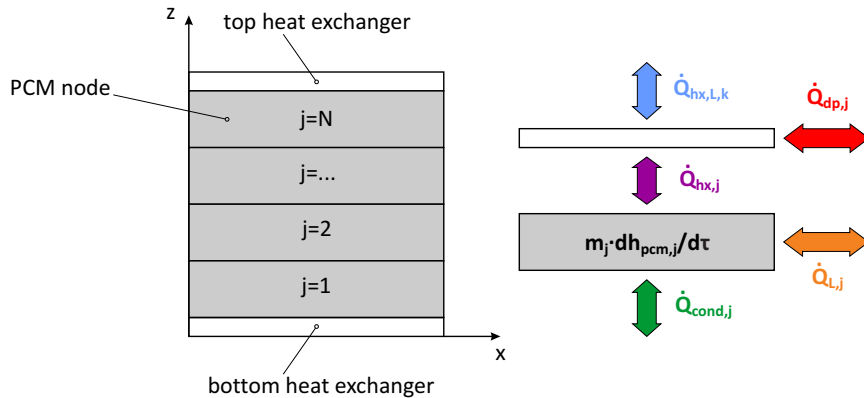


Figure 2.11: Mathematical approach of the T8888 model according to (Moser, 2014)

The following explanations are taken from (Moser, 2014) and should provide an insight into the function of the storage model. For a more detailed look it is referred to the mentioned literature. The mathematical model of the storage is, similar to Type840, based on an one dimensional nodal approach. According to figure 2.11 the enthalpy change of one PCM node can be written with the following equation.

$$m_j \cdot \frac{dh_{pcm,j}}{d\tau} = \dot{Q}_{cond,j}(\tau) + \dot{Q}_{L,j}(\tau) + \dot{Q}_{hx,j}(\tau) \quad (2.57)$$

Compared to the PCM nodes in vertical direction the heat exchangers are divided into nodes in flow direction. Figure 2.12 shows the detailed top heat exchanger channel divided into nodes and interacting with the PCM node.

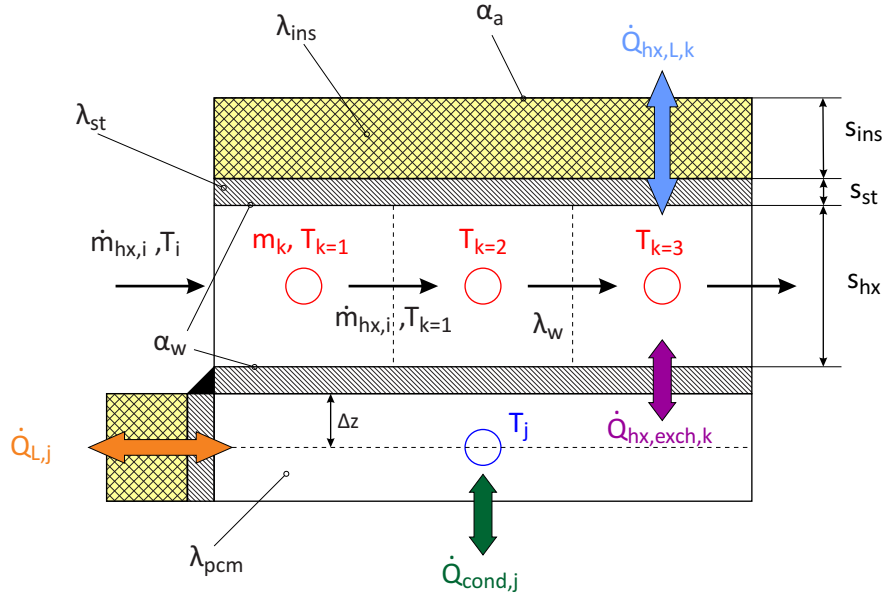


Figure 2.12: Interaction between heat exchanger nodes (k) and PCM node (j)

The colors of the heat fluxes in figure 2.12 are correspondent to those of figure 2.11. The energy balance of such a heat exchanger node can be expressed by equation (2.58).

$$m_k \cdot c_f \frac{dT_k}{d\tau} = \dot{Q}_{hx,dp}(\tau) + \dot{Q}_{hx,L,k}(\tau) + \dot{Q}_{hx,exch,k}(\tau) \quad (2.58)$$

For a better understanding, the heat rates in equation (2.57) and (2.58) are explained in the following enumeration.

a) *Heat removed or applied to the PCM node ($\dot{Q}_{hx,j}$):*

Since the heat exchanger and the PCM nodes are divided in different directions, only the sum of the heat rates removed or applied by the heat exchangers can be considered. Therefore the entire heat transferred to or from the PCM nodes can be computed with equation (2.59).

$$\dot{Q}_{hx,j} = \xi_1 \cdot \sum_k \dot{Q}_{hx,exch,k,b} + \xi_2 \cdot \sum_k \dot{Q}_{hx,exch,k,t} \quad (2.59)$$

The indices "b" and "t" are standing for "top" and "bottom" heat exchanger respectively. To ensure that the transferred heat is only applied to the top and bottom node of the

PCM material (see figure 2.11), the mathematical switches ξ_1 and ξ_2 are implemented and defined as follows.

$$\xi_1 = \begin{cases} 1 & \text{if } j = 1 \\ 0 & \text{else} \end{cases}$$

$$\xi_2 = \begin{cases} 1 & \text{if } j = N \\ 0 & \text{else} \end{cases}$$

- b) *Heat transferred by a heat exchanger node to the correspondent PCM node ($\dot{Q}_{hx,exch,k}$):*
 The heat rate transferred by one heat exchanger node (k) to the PCM node (j) can be described by equation (2.60). Where T_j denotes the temperature of the corresponding PCM node and T_k the mean temperature of one heat exchanger node.

$$\dot{Q}_{hx,exch,k} = (U \cdot A)_{hx,k} \cdot (T_j - T_k) \quad (2.60)$$

The heat exchanger is modelled as a rectangular channel (see figure 2.12) and the different layers between the considered temperatures have to be accounted for. Due to this, the heat transfer coefficient can be calculated with the well known equation for the heat transfer through a plane wall (see for example (Incropera et al., 2011)).

$$(U \cdot A)_{hx,k} = \frac{A_{hx,k}}{\frac{1}{\alpha_w} \cdot \xi_3 + \frac{s_{hx}}{\lambda_w} \cdot (1 - \xi_3) + \frac{s_{st}}{\lambda_{st}} + \frac{\Delta z}{\lambda_{pcm}}} \quad (2.61)$$

Where $A_{hx,k}$ denotes the effective heat exchanger area of one node. The channel height is described by s_{hx} and the wall thickness by s_{st} . Δz is a considered PCM layer thickness of the PCM node adjoining to the heat exchanger to account for conduction processes, which is the limiting factor as mentioned in section 1. The thermal conductivities λ_w and λ_{st} are accounting for the water layer and the steel containment respectively. The calculation of the convective heat transfer coefficient α_w is carried out by Nusselt correlations for internal flow which is not described in detail. If there is no mass flow $\dot{m}_{hx,i}$ through the heat exchanger only conduction through the water layer is assumed. This can be maintained by the parameter ξ_3 which is defined by the following condition.

$$\xi_3 = \begin{cases} 1 & \text{if } \dot{m}_{hx,i} > 0 \\ 0 & \text{else} \end{cases}$$

The overall heat transfer coefficient is then computed in each time step.

- c) *Heat conduction between the PCM nodes ($\dot{Q}_{cond,j}$):*
 The heat flux by conduction between the PCM nodes can be calculated with the well known Fourier approach (Incropera et al., 2011). Expressed in finite differences, the Fourier equation becomes the following form.

$$\dot{Q}_{cond,j} = \lambda_{pcm} \cdot \frac{A_j \cdot N}{H} \cdot (T_{j-1} - 2 \cdot T_j + T_{j+1}) \quad (2.62)$$

Where N denotes the number of defined storage nodes. H displays the overall thickness of the PCM layer. The area of the boundary surface between two nodes is expressed with A_j .

d) *Heat losses of PCM nodes* ($\dot{Q}_{L,j}$):

In Type8888, the heat losses of the PCM nodes which are not adjacent to the heat exchangers are computed with equation (2.63).

$$\dot{Q}_{L,j} = (U \cdot A)_{amb,j} \cdot (T_{amb} - T_j) \quad (2.63)$$

With the heat transfer coefficient according to expression (2.64).

$$(U \cdot A)_{amb,j} = \frac{A_j}{\frac{Z}{2 \cdot \lambda_{pcm}} + \frac{s_{st}}{\lambda_{st}} + \frac{s_{ins,j}}{\lambda_{ins}} + \frac{1}{\alpha_a}} \quad (2.64)$$

It might stand out that in the conduction term of the PCM nodes the layer thickness of $\frac{Z}{2}$ is assumed. Z denotes a weighted distance considering the width and length of the PCM, from the PCM nodes assumed in the center of one PCM layer to the steel containment. To account for the heat conduction through the PCM in a simple way, half of this distance is considered for the thermal resistance of the PCM layer.

e) *Heat rate through double ports* ($\dot{Q}_{hx,dp}$)

Calculating the power through the double ports can be realised similar to Type840. The idea behind equation (2.65) is displayed with figure 2.12. By setting up the the energy coupled to the flow stream entering and leaving the heat exchanger node, the retrieved heat rate can be calculated as follows.

$$\dot{Q}_{hx,dp} = \dot{m}_{hx,i} \cdot c_f \cdot [(T_i - T_k) \cdot \delta_{i,k} + (T_{i+dp} - T_k) \cdot \varepsilon_{i,k,o}] \quad (2.65)$$

In order to ensure the correct calculation, mathematical switches are necessary. The parameter $\delta_{i,k}$ defines the inlet node and succumbs the following condition.

$$\delta_{i,k} = \begin{cases} 1 & \text{if } i = k \\ 0 & \text{if } i \neq k \end{cases}$$

Since the heat exchangers are operated for charging and discharging the parameter dp considers the flow direction with the following condition.

$$dp = \begin{cases} +1 & \text{if } \dot{m}_{hx,i} > 0 \\ -1 & \text{if } \dot{m}_{hx,i} < 0 \end{cases}$$

Finally, the parameter $\varepsilon_{i,k,o}$ ensures that the second term in equation (2.65) disappears for the inlet node.

$$\varepsilon_{i,k,o} = \begin{cases} 1 & \text{if } 1 < dp \cdot (i - k) \leq dp \cdot (i - o) \\ 0 & \text{else} \end{cases}$$

f) *Heat loss of the heat exchanger* ($\dot{Q}_{hx,L,k}$):

The heat losses to the ambient can be obtained from the following expression.

$$\dot{Q}_{hx,L,k} = (U \cdot A)_{amb,k} \cdot (T_{amb} - T_k) \quad (2.66)$$

The heat transfer coefficient $(U \cdot A)_{amb,k}$ can then be found easily analogous to equation (2.64) with the parameters of figure 2.12 as follows.

$$(U \cdot A)_{amb,k} = \frac{A_{hx,k}}{\frac{1}{\alpha_w} + \frac{s_{st,k}}{\lambda_{st}} + \frac{s_{ins}}{\lambda_{ins}} + \frac{1}{\alpha_a}} \quad (2.67)$$

With $A_{hx,k}$ as outside surface area of the respective heat exchanger node.

g) *State of the PCM (enthalpy of the PCM)*: In order to calculate the temperatures of each PCM node the enthalpy approach had been selected. Similar to Type840, the temperature can be obtained by interpolating a given h/T characteristic. Recalling section 2.2.5 the h/T characteristic can be displayed by figure 2.13.

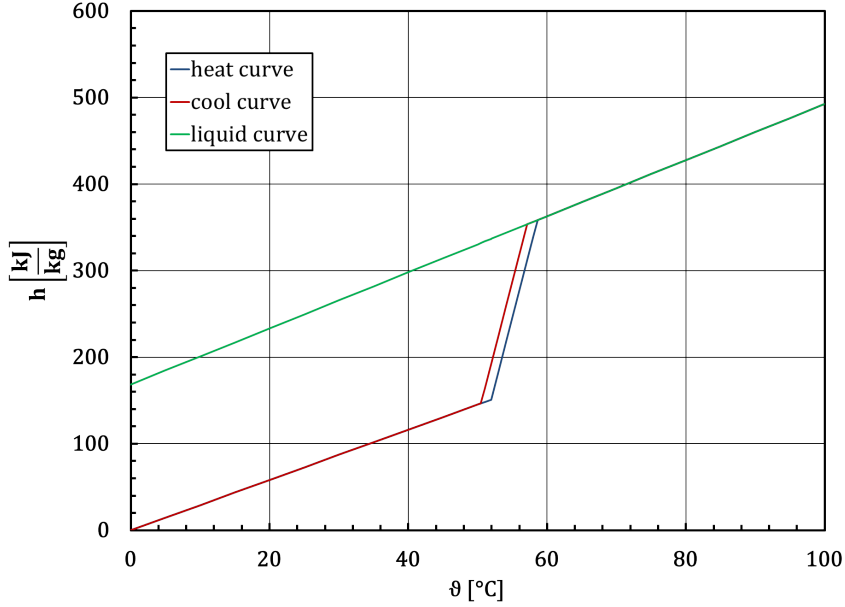


Figure 2.13: h/T characteristics of Type8888 (Moser, 2014)

An important aspect of figure 2.13 is that it includes the internal energy of the steel containment. That means that the single h/T characteristic of the phase change material itself, is weighted with the specific heat of the surrounding steel sheets according to their build-in mass.

One advantage of the enthalpy approach is, that it is possible to consider the subcooling effect (green line) and hysteresis effects which occur in the real process (blue and red line). Another point can be observed in figure 2.13. The phase change is not a sharp discontinuity compared to figure 2.6, it covers more a temperature range in real applications. Therefore a fictive specific heat of the PCM within the phase change area could be obtained from thermophysical measurements (compare to section 3.3) since the specific heat is represented by the slope of the enthalpy curve. The data behind figure 2.13 can be provided with a data file or can be generated within Type8888 itself by entering properties like the specific heat in liquid and solid state (c_l , c_s), the heat of fusion (Δh_{tr}), melting start and end temperatures ($T_{melt,start}$, $T_{melt,end}$) and the hysteresis. Details on the utilized PCM material and its properties are given in section 3.3.

In case of a heating process, the enthalpy of a PCM node follows the red curve if the node temperature of the heat exchanger is higher. If a cooling process occurs and the PCM node has a higher temperature than the heat exchanger node, the enthalpy follows the blue curve. By using these two different h/T characteristics the aforementioned hysteresis can be considered. The green curve considers the subcooling effect. In the mathematical model, subcooling occurs if a user defined temperature for secure melting over a certain

period of time is reached. Should a cooling process start after this condition is fulfilled, the enthalpy of the PCM node follows the green line.

Once the energy balance is completed and the governing terms are identified, the exergy analysis can be carried out. The first attempts of an exergy analysis had been performed outside the TRNSYS type by implementing the arithmetic equations into the EQUATION statement. It had become quite complex to implement the exergy analysis outside of Type8888, if high numbers of storage modules are needed. This is the case with seasonal applications, for example if 24 modules are needed, for each module the exergy balance according to figure 2.14 has to be performed which can become quite unhandy and complex.

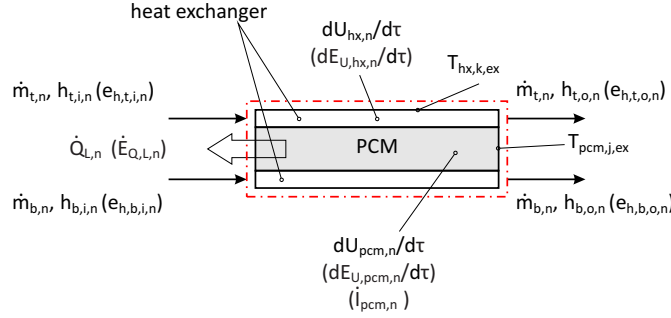


Figure 2.14: Energy and exergy fluxes of a PCM storage module

Another point is the transition temperature for heat losses and the resulting inaccuracies (compare to section 2.3.5) which led to the decision to implement the exergy assessment into Type8888. A general exergy balance for one heat storage module (n) can then be written according to figure 2.14 and the expressions from section 2.2.3 as follows.

$$\begin{aligned} \dot{I}_{pcm,n} = & \dot{m}_{t,n} \cdot (e_{h,t,i,n} - e_{h,t,o,n}) + \dot{m}_{b,n} \cdot (e_{h,b,i,n} - e_{h,b,o,n}) - \dot{E}_{Q,L,n} - \dot{E}_{Q,hx,L,n} \\ & - \frac{dE_{u,pcm,n}}{d\tau} - \left(\frac{dE_{u,hx,n}}{d\tau} \right)_t - \left(\frac{dE_{u,hx,n}}{d\tau} \right)_b \end{aligned} \quad (2.68)$$

With the exergy of the enthalpy fluxes for the top and the bottom heat exchanger respectively:

$$(e_{h,t,i,n} - e_{h,t,o,n}) = c_f \cdot \left[(T_{t,i,n} - T_{t,o,n}) - T_0 \cdot \ln \left(\frac{T_{t,i,n}}{T_{t,o,n}} \right) \right] \quad (2.69)$$

The exergy of the heat losses per PCM node ($\dot{E}_{Q,L,j}$) can be easily expressed for each module with equation (2.70).

$$\dot{E}_{Q,L,n} = \sum_j \dot{Q}_{L,j} \cdot \left(1 - \frac{T_0}{T_{pcm,j,ex}} \right) \quad (2.70)$$

The exergy of the heat exchanger losses can be formulated similarly.

$$\dot{E}_{Q,hx,L,n} = \sum_k \dot{Q}_{hx,L,k} \cdot \left(1 - \frac{T_0}{T_{hx,k,ex}} \right) \quad (2.71)$$

The transition temperatures are always considered as the inner wall temperatures of the heat exchanger or the PCM containment. Therefore the transition temperature for the

PCM node ($T_{pcm,j,ex}$) can be obtained from equation (2.72) by rearranging expression (2.63) and considering only the effective thermal resistance (λ_{pcm}).

$$T_{pcm,j,ex} = T_j + \frac{\dot{Q}_{L,j}}{\frac{A_j \cdot 2 \cdot \lambda_{pcm}}{Z}} \quad (2.72)$$

And for the heat exchanger, the transition temperature $T_{hx,k,ex}$ can be found with the same procedure applied for equation (2.66) and written as follows.

$$T_{hx,k,ex} = T_j + \frac{\dot{Q}_{hx,L,k}}{A_k \cdot \alpha_w} \quad (2.73)$$

The exergy of the internal energy of the PCM is computed with a similar approach to the h/T characteristic mentioned before. Applying equation (2.31) from section 2.2.5 to the h/T characteristic of the PCM, an exergy/temperature characteristic can be calculated according to figure 2.15 with a reference temperature $T_0 = 263.15$ K. These characteristics are implemented into the TRNSYS type.

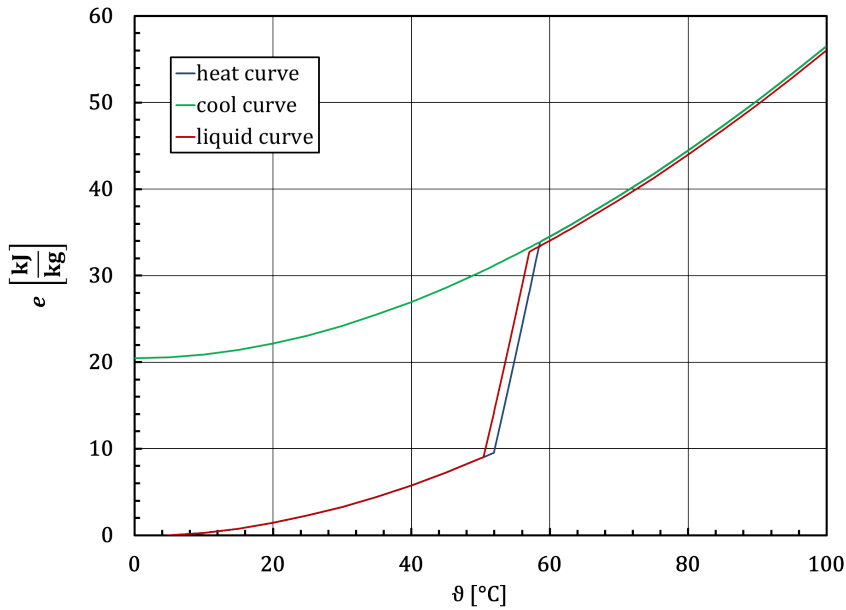


Figure 2.15: Exergy/T characteristics of Type8888 (Moser, 2014)

Once the PCM node temperature is known the exergy of the PCM can be interpolated from the obtained exergy/temperature curve. The meaning of the curves are identical to those which are stated above according to the h/T characteristics. The last remaining term is the exergy of internal energy of the heat exchanger $\dot{E}_{u,hx,n}$ in respect to the top and the bottom one. Analog to the other described components, the exergy of the internal energy can be formulated again with equation (2.74).

$$\dot{E}_{u,hx,n} = \sum_k m_k \cdot c_f \cdot \frac{d}{dT} (T_k - T_0 \cdot \ln T_k) \quad (2.74)$$

Finally, equation (2.68) is completely defined and the entire irreversibility of the PCM storage system can be calculated as the sum of the module irreversibilities.

If the storage module number is high, the handling of the type outputs might get complicated in order to create control strategies. Therefore Type8888 comes with an additional controller type "Type8889" also developed by Christoph Moser. For instance, every module has a state (liquid, solid, subcooled) and let's say one mean temperature or a specific energy content. Now, if a larger number of modules are needed the sum of outputs are becoming quite high. In order to build a control sequence which has to select a module to charge or discharge, the outputs of every module have to be worked in which can be rather complex and unhandy. Therefore Type8889 provides predefined charging and discharging cases for selecting an appropriate module. However the possibility of an individual control concept is still given. For more details on Type8889 it is again referred to (Moser, 2014).

2.3.4 Counter flow heat exchanger

The seasonal application of TES requires certain measures in order to maintain the function of the solar loop and decreasing or avoiding downtime during winter. Temperatures under the solidification point of the heat transfer fluid (HTF) can cause such downtimes and may lead to damages of system components. A method to avoid a freezing HTF can be provided by a so called "drain back system". With a drain back system the HTF is drained from the solar loop and especially from the collectors into a storage volume and air is filling the remaining space, if the solidification temperature is fallen below. This allows to use water as a HTF and a direct connection of the solar loop with the thermal energy storage (Stieglitz and Heinzl, 2012). On the other hand, drain back systems are quite complex in terms of system layout and control strategies. An easier approach is to use special HTFs like antifreeze mixtures of water and alcohol, accepting problems like a lower heat capacity than water and the need of a heat exchanger which connects the solar loop and the TES. The latter method was agreed on in this work (Bertsch et al., 2013). Furthermore a heat exchanger is used in the domestic hot water (DHW) loop (see section 4). Hence a counter flow heat exchanger model is described in this section.

For the TRNSYS simulations the standard type "Type5b" for the collector loop and the non-standard type "Type805" for the DHW loop are utilized. Both of them follow the same mathematical model with one exception. Type805 calculates the hot side mass flow iteratively in order to achieve a user defined set point temperature at the cold side outlet. At Type5b the hot side massflow is just an input value. The mathematical model is known as the "Effectiveness-NTU-method" or referred to as "minimum capacitance approach". The following description should give an overview of the model and is basically taken from (SEL, 2012) and (Incropera et al., 2011). For a more detailed derivation it is referred to (Incropera et al., 2011) and (Duffie and Beckman, 2006). Figure 2.16 shows the scheme of a counterflow heat exchanger, energy and exergy fluxes used for the following explanations.

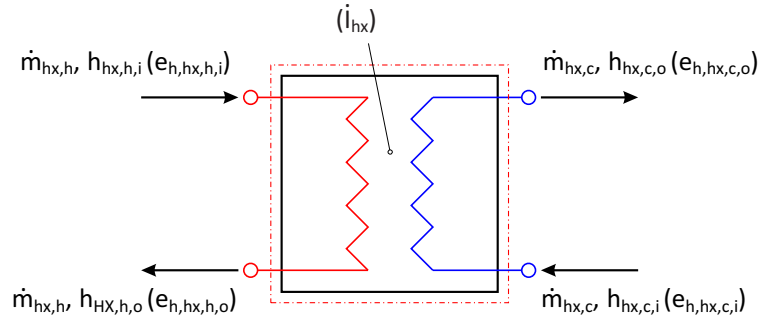


Figure 2.16: Energy and exergy fluxes of counterflow heat exchanger

To illustrate the behaviour of a counter flow heat exchanger the temperature characteristic displayed over the heat exchanger length can be useful. Correspondent to the heat capacity rates of the hot side (\dot{C}_h) and the cold side HTF (\dot{C}_c) and the heat transfer coefficient ($(U \cdot A)_{hx}$) can result in a temperature characteristic shown in figure 2.17.

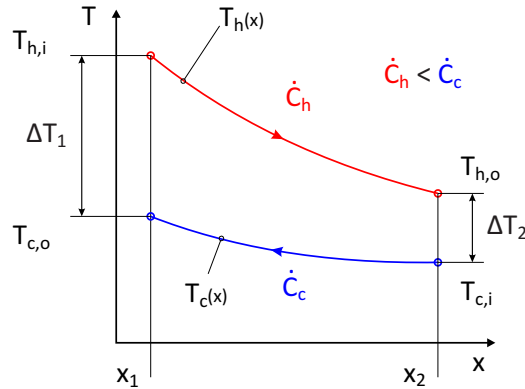


Figure 2.17: Schematic T/x characteristics of a counter flow heat exchanger according to (Incropera et al., 2011)

The slope of the temperature curves is representing the heat capacity rates of the respective flow stream. The positions x_1 and x_2 should indicate the inlet and the outlet of the heat exchanger. If now an ideal heat exchanger without environmental losses and an infinite length ($x = \infty$) is considered, figure 2.17 changes to figure 2.18.

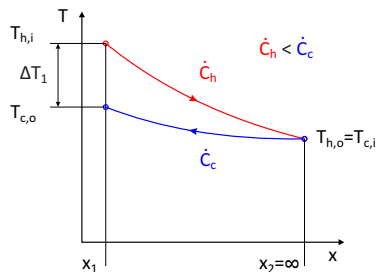


Figure 2.18: Schematic T/x characteristics of an ideal heat exchanger and $\dot{C}_h < \dot{C}_c$

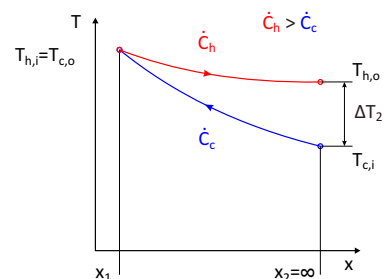


Figure 2.19: Schematic T/x characteristics of an ideal heat exchanger and $\dot{C}_h > \dot{C}_c$

It can be seen that the temperature of the cold side outlet can reach the hot side inlet temperature ($T_{c,o} = T_{h,i}$) if \dot{C}_c is smaller than \dot{C}_h as displayed in figure 2.19. If \dot{C}_c is greater

than \dot{C}_h the hot side outlet temperature can be cooled down to the cold side inlet temperature ($T_{h,o} = T_{c,i}$) as can be seen in figure 2.18 (Incropera et al., 2011). Setting up the energy balance for each flow stream, a maximum heat transfer rate of the heat exchanger can be determined for those two cases with the following equation.

$$\dot{q}_{max} = \begin{cases} \dot{C}_c \cdot (T_{h,i} - T_{c,i}) & \text{if } \dot{C}_c < \dot{C}_h \\ \dot{C}_h \cdot (T_{h,i} - T_{c,i}) & \text{if } \dot{C}_c > \dot{C}_h \end{cases} \quad (2.75)$$

Equation (2.75) shows the interesting aspect that the maximum heat transfer rate is always achieved with the lower heat capacity rate (Incropera et al., 2011). Therefore equation (2.75) can be simplified to the following expression.

$$\dot{q}_{max} = \dot{C}_{min} \cdot (T_{h,i} - T_{c,i}) \quad (2.76)$$

Now, that the maximum heat transfer rate can be calculated, a heat exchanger effectiveness (ε) can be defined.

$$\varepsilon = \frac{\dot{q}}{\dot{q}_{max}} \quad (2.77)$$

Where \dot{q} denotes the actual heat transfer rate of the non ideal heat exchanger. The main advantage resulting from the definition of an effectiveness is that it becomes possible to determine the actual heat rate with a simple relation just depending on the inlet temperatures the minimum heat capacity rate. Hence the actual heat rate can be computed as follows.

$$\dot{q} = \varepsilon \cdot \dot{C}_{min} \cdot (T_{h,i} - T_{c,i}) \quad (2.78)$$

The next step is to express the effectiveness with known parameters. It can be shown that ε is a function of a parameter named NTU (Number of Transfer Units) and the relation between \dot{C}_{min} and \dot{C}_{max} (Incropera et al., 2011).

$$\varepsilon = f \left(NTU, \frac{\dot{C}_{min}}{\dot{C}_{max}} \right)$$

With the well known dimensionless parameter NTU defined as follows.

$$NTU = \frac{(U \cdot A)_{hx}}{\dot{C}_{min}} \quad (2.79)$$

And finally, without derivation, the effectiveness for a counter flow heat exchanger can be calculated with equation (2.80) (SEL, 2012).

$$\varepsilon = \frac{1 - e \left[-NTU \cdot \left(1 - \frac{\dot{C}_{min}}{\dot{C}_{max}} \right) \right]}{1 - \left(\frac{\dot{C}_{min}}{\dot{C}_{max}} \right) \cdot e \left[-NTU \cdot \left(1 - \frac{\dot{C}_{min}}{\dot{C}_{max}} \right) \right]} \quad (2.80)$$

With the known inlet temperatures, the heat capacity rates and the heat transfer coefficient, the outlet temperatures and the heat transfer rate can be computed by considering equations (2.78) and (2.80) as well as the energy balance for each flow stream according to figure 2.16.

The irreversibility can also be found very quickly. According to figure 2.16 and considering the basic equations from section 2.2.3 and keeping in mind that no thermal mass of the heat exchanger and no ambient losses are accounted for by the mathematical model, the exergy balance can be written with the following expression.

$$\begin{aligned} \dot{I}_{HX} = & \dot{m}_h \cdot c_{f,h} \cdot \left[(T_{h,i} - T_{h,o}) - T_0 \cdot \ln \left(\frac{T_{h,i}}{T_{h,o}} \right) \right] \\ & + \dot{m}_c \cdot c_{f,c} \cdot \left[(T_{c,i} - T_{c,o}) - T_0 \cdot \ln \left(\frac{T_{c,i}}{T_{c,o}} \right) \right] \end{aligned} \quad (2.81)$$

The mass flows \dot{m}_h and \dot{m}_c as well as the inlet and outlet temperatures can be obtained as outputs from the TRNSYS types, Type5b and Type805 respectively. Equation (2.81) can be again subsequently entered into TRNSYS via the EQUATION statement and calculated in every timestep.

2.3.5 Radiator

The energy required for space heating is provided by a radiator. In the course of the project it would have been possible to select a floor heating system as well. In this thesis the intention was to analyse a storage system which can be installed in already existing structures in terms of refurbishments where not always a floor heating system is available.

A dynamic radiator is modelled with the non-standard type "Type362" developed by S. Holst of the "Bayrisches Zentrum für angewandte Energieforschung e.V." (ZAE). The following explanations are taken from (Holst, 1996) and partially from (Recknagel et al., 2007). Figure 2.20 shows the schematic structure, the energy and exergy fluxes (in brackets) according to the mathematical model.

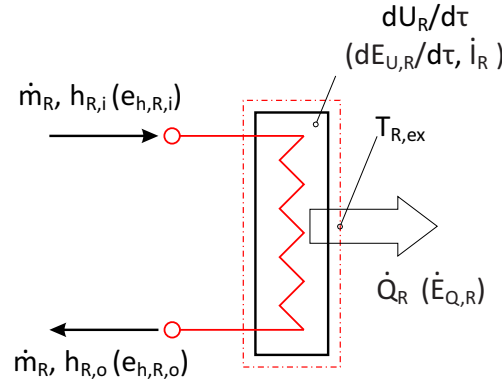


Figure 2.20: Energy and exergy fluxes of a radiator

The energy balance for a dynamic radiator model considers the thermal mass (C_R) of the radiator. In the case of Type362 the thermal mass is concentrated into one node with the return temperature $T_{R,o}$ of the radiator. This model is called "first order radiator model". The energy balance can then be written with the following first order differential equation.

$$\dot{m}_R \cdot c_f \cdot (T_{R,i} - T_{R,o}) - \underbrace{\dot{Q}_R \cdot \left(\frac{\Delta T_{lg}}{\Delta T_{lg,N}} \right)^n}_{\dot{Q}_R} = C_R \cdot \underbrace{\frac{dT_{R,o}}{d\tau}}_{\frac{dU_R}{d\tau}} \quad (2.82)$$

Inlet and outlet temperatures are denoted with $T_{R,i}$ and $T_{R,o}$ respectively. The lumped thermal capacitance of the HTF and the metal body are described with C_R . The term \dot{Q}_R may stand out and should be looked at a little bit closer. The heat transfer rates $\dot{Q}_{R,j}$ of a radiator at two operation points ($\Delta T_{lg,1}$ and $\Delta T_{lg,2}$) can be set into relation (Recknagel et al., 2007).

$$\frac{\dot{Q}_{R,1}}{\dot{Q}_{R,2}} = \frac{U_1 \cdot \Delta T_{lg,1}}{U_2 \cdot \Delta T_{lg,2}} \quad (2.83)$$

With the supply and return temperature and the temperature of the surrounding $T_{sur,j}$, the logarithmic temperature difference ($\Delta T_{lg,j}$) can be defined as follows.

$$\Delta T_{lg,j} = \frac{T_{R,i,j} - T_{R,o,j}}{\ln \left(\frac{T_{R,i,j} - T_{sur,j}}{T_{R,o,j} - T_{sur,j}} \right)} \quad (2.84)$$

The heating surface area of the radiator can be canceled in equation (2.83) but the temperature dependence of the heat transfer coefficient (U_j) has to be considered. The heat transfer rate can then be approximated with equation (2.85) by considering the convective heat transfer as the limiting factor (Holst, 1996).

$$\dot{Q}_{R,j} = K_R \cdot (\Delta T_{lg,j})^n \quad (2.85)$$

With a radiator model dependent constant K_R which can be approximated as temperature independent and the so called radiator exponent (n) which is as well a model characteristic. In this case, for a standard radiator, n can be assumed with 1.3 (Recknagel et al., 2007). Now let's say the operation point two is a nominal point ($j = N$) with constant temperatures for example in low temperature systems $\vartheta_{R,i} = 40^\circ\text{C}/\vartheta_{R,o} = 35^\circ\text{C}/\vartheta_{sur} = 20^\circ\text{C}$. Hence a nominal heat rate \dot{Q}_N can be computed. The nominal heat rates are obtained from radiator tests and provided by data sheets. With a given \dot{Q}_N and the test conditions the actual heat rate \dot{Q}_R can be calculated under combination of equation (2.83) and (2.85).

$$\dot{Q}_R = \dot{Q}_N \cdot \left(\frac{\Delta T_{lg}}{\Delta T_{lg,N}} \right)^n \quad (2.86)$$

Furthermore \dot{Q}_R can be expressed with equation (2.87) since it is assumed that the thermal mass is at the temperature $T_{R,o}$.

$$\dot{Q}_R = (U \cdot A)_R \cdot (T_{R,o} - T_{R,i}) \quad (2.87)$$

Combining equation (2.86) and (2.87), the effective heat transfer coefficient ($(U \cdot A)_R$) can be calculated.

$$(U \cdot A)_R = \frac{\dot{Q}_N \cdot \left(\frac{\Delta T_{lg}}{\Delta T_{lg,N}} \right)^n}{(T_{R,o} - T_{R,i})} \quad (2.88)$$

Hence the differential equation (2.82) can be written as follows.

$$\dot{m}_R \cdot c_f \cdot (T_{R,i} - T_{R,o}) - (U \cdot A)_R \cdot (T_{R,o} - T_{R,i}) = C_R \cdot \frac{dT_{R,o}}{d\tau} \quad (2.89)$$

Equation (2.89) is then solved analytically with the TRNSYS subroutine DIFFEQ. Additionally, Type362 is able to consider the supply and return pipes as thermal masses and loss

factors. The pipe models of Type362 had been intentionally left out at this point because they had not been used during the simulations. In the system simulation, stand alone pipe models (Type709) had been utilized and are described in section 2.3.6.

At this point, it is again the task to find the appropriate exergy balance of the radiator model. According to figure 2.20 and the equations from section 2.2.3 a exergy balance can be formulated as follows.

$$\begin{aligned} \dot{I}_R = & \dot{m}_R \cdot c_{f,R} \cdot \left[(T_{R,i} - T_{R,o}) - T_0 \cdot \ln \left(\frac{T_{R,i}}{T_{R,o}} \right) \right] \\ & - \dot{Q}_R \cdot \left(1 - \frac{T_0}{T_{R,ex}} \right) - \frac{dE_{u,R}}{d\tau} \end{aligned} \quad (2.90)$$

Analog to equation (2.48) from section 2.3.1 the exergy of the internal energy can be written as follows.

$$\frac{dE_{u,R}}{d\tau} = C_R \cdot \frac{d}{d\tau} (T_{R,o} - T_0 \cdot \ln T_{R,o}) \quad (2.91)$$

Implementing equation (2.91) into the EQUATION statement of TRNSYS caused some numerical problems. In comparison to a smooth internal energy characteristic of the radiator, the exergy of the internal energy showed quite massive peaks if stronger changes of the internal energy occurred. The causing effect might have been that the internal energy is calculated within Type362 with the arithmetic mean of $T_{R,o}$ at the beginning and at the end of the time step. Since that the mean temperature is not accessible as a type output, the calculation of equation (2.91) had to be implemented into the TRNSYS source code as well which was again performed by Christoph Moser. Now, the exergy of the internal energy of the radiator can obtained as an output of Type362. Another difficulty is provided by the determination of the transition temperature ($T_{R,ex}$) of the heat transfer rate \dot{Q}_R . It becomes difficult to determine an exact transition temperature since the radiator is treated like a black box with one temperature node and only the overall effective heat transfer coefficient ($(U \cdot A)_R$) can be obtained as a type output. If every heat transfer resistance would have been known (compare to equations (2.63) and (2.64) of section 2.3.3) it would be possible to calculate the surface temperature of the radiator which is at the same time the transition temperature. Hence an approximation had to be made. Since the surface temperature has to lie between the mean fluid temperature ($T_{R,m}$) of the radiator and the temperature of the surrounding (T_{sur}), the transition temperature ($T_{R,ex}$) is modeled as a mean temperature as follows.

$$T_{R,ex} = \frac{T_{R,m} + T_{sur}}{2} \quad (2.92)$$

With the mean fluid temperature:

$$T_{R,m} = \frac{T_{R,i} + T_{R,o}}{2} \quad (2.93)$$

Unfortunately, the utilization of equation (2.92) brings an inaccuracy with it, which becomes significant when no heat is supplied to the radiator and just the heat exchange with the surrounding is dominant (e.g. in summer). Otherwise the error is negligible. Problems, inaccuracies and the consequences of such kinds are addressed in section 3.4.2 in more detail and therefore not treated at this point. Despite the error that occurs, the model had been used for the exergy calculation and had been implemented into the EQUATION statement.

2.3.6 Hydraulics

Hydraulic components like mixing valves, circulating pumps and pipes are contributing to the energy and exergy balances. Due to this, the basic models as well as the exergetic assessment like in the previous sections are explained briefly. The main parts are taken from (SEL, 2012).

a) *Mixing valve and tee piece:*

The mixing valves (tee pieces), are modeled with the standard type "Type11h". Figure 2.21 displays the basic structure, the considered energy and exergy fluxes of the mathematical model.

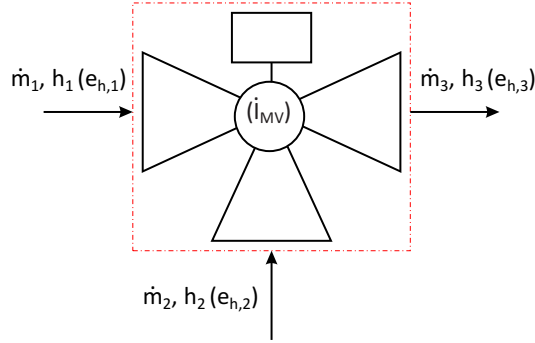


Figure 2.21: Energy and exergy fluxes of a mixing valve

According to figure 2.21, the energy balance for a simple tee piece can be found very quickly with the following expression.

$$\dot{m}_1 \cdot c_f \cdot (T_1 - T_{ref}) + \dot{m}_2 \cdot c_f \cdot (T_2 - T_{ref}) = \dot{m}_3 \cdot c_f \cdot (T_3 - T_{ref}) \quad (2.94)$$

With T_{ref} as reference temperature for enthalpy calculations. Rearranging equation (2.94), the outlet temperature can be calculated under consideration of $T_{ref} = 273.15 \text{ K}$ ($\vartheta_{ref} = 0^\circ\text{C}$). The temperatures T_1 , T_2 and the mass flows \dot{m}_1, \dot{m}_2 are input values for the TRNSYS type.

$$T_3 = 237.15 + \frac{\dot{m}_1 \cdot T_1 + \dot{m}_2 \cdot T_2}{\dot{m}_3} \quad (2.95)$$

The conservation of mass can then be written according to equation (2.2) of section 2.1.1 as follows.

$$\dot{m}_3 = \dot{m}_1 + \dot{m}_2 \quad (2.96)$$

Mixing processes are a source for irreversibilities and therefore taken into account. Experience tells that no real flow stream with the temperature T_3 obtained by mixing two flow streams with the temperatures $T_1 > T_2$ could have been observed unmixing itself without any intervention from the outside of the system boundary. Hence mixing processes are highly irreversible and remembering the Gouy-Stodola relation (equation (2.35) of section 2.2.6) are causing exergy destruction. An exergy balance can be formulated with equation (2.97) considering the enthalpy fluxes of figure 2.21 and equation (2.94) and the

exergy formulation of section 2.2.3.

$$\begin{aligned} \dot{I}_{MV} = & \dot{m}_1 \cdot c_f \cdot \left[(T_1 - T_0) - T_0 \cdot \ln \left(\frac{T_1}{T_0} \right) \right] + \dot{m}_2 \cdot c_f \cdot \left[(T_2 - T_0) - T_0 \cdot \ln \left(\frac{T_2}{T_0} \right) \right] \\ & - \dot{m}_3 \cdot c_f \cdot \left[(T_3 - T_0) - T_0 \cdot \ln \left(\frac{T_3}{T_0} \right) \right] \end{aligned} \quad (2.97)$$

Finally, the irreversibility of possible mixing processes can be calculated within TRNSYS.

b) *Pipes:*

Seasonal storage applications might contain the necessity of high storage volumes and collector areas. The connection distances for piping between a large collector field and the storage, heat exchangers and other components can reach significant values in terms of heat losses and thermal mass. Therefore pipes had been modeled with the non-standard type "Type709" obtained from the TESS library (TESS, 2012). The TESS library contains various models for different applications and components of thermal energy systems and more. For detailed information it is referred to (SEL, 2012) and (TESS, 2012). The following explanation of the mathematical aspects are taken from (SEL, 2012) and (TESS, 2012). Figure 2.22 shows again the structure, energy and exergy fluxes of the considered pipe model.

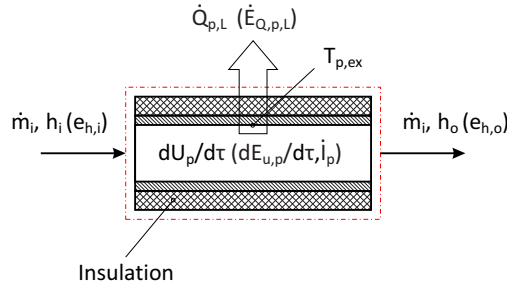


Figure 2.22: Energy and exergy fluxes of a Pipe

Type709 works with the so called "plug-flow" approach exactly identical to the standard type "Type31" (SEL, 2012). The difference between both types is that Type709 is able to compute the heat transfer coefficient for internal flow ($\alpha_{p,i}$) under consideration of the fluid properties and flow velocity with Nusselt- and Reynolds correlations. For Type31 however, a constant heat transfer coefficient ($U \cdot A$) has to be provided by the user. In order to understand the plug flow-model an example obtained from (TESS, 2012) should give some insight. A pipe should be considered, with three different mass segments of three different temperatures (T_1, T_2, T_3 in figure 2.23 case a)). If a mass segment according to $\dot{m}_i \cdot \Delta\tau$ with a temperature T_i enters the pipe, the same amount of mass is "pushed out" (see figure 2.23 case b)).

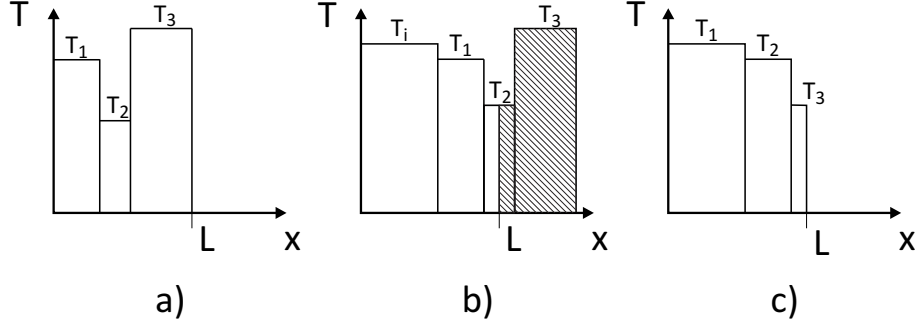


Figure 2.23: Plug flow approach of Type709 according to (TESS, 2012)

The conservation of mass has to be fulfilled hence it is possible that only a fraction of a segment leaves the pipe, in this case the segment T_2 . Case c) of figure 2.23 displays the final state where the new mass segment takes its place in the pipe. In this example, the outlet temperature (T_o) is then calculated as a mass-weighted mean value of the leaving segments according to equation (2.98).

$$T_o = \frac{m_3 \cdot T_3 + (\dot{m}_i \cdot \Delta\tau - m_3) \cdot T_2}{\dot{m}_i \cdot \Delta\tau} \quad (2.98)$$

Equation (2.98) can be written with a more general formulation as follows.

$$T_o = \frac{1}{\dot{m}_i \cdot \Delta\tau} \cdot \sum_{j=1}^{k-1} (m_j \cdot T_j + a \cdot m_k \cdot T_k) \quad (2.99)$$

Where a has to satisfy the following conditions.

$$\sum_{j=1}^{k-1} (m_j + a \cdot m_k) = \dot{m}_i \cdot \Delta\tau \quad (2.100)$$

$$0 \leq a \leq 1 \quad (2.101)$$

And finally the energy balance for each segment, considering the heat losses can be computed with expression (2.102).

$$m_j \cdot c_f \cdot \frac{dT_j}{d\tau} = - \underbrace{(U \cdot A)_j \cdot (T_j - T_{sur})}_{\dot{Q}_{p,L,j}} \quad (2.102)$$

Where T_{sur} denotes the temperature of the surrounding. The overall heat transfer coefficient ($(U \cdot A)_j$) can then be calculated with user provided fluid and pipe material properties. The heat transfer coefficient follows the well-known equation for cylindrical pipes (see e.g. (Incropera et al., 2011)) with the pipe's inner surface A as reference area.

$$(U \cdot A)_j = \frac{A}{\frac{1}{\alpha_{i,p}} + \frac{d_{p,i}}{2 \cdot \lambda_p} \cdot \ln \frac{d_{p,i}}{d_{p,o}} + \frac{d_{p,o}}{2 \cdot \lambda_{p,ins}} \cdot \ln \frac{d_{p,o}}{d_{p,ins}} + \frac{1}{\alpha_{o,p}}} \quad (2.103)$$

Where $d_{p,i}$, $d_{p,o}$, d_{ins} are denoting the inner pipe diameter, the outer pipe diameter and the insulation diameter respectively and have to be supplied by the user. The outside

heat transfer coefficient is described with $\alpha_{o,p}$ and has to be provided by the user as well as the thermal conductivity of the pipe λ_p and the insulation $\lambda_{p,ins}$. As mentioned before the inner heat transfer coefficient ($\alpha_{p,i}$) is calculated within Type709. For the derivation it is referred to (TESS, 2012) and not explained at this point. Within the plug flow model no mixing or conduction processes between adjoining nodes are accounted for.

The fact that the pipes are defined as general thermodynamic systems makes it necessary to perform an exergy assessment. According to figure 2.22 the exergy balance and hence the irreversibility can be found easily with equation (2.104).

$$\dot{I}_p = \dot{m}_i \cdot c_f \cdot \left[(T_i - T_o) - T_o \cdot \ln \left(\frac{T_i}{T_o} \right) \right] - \dot{Q}_{p,L} \cdot \left(1 - \frac{T_o}{T_{p,ex}} \right) - \frac{dE_{u,p}}{d\tau} \quad (2.104)$$

The exergy of the internal energy had to be calculated with a mean fluid temperature $T_{m,f}$ which is accessible as type output. The heat losses $\dot{Q}_{L,p}$ can also be obtained as an output from Type709. The capacitance of the fluid within the pipe at the current time step ($C_{f,p}$) had been manually calculated with the pipe's geometrical properties according to equation (2.105).

$$C_{f,p} = \rho_f \cdot c_f \cdot \frac{d_{p,i}^2 \cdot \pi}{4} \cdot L_p \quad (2.105)$$

Finally, the exergy of the internal energy for each segment can be again obtained analogous to equation (2.48) with the following expression.

$$\frac{dE_{u,p}}{d\tau} = C_{f,p} \cdot \frac{d}{d\tau} (T_{m,f} - T_o \cdot \ln T_{m,f}) \quad (2.106)$$

By expressing the derivation as finite differences, it is possible to implement equation (2.106) into the EQUATION statement of TRNSYS. It is clear that the utilization of the mean pipe temperature displays a quite inaccurate approximation if long pipe lengths are considered as it is the case of this work. The decision for this approach had been supported by the number of accessible outputs of Type709. $T_{f,m}$ is the only fluid temperature besides the inlet and outlet which can be obtained as an output. This approach might cause problems calculating the irreversibilities similar to the statements in section 2.3.5.

The next step is to define an appropriate transition temperature $T_{p,ex}$. Similar to equation (2.56) of section 2.3.2 the transition temperature had been computed with the following expression.

$$T_{p,ex} = T_{f,m} - \sum_j \dot{Q}_{p,L,j} \cdot \frac{1}{A \cdot \alpha_{i,p}} \quad (2.107)$$

Since only the overall heat transfer coefficient ($U \cdot A$) is accessible as an output, $\alpha_{i,p}$ has to be calculated by rearranging equation (2.103) within an EQUATION statement. Furthermore only the sum of the heat losses can be retrieved from Type709. Due to this, it becomes impossible to calculate the accurate respective transition temperature of each segment $T_{p,ex,j}$. As a consequence, a quite rough approximation had to be made with equation (2.107) to define a mean transition temperature $T_{p,ex}$. It is clear that this approach might cause inaccuracies calculating the irreversibilities as well, especially if the mass flow remains zero. These problems and difficulties will be addressed in section 3.4.2 briefly in more detail.

c) *Circulation pump:*

The circulation pump model which is utilized in this work is defined as variable speed pump with "Type3d". The mathematical approach is very simple. The user has to provide a maximum flow rate ($\dot{m}_{pu,max}$), the maximum electric pump power ($P_{pu,max}$), a control function (δ_{pu}) and a conversion factor (f_{pu}). The following explanations are again obtained from (SEL, 2012). Figure 2.24 shows the considered system and should elucidate the energetic and exergetic assessment.

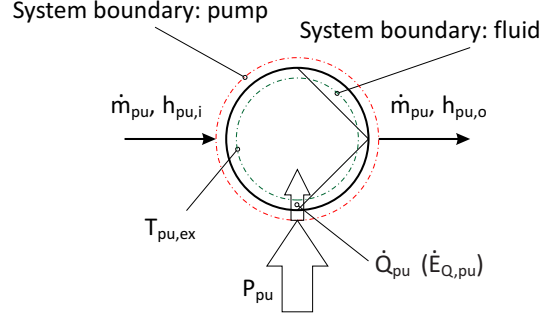


Figure 2.24: Model of circulation pump

The massflow rate (\dot{m}_{pu}) is described as linear function of δ_{pu} and $\dot{m}_{pu,max}$ and can be expressed with equation (2.108).

$$\dot{m}_{pu} = \delta_{pu} \cdot \dot{m}_{pu,max} \quad (2.108)$$

The control function has to serve the following condition.

$$0 \leq \delta_{pu} \leq 1$$

The consumed electrical power P_{pu} can be calculated analog to equation (2.108) as follows.

$$P_{pu} = \delta_{pu} \cdot P_{pu,max} \quad (2.109)$$

The conversion factor can be understood as the fraction of electrical power which is transformed into heat (\dot{Q}_{pu}) due to friction and applied to the flow which is pointed out in figure 2.24. Therefore the outlet temperature ($T_{pu,o}$) of the pump can be computed considering this heat transfer.

$$T_{pu,o} = T_{pu,i} + \frac{P_{pu} \cdot f_{pu}}{\dot{m}_{pu} \cdot c_f} \quad (2.110)$$

Unfortunately, the mathematical model of Type3d does not account for the increase of the total enthalpy of the flow stream ($h_{tot} = h + \frac{v^2}{2}$, see also section 2.1.2). In other words it can be said, that the kinetic energy and the pressure increase are not accounted for within the outlet enthalpy of the flow stream. Therefore, only the transformed heat from equation (2.110) can be considered in the energy and exergy balances. An exergy assessment of the pump model had not been performed in the way the other components were treated since pumps are playing a minor role in this work and it is not the task to find the optimal pump type or design. Another aspect is that the required pump power is rather low and hence the heat applied. However for the global energy and exergy balances of the overall and the subsystems (space heating (SH), domestic hot water (DHW), solar

loop (SL), storage (ST)) the exergy of \dot{Q}_{pu} is considered where necessary with equation (2.111).

$$\dot{E}_{Q,pu} = \dot{Q}_{pu} \cdot \left(1 - \frac{T_0}{T_{pu,ex}}\right) \quad (2.111)$$

Due to the lack of detailed information about the heat transfer inside the pump. The transition temperature is simply modeled as the arithmetic mean of the inlet ($T_{pu,i}$) and the outlet temperature ($T_{pu,o}$).

2.4 Performance indicators

Characteristic parameters and performance indicators can be useful tools in terms of benchmarking different principles and technologies not only in thermal engineering. It is often desired to display the performance of technologies just with a few or even one characteristic number. A commonly accepted set of indicators for thermal energy storage applications is difficult to find since there are a variety of characteristics for example economical (accepted costs per storage cycle), ecological (CO_2 emission, life cycle analysis), of course energetic and exergetic performances, solar fractions, user comfort, storage densities and more, which can follow opposing trends. An example for the controversy of this topic can be found in a presentation given by Christoph Rathgeber from ZAE Bayern during TASK4229 in Ljubiana in 2013. Rathgeber stated that the acceptable investment costs depending on the storage period are rather low for seasonal storage applications in general (Rathgeber and Eberhard, 2013). This aspect might state a major challenge for the considered PCM TES considered in this work. A currently running inquiry (as in 2013) by Rathgeber should evaluate the actual costs of different storage technologies in terms of material costs, concept (PCM, water, adsorption, absorption), operational costs and more. It is clear that not all of these aspects can be covered in this thesis. Therefore, already known performance indicators and efficiencies are utilized in this work to evaluate the reference and the PCM technology. The considered parameters include energetic and exergetic efficiencies (section 2.4.1), storage density (section 2.4.2) as well as the solar fraction and penalty functions (section 2.4.3). Economical and ecological aspect are not considered.

2.4.1 Energetic and exergetic efficiency

The comparison of the conventional and the PCM based system should be performed with the energetic and exergetic efficiencies of the overall system. In order to elucidate the effect of changing control strategies and different storage technologies on subsystems (e.g. DHW loop) and active elements (e.g. storage, heat exchanger), the following efficiencies had been applied on any of these components. The simplest definition for an efficiency, energetically or exergetically can be defined as follows (Baehr and Kabelac, 2009).

$$\eta = \frac{\text{energetic benefit}}{\text{energetic effort}} = \frac{Q_{use}}{Q_{eff}} \quad (2.112)$$

$$\psi = \frac{\text{exergetic benefit}}{\text{exergetic effort}} = \frac{E_{use}}{E_{eff}} \quad (2.113)$$

Where η and ψ denote the energetic and exergetic efficiency respectively. The equations (2.112) and (2.113) had been used for components where the change of internal energy can

be neglected compared to the effort and the useful energy gain. The thermal masses of the subsystems and the overall system are not insignificant, however the change after a one year period is almost zero (since the system reaches the same state as in the beginning). Hence the aforementioned definitions can be utilized on a system level as well. When it comes to thermal storage it is clear that the thermal capacitance has to be accounted for in efficiency considerations. (Dincer and Rosen, 2011) provided four cases (case A,B,C and D) for an overall analysis of thermal storages. These cases are not derived in detail at this point, but the selection of the most applicable definition should be explained briefly. For more information and a detailed explanation it is referred to (Dincer and Rosen, 2011). The explanations are performed only for the energetic efficiencies since the considerations for exergy and energy are almost identical. The mathematical expressions are given for both forms. Possible differences between energetic and exergetic considerations are discussed explicitly. The first case can simply be written analogous to equations (2.112).

$$\eta_A = \frac{\text{Energy recovered}}{\text{Energy input}} = \frac{Q_{dis}}{Q_{ch}} \quad (2.114)$$

$$\psi_A = \frac{\text{Exergy recovered}}{\text{Exergy input}} = \frac{E_{dis}}{E_{ch}} \quad (2.115)$$

The indices "dis" and "ch" are denoting "discharge" and "charge". Case A only considers the output and the input of the storage. Case B on the other hand, considers the change in internal energy (ΔU).

$$\eta_B = \frac{\text{Energy recovered} + \text{Energy accumulation}}{\text{Energy input}} = \frac{Q_{dis} + \Delta U}{Q_{ch}} \quad (2.116)$$

$$\psi_B = \frac{\text{Exergy recovered} + \text{Exergy accumulation}}{\text{Exergy input}} = \frac{E_{dis} + \Delta E_u}{E_{ch}} \quad (2.117)$$

Case C is taking the the initial amount of energy in the store (U_i) as an asset.

$$\eta_C = \frac{\text{Energy recovered}}{\text{Energy input} + \text{Initial energy in store}} = \frac{Q_{dis}}{Q_{ch} + U_i} \quad (2.118)$$

$$\psi_C = \frac{\text{Exergy recovered}}{\text{Exergy input} + \text{Initial exergy in store}} = \frac{E_{dis}}{E_{ch} + E_{u,i}} \quad (2.119)$$

Case D accounts for the final (U_f) and the initial state (U_i) of the storage.

$$\eta_D = \frac{\text{Energy recovered} + \text{Final energy in store}}{\text{Energy input} + \text{Initial energy in store}} = \frac{Q_{dis} + U_f}{Q_{ch} + U_i} \quad (2.120)$$

$$\psi_D = \frac{\text{Exergy recovered}}{\text{Exergy input} + \text{Initial exergy in store}} = \frac{E_{dis} + E_{u,f}}{E_{ch} + E_{u,i}} \quad (2.121)$$

According to (Dincer and Rosen, 2011), the application of the most suitable cases depends on three different operating modes of the storage. These three modes are defined as $\Delta U < 0$, $\Delta U = 0$ and $\Delta U > 0$. The three modes are valid for the exergy consideration in an analogous way and therefore not explained separately. For case A , it is possible to yield efficiency values

over one which of course violates the first law, if $\Delta U < 0$. This irregular value can occur if more energy (or exergy) (Q_{dis} , E_{dis}) is withdrawn by decreasing the internal energy of the thermal storage as energy (or exergy) (Q_{ch} , E_{ch}) is applied to the storage. Case B and D are appropriate if $\Delta U > 0$ and $\Delta U < 0$, where A and C can be misleading because the change in internal energy is not accounted for. If the internal energy reaches the initial point (full storage cycle, $\Delta U = 0$) any of those cases provide appropriate values of the same magnitude. The last point is interesting for the evaluations made in this paper because one year storage periods are considered which displays a full storage cycle. For comparison, energetic efficiency analysis for different storage types had been also performed by (Moser, 2012). Energetic and exergetic efficiency analysis of a small scale PCM storage had been carried out by (Brandstätter, 2014) in the course of the COMTES project as well.

2.4.2 Storage density

The storage density as mentioned in the introduction, is a significant factor when it comes to seasonal storage applications since storage volumes can be rather high. In order to evaluate the improvement of new storage concepts, different storage density parameters are obtained from literature and described briefly in this section. The storage density indicators are obtained from (Wilhelms et al., 2009).

a) *Physical storage density* (S_{phys}):

The physical storage density describes the theoretical possible energy per cubic meter storable in a storage medium (water, SAT). This relation can be written with equation (2.122).

$$S_{phys} = \frac{Q_{med}}{V_{med}} \quad (2.122)$$

The storable sensible energy of the material (Q_{med}) can be calculated by defining reasonable boundary temperatures (e.g. for water, $\vartheta_{up} = 100^\circ\text{C}$ and $\vartheta_{low} = 4^\circ\text{C}$).

$$Q_{med} = m_{med} \cdot c_{med} \cdot (T_{up} - T_{low}) \quad (2.123)$$

With the mass of the medium m_{med} , the specific heat c_{med} and the upper and lower boundary temperatures T_{up} , T_{low} . In terms of PCM, the latent heat of course has to be considered (see section 2.2.5).

b) *Effective storage density* (S_{eff}):

The effective storage density accounts for additional measures which have to be taken in order to maintain the function of the storage system. Therefore a storage volume V_{st} is defined and contains the material volume (V_{med}), possible unused space within the storage, insulation, storage wall thickness and possible built in components (e.g. heat exchangers, stratifying units). In addition the volume of the periphery (V_{per}) is considered and contains the piping, pumps, valves etc. and their insulation. Hence it can be written.

$$S_{eff} = \frac{Q_{med}}{V_{st} + V_{per}} \quad (2.124)$$

c) *Actual storage density* (S_{act}):

The last definition is the actual storage density. This factor accounts for a possible emerging unusable space (V_{un}) due to maintenance or deconstruction requirements.

$$S_{act} = \frac{Q_{med}}{V_{st} + V_{per} + V_{un}} \quad (2.125)$$

In order to support the interpretation of those indicators it is required to mention the considered boundary conditions when presented.

2.4.3 Solar fraction and penalty functions

An important factor in designing solar thermal systems is the well known solar fraction f_{sol} . Depending on how the system boundaries are drawn, different definitions of solar fractions can be given (see for example (Heimrath, 2004)). In this work it describes the relation between the actual useful energy retrieved for SH and DHW demands from the solar system and the fraction of auxiliary energy supplied by an electric heater or a conventional boiler. Therefore the amount of heat demand which is actually covered by solar energy is represented. This relation can then be written as follows (Stieglitz and Heinzl, 2012; Heimrath, 2004).

$$f_{sol} = 1 - \frac{Q_{aux} + Q_{pen,DHW} + Q_{pen,SH}}{Q_{use,DHW} + Q_{use,SH}} \quad (2.126)$$

With $Q_{use,DHW}$ denoting the retrieved energy for hot water preparation, $Q_{use,SH}$ describing the space heating demand and Q_{aux} the auxiliary energy. In equation (2.126) two new parameters, the so called "penalty functions" for domestic hot water ($Q_{pen,DHW}$) and space heating ($Q_{pen,SH}$) are introduced. These penalties had been proposed by (Weiss et al., 2003) in order to assure sufficient dimensioning of solar combi systems and to account for the users comfort. If the required boundary conditions are not met, in this case the hot water temperature ($\vartheta_{set,DHW} = 45^\circ\text{C}$) and/or the required room temperature ($\vartheta_{set,room} = 19.5^\circ\text{C}$), the penalties are calculated and treated as an auxiliary heat demand. The penalty function for the DHW demand is defined by the following expression, calculated in every timestep and then integrated over the simulation period (τ) (Weiss et al., 2003).

$$Q_{pen,DHW} = \int_0^\tau \dot{m}_{DHW} \cdot c_f \cdot [\Delta T_{pen,DHW} + (\Delta T_{pen,DHW} + 1)^{x_{DHW}} - 1] d\tau \quad (2.127)$$

With the following definition of $\Delta T_{pen,DHW}$:

$$\max(0; \vartheta_{set,DHW} - \vartheta_{act,DHW}) \quad (2.128)$$

The temperature difference function from equation (2.128) describes the deviation from the required set point. The maximum function ensures that only a lack of energy is accounted for. If now, a lack of energy supply occurs the actual difference between supply and demand (linear term in equation (2.127)) is extended with an exponential function to account for not meeting the user requirements. The exponent (x_{DHW}) had been chosen to 4 according to (Weiss et al., 2003) which displays a quite strict assumption. The addition and subtraction of 1 in equation (2.127) has the reason of maintaining a monotonic and continuous function in special cases (Weiss et al., 2003). A similar function had been defined in order to account for the space heating demand as follows.

$$Q_{pen,SH} = \int_0^\tau (U \cdot A)_{build} \cdot \max[0; \Delta T_{pen,SH} + (\Delta T_{pen,SH} + 1)^{x_{SH}} - 1] d\tau \quad (2.129)$$

With $\Delta T_{pen,SH}$ defined as:

$$\max(0; \vartheta_{set,room} - \vartheta_{act,room}) \quad (2.130)$$

The heat transfer coefficient of the building is denoted with $(U \cdot A)_{build}$ and had been obtained by assuming the same temperature difference between indoors and outdoors, applies for the considered parts of the reference building. By equating the the entire losses and the partial losses, the following expression for $(U \cdot A)_{build}$ can be found.

$$(U \cdot A)_{build} = (U \cdot A)_{win} + (U \cdot A)_{frame} + (U \cdot A)_{ext,wall} + (U \cdot A)_{roof} \quad (2.131)$$

Where the subscripts "*win*", "*frame*", "*ext,wall*" and "*roof*" denote the heat transfer coefficients of windows, the window frame, the exterior walls and the roof respectively. The data can be obtained from section 3.1.1 and (Bertsch et al., 2013). The space heating penalty exponent (x_{SH}) had been chosen to 2 according to (Weiss et al., 2003; Heimrath and Haller, 2007). The maximum function should avoid negative penalty values. The meaning of the linear and the exponential term are analog to the explanations above. (Weiss et al., 2003) provided SH penalties if $\vartheta_{act,room}$ exceeds a certain threshold in order to account for over heating, but had not been utilized in this work because no active cooling had been considered. At this point the main premise of the system design in this work can be defined. As a consequence of the seasonal application, a solar fraction of $95 \pm 2\%$ should be the goal of the reference and the PCM systems.

2.5 Simulation tool TRNSYS 17.1

The simulation program TRNSYS (Transient System Simulation) had been originally developed at the Solar Energy Laboratory (SEL) of the University of Wisconsin (USA). The simulation environment provides the possibility to perform transient calculations of various forms of energy systems (e.g. solar energy systems, conventional heating systems, wind energy conversion etc.), their components (e.g. TES, heat exchangers, solar collectors, etc.) as well as building structures in dependence of their environment (climate data) (SEL, 2012). In this work the version TRNSYS 17.1 had been used for the calculations. This section should give a short introduction into the important aspects of the simulation program regarding this thesis. Further information can be found for example in (Heimrath, 2004), (Blanco, 2012) and (SEL, 2012).

2.5.1 Simulation Studio and TRNSYS-types

The graphical user interface (GUI) of TRNSYS is called "Simulation Studio". It can be understand as a sort of canvas where the different mathematical models, the already known "types", are placed via "drag and drop". Figure 2.25 shows a screenshot of the utilized simulation studio. On the right side, the variety of type libraries can be noticed. Connected types of a system simulation can be seen in the center. The standard types come along with the TRNSYS program. Non-standard types for special applications or a different level of detail can either be provided by institutions as it is the case with the TESS libraries (Thermal Energy Systems Specialists, (TESS, 2012)) or developed individually. In the 17.1 version, the types are implemented in FORTRAN90, older versions work with FORTRAN77.

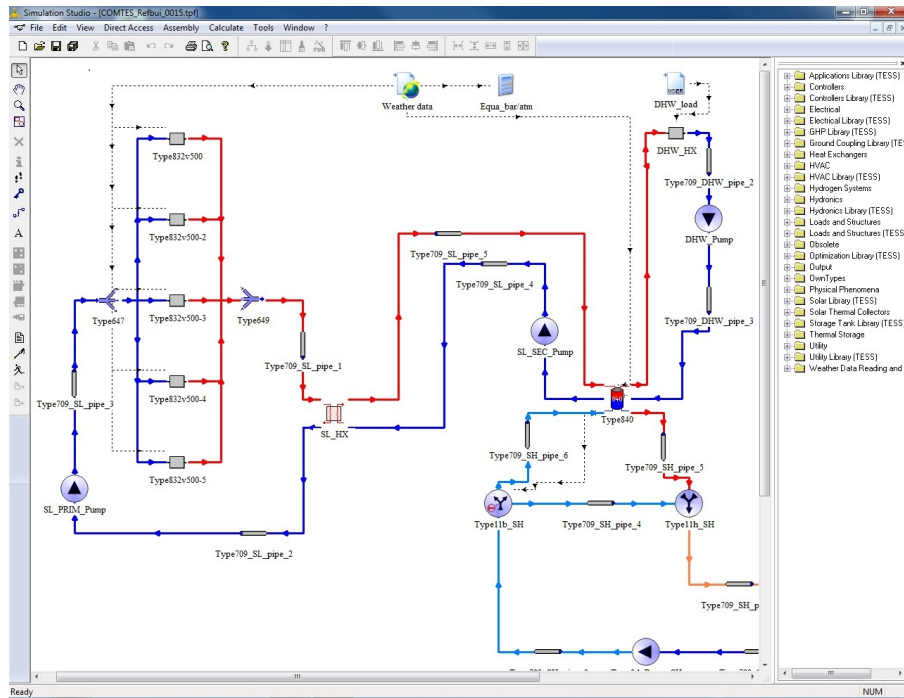


Figure 2.25: Screenshot of the Simulation Studio

TRNSYS uses a modular approach. These modules are called "types" and represent the physical models of the different system components. These types are interlinked with each other in order to assemble the desired system. The output of one type provides the input for another. For example, the outlet temperature of a heat exchanger type becomes the inlet temperature for a storage type. The user has to ensure that the hydraulic circuit between the connected types is closed to avoid a violation of mass conservation. In general TRNSYS does not check mass or energy balances therefore it has to be performed by the user. Every type has a so called "Proforma" (figure 2.26) which serves as some kind of form where necessary parameters can be entered and/or changed. The Proforma gives insight into the required inputs and accessible outputs as well as special applications of the considered type.

Parameter	Input	Output	Derivative	Special Cards	External Files	Comment
1	Number in series	1	-	-	-	More... <input checked="" type="checkbox"/> Macro
2	Collector area	1	m ²	-	-	More... <input checked="" type="checkbox"/>
3	Fluid specific heat	4.190	kJ/kg.K	-	-	More... <input checked="" type="checkbox"/>
4	Efficiency mode	1	-	-	-	More... <input checked="" type="checkbox"/>
5	Tested flow rate	40.0	kg/hr.m ²	-	-	More... <input checked="" type="checkbox"/>
6	Intercept efficiency	0.80	-	-	-	More... <input checked="" type="checkbox"/>
7	Efficiency slope	13.0	kJ/hr.m ² .K	-	-	More... <input checked="" type="checkbox"/>
8	Efficiency curvature	0.05	kJ/hr.m ² .K ²	-	-	More... <input checked="" type="checkbox"/>

Figure 2.26: Proforma of a TRNSYS type

The information of the utilized types, their connections and the simulation parameters are stored in the so called "DECK" file. This file collects all the required information which is used in the simulation and is sent to the program kernel where the calculations are performed (Heimrath, 2004). The calculation is performed in a specific order which can be changed by the user if desired. During one timestep iterations are performed until a convergence

criterion is met. If this is not the case, the next iteration begins, but only components which had not converged in the previous iteration, are recalculated (Moser, 2012).

2.5.2 The EQUATION statement

The EQUATION statement as mentioned in the sections above had been utilized to perform the exergetic and energetic evaluation of the systems and their components. Within the EQUATION statement it is possible to include user defined arithmetic equations and let them interact with TRNSYS types. These interactions can be for example special control strategies, elementary Boolean operations like "greater than" statements, unit conversions or other simple calculations. Figure 2.27 shows the graphical user interface of EQUATION which might remind on a pocket calculator.

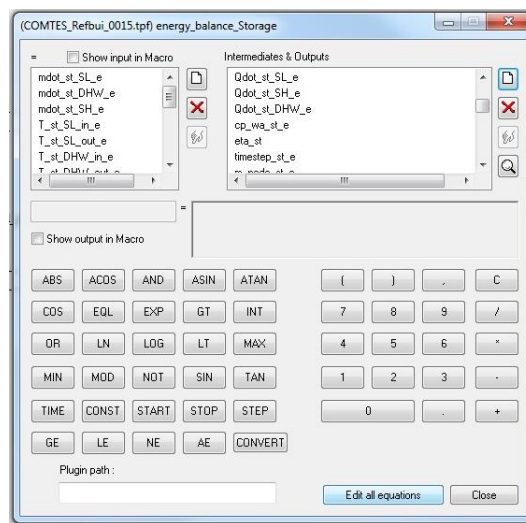


Figure 2.27: GUI of the EQUATION statement

The equation statement is used like a type. It can be placed in the Simulation Studio via drag and drop and linked to the considered TRNSYS types. The defined inputs can be added and named in the left window in figure 2.27. On the right side, the outputs and equations can be found. The exergy balances described in the previous sections had been entered into the EQUATION statement and printed to text files for further processing. Implementing control strategies via the EQUATION statement, might cause stability problems if the control function become complex.

2.5.3 Loads and structures with TRNBUILD

Behind every heating system there is a structure serving as boundary and dimensioning condition. The user interface TRNBUILD provides a very useful tool in order to define the desired building. TRNBUILD gives the possibility to define "Multizone Buildings" considering internal and electrical gains. Multizone buildings can be described as structure with several so called "Airnods" at which the entire thermal capacity is lumped. These Airnodes can represent for example one single storey or several nodes can be defined within a room. Figure 2.28 shows the graphical user interface of a zone within a defined building.

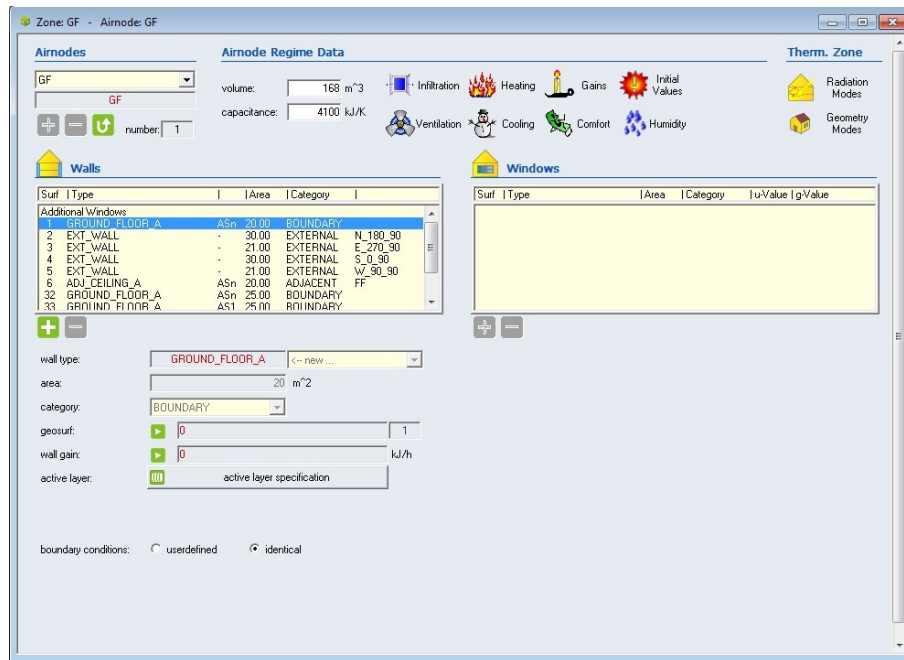


Figure 2.28: Regime data of a building Airnode within TRNBUILD

In this user interface it is possible to define for instance the wall structure and its thermal properties, internal gains, humidity and comfort considerations, ideal heating and cooling as well as long wave radiation models and infiltration and ventilation aspects. The geometry of the considered structure can be defined in Google SKETCHUP (SketchUp, 2014) as a three dimensional model and subsequent imported into TRNBUILD. The three dimensional aspect provides the basis for detailed long wave radiation calculations and shading. The information generated by TRNBUILD is simply written in a text file with the ending "B17" which can be implemented into the Simulation Studio via "Type56". Type56 can interact with other system components and climate data due to inputs and outputs as mentioned in section 2.5.1. (SEL, 2012)

3 GENERAL ASPECTS AND BOUNDARY CONDITIONS

This section should collect all the boundary conditions and other aspects which had been applied for every system simulation throughout this work. In section 3.1 a description of the utilized reference building, the demands and gains should give some understanding of the structural boundary conditions. The considered environmental boundary conditions in form of climate data files as well as the reference state for exergy calculations are briefly introduced in section 3.2. A short explanation of the utilized phase change material is provided in section 3.3. Section 3.4 sums up general simulation parameters and furthermore it should give an overview on problems and difficulties which occurred during the simulation and evaluation work.

3.1 The reference building

A reference building model serves as boundary condition for the space heating loop and determines the demand in dependence of external and internal influences. The external influences are described by weather data such as solar irradiation and ambient temperatures. The internal gains from electrical devices and persons contribute to the energy demand of a building as well. The domestic hot water demand states an additional load case for a solar thermal system. Since it is always difficult to determine the user behaviour, representative functions have to be utilized in system simulations. These boundary data had been determined in Work Package 1 (WP1) of the COMTES project in advance to this thesis and therefore had not been part of this work. The following information had been obtained from (Bertsch et al., 2013).

3.1.1 Single family house

The reference building had been basically taken from the definitions made during TASK32 (Heimrath and Haller, 2007). As structural boundary condition, a free standing two storey single family house (SFH) without a basement had been selected. Each storey had been implemented as one zone in TRNBUILD. A multizone approach provides the possibility to account for air coupling between the two storeys as well as the long wave radiation distribution within the zones in a more realistic way. The geometric model had been generated with Google SKETCHUP and is shown in figure 3.1. A balcony had been added on the south side of the building which has shading effects on the lower windows.

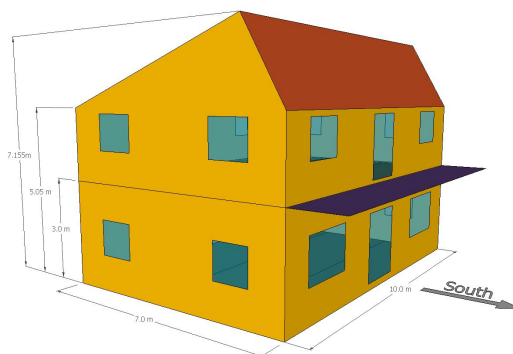


Figure 3.1: Geometrical model of the reference building (Bertsch et al., 2013)

The fraction of the glazed vertical wall area equals to 13 %. The angle of the south oriented roof area equals 20°, the north oriented one results in 60°. With a length (L) of 10 m and

a width (W) of 7 m the total floor area of the two storeys result in 140 m². A summary of further basic geometrical data had been obtained from (Bertsch et al., 2013) and can be taken from table 3.1. The net wall area (A_{net}) is defined as the entire wall area excluding the glazed area (A_{win}).

Table 3.1: Wall areas of the reference building according to their orientation (Bertsch et al., 2013)

orientation	ground floor		first floor	
	A_{net}	A_{win}	A_{net}	A_{win}
	m ²	m ²	m ²	m ²
North	28.20	1.80	19.18	1.32
East	18.90	2.10	19.42	2.30
South	22.50	7.50	15.66	4.84
West	18.90	2.10	19.42	2.30
Roof North	-	-	61.56	-
Roof South	-	-	24.31	-
Ground floor	70.00	-	70.00	-
Σ	158.50	13.50	143.68	10.76

The thermal properties of the wall constructions had been chosen in a way that a heating demand results in 36.3 kWh/m² in a reference climate of Zurich (see section 3.2). A detailed wall construction can be obtained from (Bertsch et al., 2013), in table 3.2 only the overall heat transfer coefficients (HTC, U) and the wall thicknesses (s) as well as the window characteristics are given to provide an impression of the thermal properties.

Table 3.2: Thermal properties of the respective wall types and windows (Bertsch et al., 2013)

wall type	heat transfer coefficient	layer thickness	solar transmittance
	U	s	g
	W/(m ² K)	m	-
External	0.200	0.408	-
Roof	0.215	0.295	-
Ground floor	0.189	0.405	-
Adjacent ceiling	0.860	0.280	-
Window frame	1.980	-	-
Window	1.100	0.023	0.609

The interaction of the ground floor with the environment had been neglected by setting the boundary conditions of this wall component to "identical" in the TRNBUILD interface. Hence the HTC for the ground floor in table 3.2 has no effect. In order to account for air coupling between the outside and the inside of the building ventilation and infiltration had been considered. The air flow due to leakage had been assumed with a constant air change rate of 0.4 h⁻¹. The ventilation is a little bit more complex because it has to somehow represent a user behaviour. This had been realised by defining two tilted windows and one

balcony door for each floor. The windows and balcony doors had been modelled with the non-standard type "Type358" which is not discussed in detail at this point. The control signal for this passive cooling is switched on if the following conditions are met (Bertsch et al., 2013).

- The time is between 9 p.m. and 8 a.m.
- The average ambient temperature of the last 24 hours was above 12 °C.
- The room temperature is higher than 24 °C.
- The ambient temperature is a least 2K below room temperature

Other cooling devices had not been implemented. Since the building had been set up in the course of the COMTES project before this thesis, it is not discussed in detail in this work. For further information it is referred to (Bertsch et al., 2013).

3.1.2 Domestic hot water demand and internal gains

As a load case, the domestic hot water demand can be a crucial point in systems performance evaluation since the energy rates can get quite high according to short draw off periods and a rather high temperature level. The draw off profile considered for the simulations had been basically obtained from TASK32 (Heimrath and Haller, 2007) with a constant fresh water temperature as minor simplification. It is based on a statistical approach with the basic parameters displayed in table 3.3 and obtained from (Heimrath and Haller, 2007).

Table 3.3: Basic data of the DHW demand (Heimrath and Haller, 2007)

hot water temperature	fresh water temperature	minimum flowrate	maximum flowrate	daily average draw off
ϑ_h	ϑ_{cw}	\dot{m}_{min}	\dot{m}_{max}	\dot{V}_{avg}
°C	°C	kg/h	kg/h	l/d
45	10	60	1332	200

The DHW load cases are available as a text file containing the required massflow in 6 min timesteps. This load file is implemented via a data reader (Type9,(SEL, 2012)) and simply connected to the DHW heat exchanger (Type805) as input on the cold side. Type805 then calculates the necessary hot side massflow in order to achieve the set point temperature of 45 °C. The resulting hot water demand per week of the year can be observed in figure 3.2.

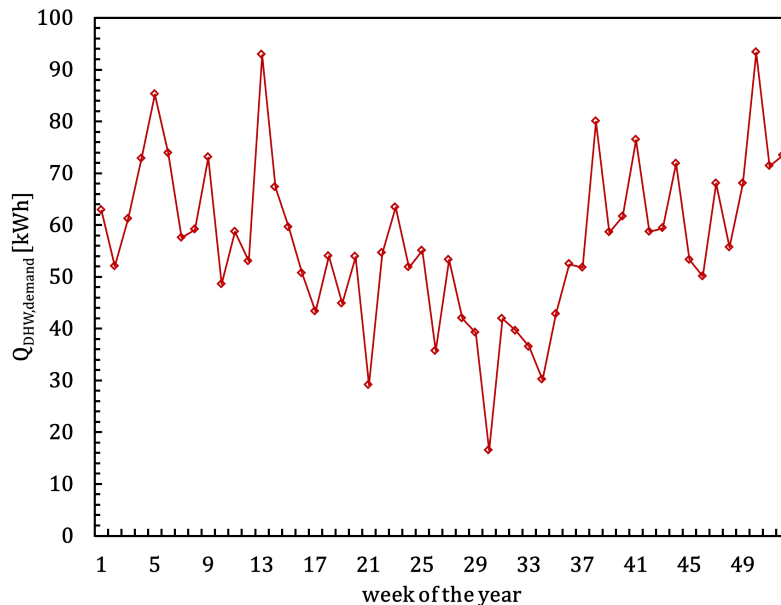


Figure 3.2: Weekly integrated energy demand for hot water preparation

In order to account for internal heat gains caused by persons and electrical devices, data files utilized in TASK32 (Heimrath and Haller, 2007) according to ISO 7730 for a person who is seated at rest, had been agreed on in this project. The heat gain and its distribution is displayed in table 3.4.

Table 3.4: Heat gain distribution per person seated at rest according to (Heimrath and Haller, 2007)

heat gain			
\dot{Q}_{pers}			
W			
convective	radiative	latent	Σ
40	20	40	100

The data from table 3.4 are multiplied with a person occupancy schedule provided by TASK32 (Heimrath and Haller, 2007). The resulting heat gain is then equally distributed to the ground and the first floor of the reference building. Figure 3.3 shows the actual heat gain (black line) in correspondence to the persons occupied (bars) during one day.

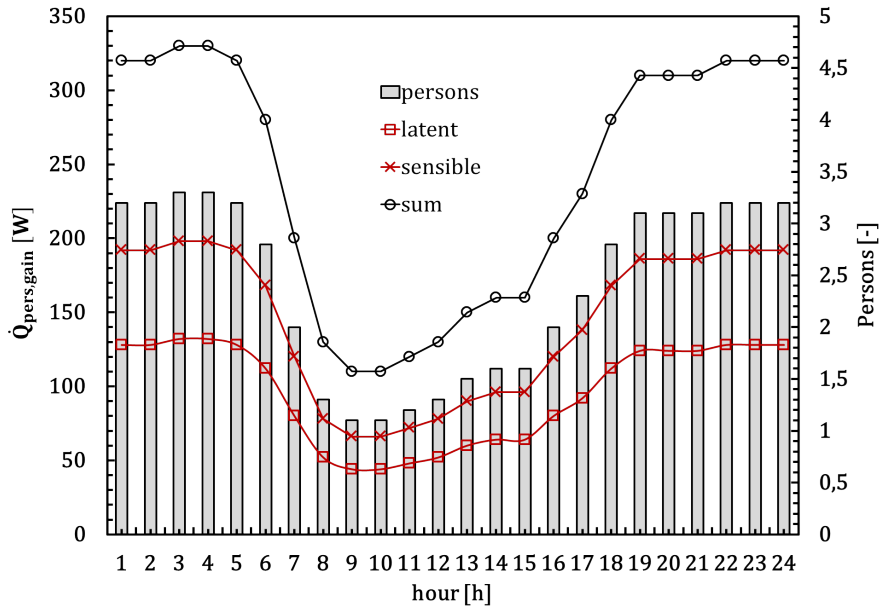


Figure 3.3: Daily heat gain and occupation obtained from (Heimrath and Haller, 2007)

This schedule repeats itself periodically. The electrical gains caused by for example computers, had been obtained from the TASK32 (Heimrath and Haller, 2007) descriptions as well. The implementation into TRNSYS is identical to the aforementioned procedure. Figure 3.4 displays a one week period of the heat gain schedule. After a week has gone by, the schedule repeats itself.

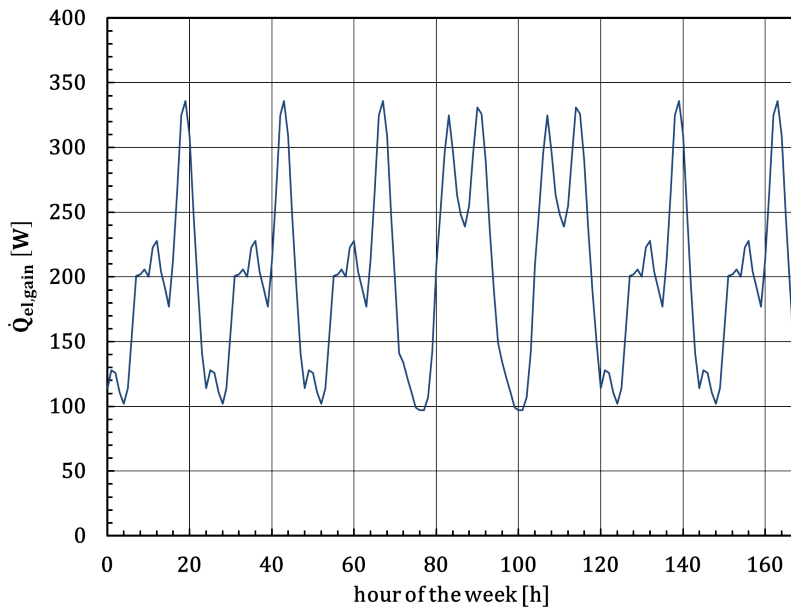


Figure 3.4: Weekly schedule of electrical gains (Heimrath and Haller, 2007)

3.2 Climate data and reference state

The climate data represents the essential boundary conditions for transient thermal energy system simulations. Especially for system performance estimations it becomes necessary to utilize climate data in order to represent the daily and of course seasonally deviations of ambient temperature and solar irradiation. These climate files can be obtained from data generators like "Meteonorm7" which provide data from a vast amount of weather stations over the world (Remund et al., 2013). The calculation of a set of weather data for any particular location is obtained by interpolating data from the nearest stations. The resulting data file represents a reference year considering weather data from the past several years. In this work a Meteonorm data file of Zurich had been utilized and implemented via a weather data reader (Type15) (SEL, 2012). The selection of this particular location had been motivated by the fact that the annual heating demand of the reference building was based on the Zurich climate. A summary of the used climate data can be found in appendix A. To give an impression, figure 3.5 displays the monthly average global horizontal radiation G_h and ambient temperature ϑ_{amb} for the location of Zurich.

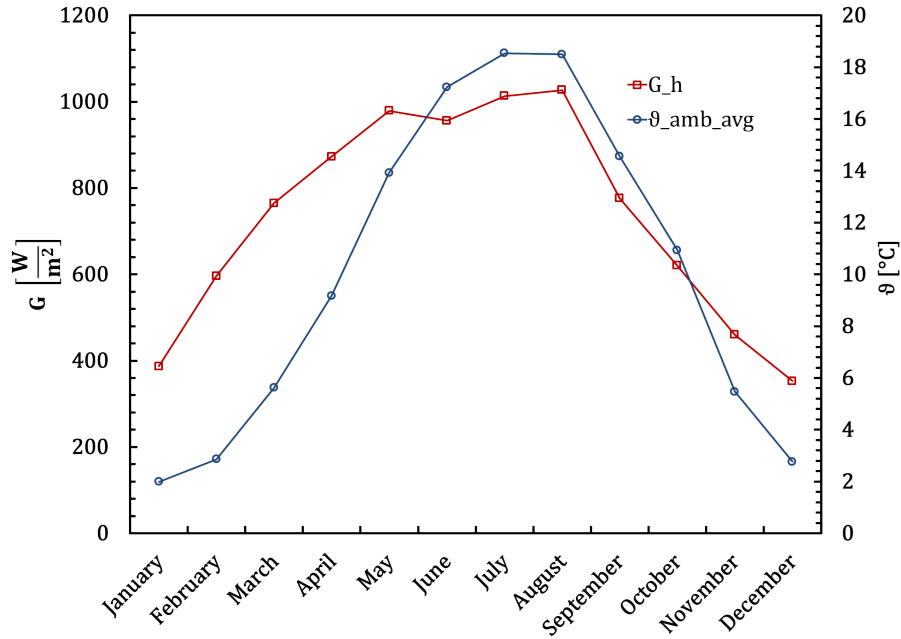


Figure 3.5: Monthly horizontal irradiation and average temperature of Zurich

The reference state needed for exergy calculations is tightly related to the chosen environmental conditions, especially to the ambient temperature (see also section 2.2.2). Although there are more detailed models to define a reference environment (Dincer and Rosen, 2011), only a constant reference temperature T_0 had been chosen to represent the reference state for exergy considerations. The fact that no chemical reactions between the considered heating system can occur (or modelled with a reasonable effort) and no mechanical work can be transported by volume change (density of the HTF is assumed constant and in closed rigid containments) supported this decision. In order to represent the actual environment and avoid algebraic sign problems (negative exergy), the lowest ambient temperature in the data file had been selected as reference temperature. Hence the reference temperature T_0 results in 263.15 K for the Zurich climate file. It had been necessary to define a ground

temperature as boundary condition for distinguished pipes defined in the system simulations (see section 4). This had been realised with the standard type "Type77". Type77 models the ground temperature for different depths with a sinusoidal characteristic depending on ambient temperature. For a detailed type description it is referred to (SEL, 2012). The ground temperature model requires parameters like amplitude, timeshift and the mean ambient temperature to define the surface temperature characteristic. The calculation of the required parameters had been performed by using the "least mean square" method to fit a sinusoidal curve (red line) into the ambient temperature characteristic of the Zurich weather file (blue line). The resulting surface temperature curve is displayed in figure 3.6 with a timeshift of about 18 days and an amplitude of 8.6°C .

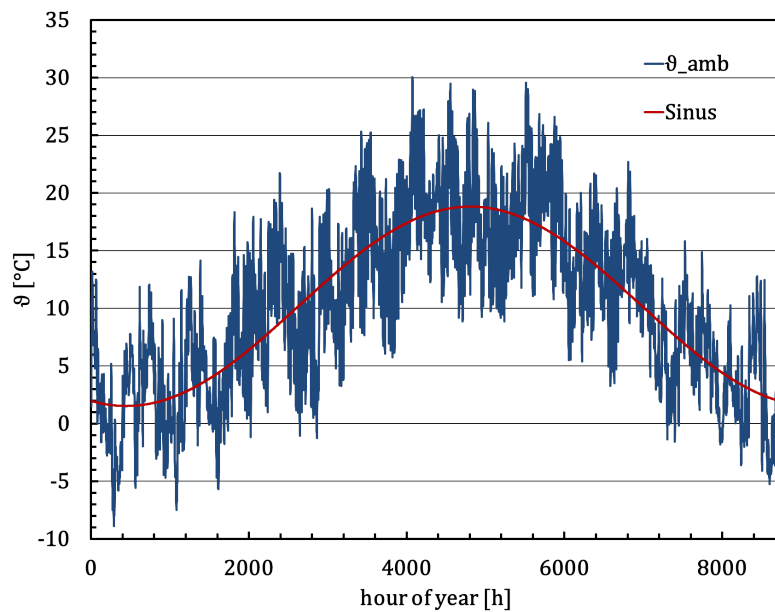


Figure 3.6: Ambient temperature characteristic over the year and calculated sinus curve

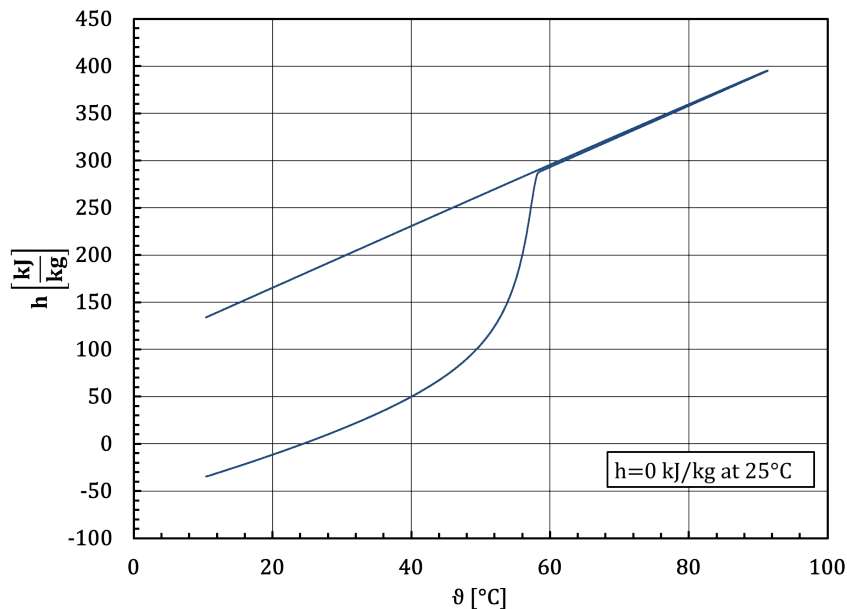
3.3 The phase change material

This section should provide the basic thermophysical properties of the phase change material used, detailed information on chemical structure, crystallisation and melting behaviour etc. can be obtained for example from (Lane, 1983) and (Dröscher, 2012). As mentioned in the introduction, a salt solution Sodium Acetate Trihydrate ($\text{NaCH}_3\text{COO} \cdot 3\text{H}_2\text{O}$) with a water fraction of 46 %wt. is investigated. Material properties of SAT can be obtained from literature but differ in a wide range. As literature sources can be stated (Sandnes, 2003), (Araki et al., 1995), (Fan et al., 2010) and (Lane, 1983). The utilized data for the numerical model can be obtained from table 3.5 and should represent the magnitude of the chosen properties since the differences in literature are significant.

Table 3.5: Material properties of the considered PCM

density solid	density liquid	thermal conductivity
ρ_s	ρ_l	λ
kg/m ³	kg/m ³	W/(m K)
1.4	1.2	0.4

For the calculations only the density in the solid state is considered since the volume change during phase transition is neglected. Regarding the mathematical model (see section 2.3.3) the h/T characteristic is important to determine the state of the phase change material. Figure 3.7 provides an h/T characteristic of the considered material measured with the "Differential Scanning Calorimetry Method" (DSC) at the "Fraunhofer-Institut für Solare Energiesysteme" (ISE) Freiburg on behalf of the IWT.

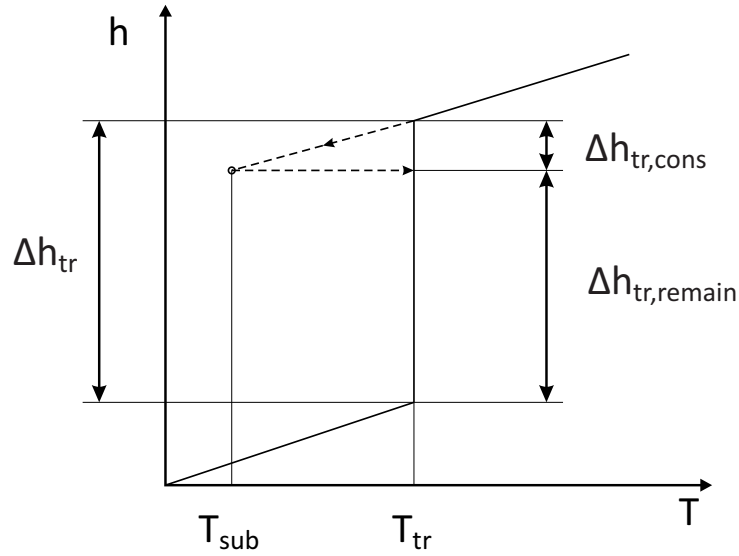
Figure 3.7: h/T measurement of SAT 46 % with DSC

According to the measured data, a summary of basic thermophysical properties of the used SAT can be obtained from table 3.6. As mentioned before in section 2.3.3, the phase change is not a sharp discontinuity in reality and to quantify this effect the melting start and end temperatures are given.

Table 3.6: Phase transition properties of the utilized PCM

specific heat solid	specific heat liquid	heat of fusion	melting start temperature	melting end temperature
c_s	c_l	Δh_{tr}	$\vartheta_{melt,start}$	$\vartheta_{melt,end}$
kJ/(kg K)	kJ/(kg K)	kJ/kg	°C	°C
2.9	3.1	205	52	58

One of the promising advantages stated in the introduction had been the ability of subcooling. It defines a meta-stable state where the PCM is still liquid below the crystallisation temperature if the material is free of nucleus. The main benefit of the subcooled state should stand out if long storage periods are desired. For example, one can imagine a PCM storage module charged up to a sufficient temperature and afterwards left to cool against the ambient (also active cooling can be considered). The PCM will be in thermal equilibrium with its environment after a certain amount of time and still stays liquid. After the material is subcooled a triggering device should activate the phase transition, the temperature rises to the according crystallisation temperature and the remaining heat can be retrieved. In theory the storing process of the subcooled material can be extended infinitely and since the PCM is in thermal equilibrium with the surrounding and it can be triggered with subsequent heat release, the storage process might be considered as "free" of losses. The described process can be displayed in an ideal h/T characteristic and is indicated by the dashed line in figure 3.8.


 Figure 3.8: Subcooling process displayed in an ideal h/T -diagram

The statement of a loss free storage is only accurate to some extend. The reclaimable amount of transition enthalpy ($\Delta h_{tr,remain}$) is highly dependent on the temperature of the the subcooled state. Figure 3.8 illustrates that, if the PCM is liquid at for example 10 °C and triggering occurs the state "jumps" on the vertical line of the phase transition, but the amount above the intersection of the horizontal (dashed) and the vertical line has to be used to heat up the remaining material to the phase change temperature (T_{tr}). Finally it can be stated, that the storage process of the subcooled liquid at ambient temperatures itself, can

be considered as "loss free", but the activation "consumes" a certain amount of transition enthalpy ($\Delta h_{tr,cons}$) according to the PCM temperature.

3.4 Simulation parameters and difficulties

In order to set up the simulation in TRNSYS a selection of general simulation parameter is necessary. These parameters include for instance, the simulation time, the simulation timestep as well as convergence tolerance and the number of iterations. The utilized values can be obtained from table 3.7.

Table 3.7: Utilized simulation parameter

simulation time	simulation timestep	convergence tolerance	number of iterations
τ	$\Delta\tau$	t_{conv}	n_{it}
h	min	-	-
8760	1	0.001	100

The actual simulation time had been chosen to 17 520 h (2 years). In order to provide more realistic starting conditions only the second year had been evaluated, hence 8760 h (1 year) in table 3.7. The small timestep had been necessary to maintain a more stable calculation. The convergence tolerance describes the relative difference of a value between two subsequent iterations. If the value of table 3.7 is met the simulation has converged in this timestep. The iterative process stops if the number of iterations are reached and a warning is written into the simulation log file. If a certain number of warnings is reached the simulation will be aborted.

3.4.1 Numerical stability problems

In the first simulation attempts almost no thermal masses had been utilized which caused convergence problems and no stable simulation had been possible. Utilizing pipes as numerical attenuation helped to fix this problem. But one simplification had to be made. The pipe model (Type709) requires a ambient temperature as input to calculate the thermal losses. Applying a transient temperature such as the ambient temperature from a climate file caused again massive convergence problems and therefore simulation failure. Hence constant boundary condition had to be applied (see section 4). Another problem had been noticed during simulation of the PCM systems. Almost every time if the solar loop pumps are switched on by a controller ($\delta_{SL} = 1$), some kind of overshoot in the energy balance of the solar system and of course in the entire system balance occurs as can be seen in figure 3.9 for the first week of the year.

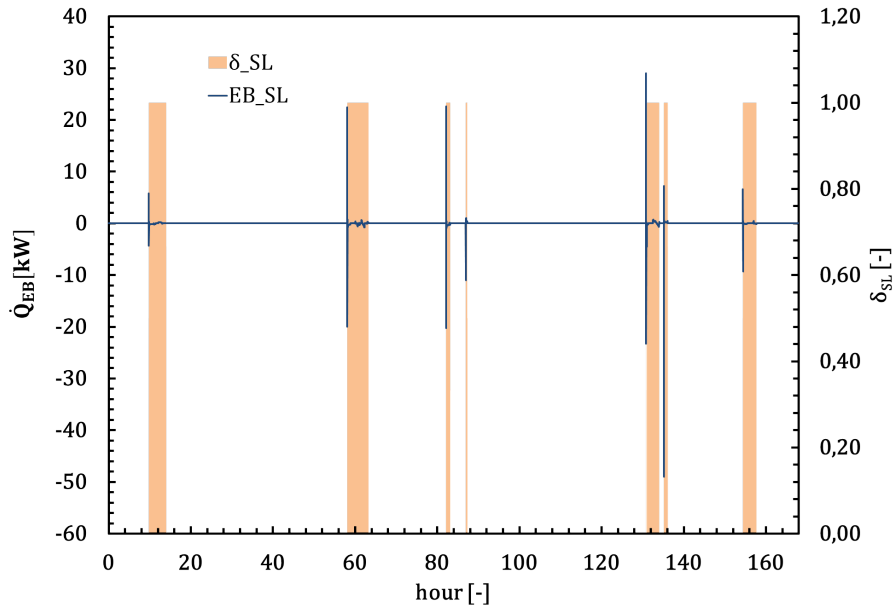


Figure 3.9: Energy balance deviation due to pump activation in PCM systems

The blue curve represents the energy balance and its deviations and the light orange areas indicate when the pump is switched on. The relation between the pump activation and the peaks in the energy balance can be clearly seen in figure 3.10. In the very moment when the pump signal is switched on (light orange area) the overshoot occurs. In the following timesteps the characteristic tunes in which might remind on a damped oscillation.

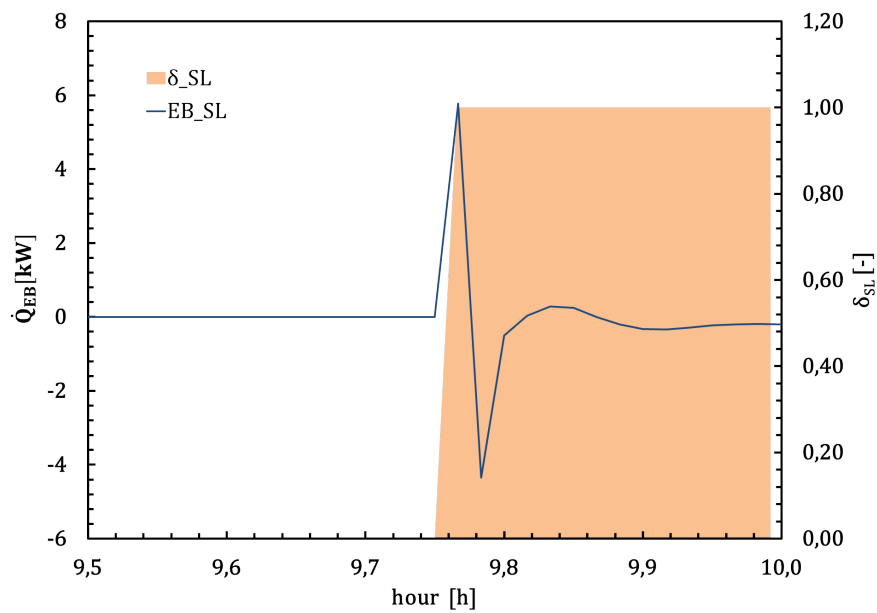


Figure 3.10: Detailed look on the first pump activation of figure 3.9

The evaluations showed that the effect of the deviations has a minor impact in yearly integrated energy balances. Probably, over the period of one year the deviations cancel each other out to a certain extent. Since that these peaks can become quite high and arbitrary concerning the arithmetic sign, it is probably the reason for high deviations in monthly and weekly integrated balances. An explanation can be, that in one period (e.g. month) are more negative (or positive) peaks than positive (or negative) which results in energy balances differing significant from zero (up to $\pm 30\%$ of the highest value in the balance). An interesting aspect however, is that in the reference system simulations these oscillations did not appear. Hence the overall energy balance errors are much smaller compared to the PCM systems (actual values are provided in sections 4 and 5). The reason for this behaviour is not really clear. A speculation might be the interaction between the collector type (Type832v5.00) and the PCM storage type (Type8888). Due to the high collector areas ($\approx 100\text{ m}^2$), high massflows ($\approx 3000\text{ kg/h}$) are required to sufficiently remove heat and avoid high absorber temperatures. If the pump is switched on the high massflow immediately causes a high heat removal from the collector. This energy is subsequently applied to the PCM heat exchanger (reduced by losses due to piping) which is designed as a very thin channel (about 2 to 4 mm). The high mass flow generates only a very small temperature drop over the heat exchanger areas. Now the return temperature from the PCM storage is rather high hence the collector entry temperature is. This causes a higher mean absorber plate temperature which might be responsible for a decreasing heat removal according to equation (2.46) since ΔT_{amb} is linear and quadratic accounted for. On the contrary to the reference system. Here the high storage volume always maintains a rather low entry temperature and therefore a subsequent decrease of the heat removal might not occur. In conclusion the reason for the instabilities of figure 3.9 might be the high massflow in combination with the low temperature drop of the PCM heat exchanger and insufficient thermal mass for numerical attenuation.

3.4.2 Problems in exergy calculations

Another aspect had been the calculation of exergies outside the TRNSYS types. Especially the calculation of the exergy of internal energy on a components and further on, on a systems base can be problematic with larger timesteps. The reason might be that on a types base, internal timesteps, which are smaller than the simulation timestep, are often used in order to maintain stable calculations (e.g. in Type840 and Type8888). The internal energies are calculated during the internal timesteps and summed up. The output of a TRNSYS type, for example some temperature (e.g. mean collector plate temperature) represents the temperature obtained in the last internal time step. If the simulation time step is very large, the difference of the considered temperature output between the end of the previous and the actual timestep can be rather high. For example, equation (2.48) of section 2.3.1 is calculated in the EQUATION statement applying finite differences.

$$\frac{\Delta E_{u,C}}{\Delta \tau} = A_p \cdot C_{eff} \cdot \frac{1}{\Delta \tau} \left[T_{m,p}(\tau) - T_{m,p}(\tau - \Delta \tau) - T_0 \cdot \ln \left(\frac{T_{m,p}(\tau)}{T_{m,p}(\tau - \Delta \tau)} \right) \right] \quad (3.1)$$

As stated before, the fact that the change of internal energy is summed up during the smaller timestep, results in a different value than a rough calculation outside of the type with only the TRNSYS outputs available according to the simulation step and an arithmetic equation. The reason is simply the finer resolution of the internal timesteps, because during one simulation timestep an arithmetic sign change can also occur and therefore influences the final result. This has to be true for the exergy change as well since it is closely connected to the internal energy. But as mentioned before the exergy of the internal energy can only be calculated

with equations like (3.1) in the case of Type832v5.00 (collector) and Type709 (Pipe). For Type362 (radiator) and Type840 (water storage) it had been possible to implement the exergy calculation into the TRNSYS source code (see sections 2.3.2 and 2.3.5). The small simulation timestep should decrease the error in the exergy balance to some extent.

Another problem with exergy considerations occur especially with the radiator and the collector type. As stated in section 2.3.5 inaccuracies are caused by the assumptions made regarding the transition temperature of a heat flux. Recalling the exergy balance of the collector type (equation (2.47)) and taking the assumption that circulation pump is switched off (stagnation), the exergy balance changes to the following expression.

$$\dot{E}_{Q_{sol}} - \dot{E}_{Q_{C,L}} - \frac{dE_{u,C}}{d\tau} = \dot{I}_C \quad (3.2)$$

In this case the internal exergy change has the magnitude of $\dot{E}_{Q_{sol}}$ and an error due to the aforementioned statements. The exergy of the losses increases as well due to higher temperatures in collector stagnation. The assumption of the mean absorber temperature as transition temperature carries an inaccuracy since the exact heat transfer is not modeled in detail within Type832v5.00. The combination of both errors and their higher magnitude in stagnation can result in negative irreversibilities in certain timesteps which violates the second law of thermodynamics. In normal collector operation, the magnitude of those errors have not that impact due to the retrieved exergy by the flow stream, but still an inaccuracy remains. The same problem occurs with the radiator type, although the exergy of internal energy had been implemented into its source code. If the flow stream is switched off, the exergy balance of the radiator simplifies to (see 2.3.5):

$$-\dot{Q}_{rad} \cdot \left(1 - \frac{T_0}{T_{R,ex}}\right) - \frac{dE_{u,R}}{d\tau} = \dot{I}_R \quad (3.3)$$

In equation (3.3), the dimension of the internal exergy and the exergy of the retrieved heat flux are the same. Hence the quite rough assumption of the transition temperature $T_{R,ex}$ has a great impact. Unfortunately, negative irreversibilities can occur if the flow stream is zero. In normal operation mode this error loses its weight, but again an inaccuracy remains. In conclusion, the calculation of internal energies or exergies within the EQUATION statement in TRNSYS utilizing the type outputs might be always problematic for the aforementioned reasons but can be used for an estimation since in normal operation the error decreases. In order to improve the quality of the results an implementation of these calculations into the TRNSYS type is necessary. The same statement can be given for modelling the transition temperature, but the implementation into the Type's source code might not always be possible since different levels of details are utilized.

4 THE REFERENCE SYSTEM

In order to point out weaknesses and strengths of the PCM storage system, a reference solar thermal system had be designed and analysed for comparison. The design is basically taken from the template described in TASK32 (Heimrath and Haller, 2007). Minor adaptations had been made regarding the piping. In this work a pipe model (Type709) had been applied for every single connection except the DHW supply line (see section 4.2). In comparison to the TASK32 template only one pipe for the collector loop and one for the auxiliary loop had been considered. Another difference is the application of an electrical auxiliary heater instead of an auxiliary boiler. A sketch of the utilized reference system is shown in figure 4.1.

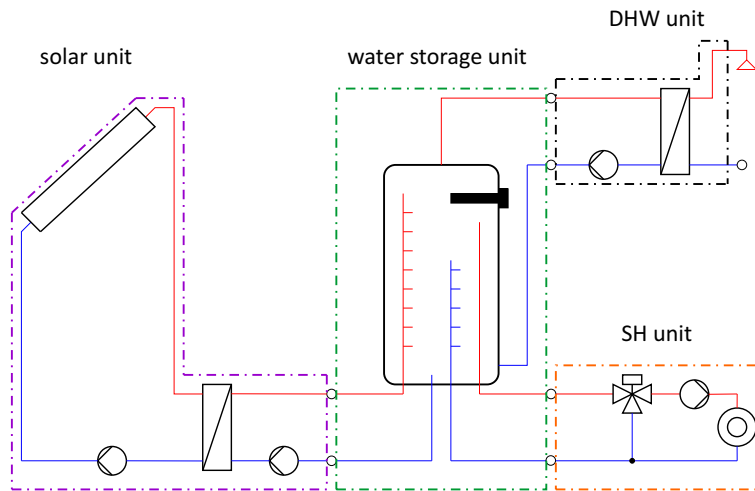


Figure 4.1: Sketch of the considered reference system according to (Bertsch et al., 2013)

The reference system consists of four subsystems according to figure 4.1 as follows:

- Solar unit (purple system boundary)
- Domestic hot water supply (black system boundary)
- Space heating unit (orange system boundary)
- Water storage unit (green system boundary)

As stated in section 2.4.3, an overall solar fraction of $95 \pm 2\%$ is the goal. The dimensioning of the system had been carried out in order to meet this requirement. In the following sections, the subsystems are described in more detail regarding their structure, dimensioning and control strategies. The last section of this chapter should show the results of the energetic and exergetic analysis of the reference system. The following descriptions of the subunits are basically valid for the PCM systems discussed in section 5, deviations are pointed out at the respective place.

4.1 Solar unit

The conversion of solar radiation into useful energy is provided by the collector loop. The requirements of a seasonal application are different to those of a standard solar combi system (solar supported system). Especially in winter, high collector areas are needed in order to provide sufficient energy to keep the required auxiliary heat low. Low ambient temperatures

in winter also state requests to the heat transfer fluid in terms of freezing as mentioned before in section 2.3.4. This fact makes it necessary to decouple the primary collector loop with a antifreeze mixture and the secondary loop with water as HTF. Furthermore high massflows are required in order to keep the HTF temperature under a certain threshold depending on the medium (e.g. $\approx 100^\circ\text{C}$ for water). This results of course in higher electrical pump powers. The basic hydraulic layout and the components to meet those requirements as well as the energy fluxes of the solar unit are displayed in figure 4.2.

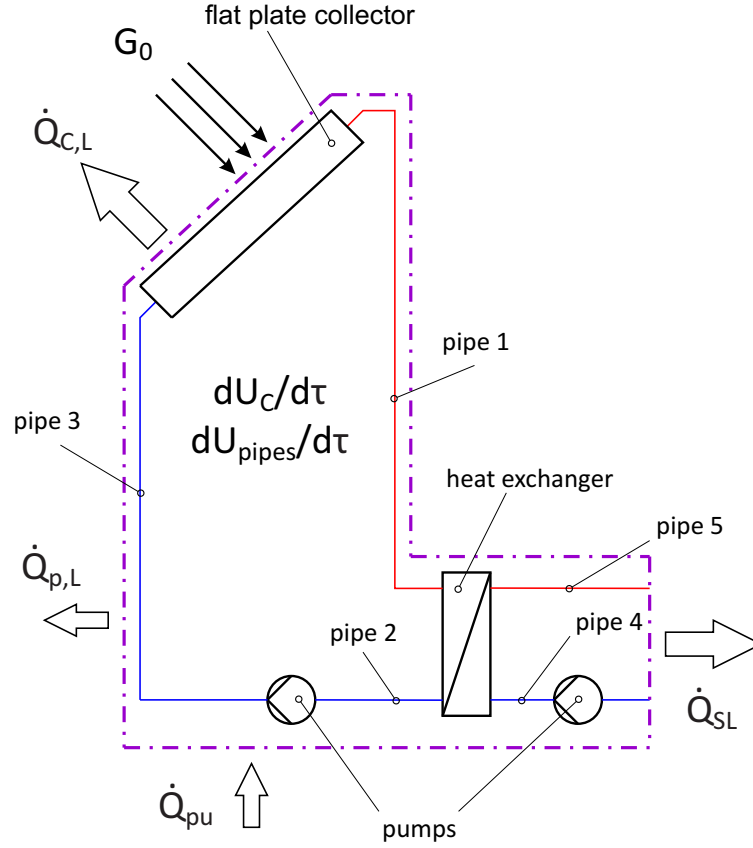


Figure 4.2: Components and energy fluxes of the solar unit

The primary (loop with collector) and the secondary loop (storage side) are decoupled by a counterflow heat exchanger. The HTF is driven by a circulating pump within the respective loops. The collector type had been chosen to a common flat plate collector. As indicated in figure 4.2 every hydraulic connection had been modelled within TRNSYS (label "pipe x"). The utilized heat transfer fluid of the primary side is a not further specified brine in order to avoid freezing. The secondary loop simply uses water. The properties of the heat transfer fluids are displayed in table 4.1.

Table 4.1: Properties of the solar loop HTF (VDI, 2006; Heimrath and Haller, 2007)

spec. heat water	density water	spec. heat brine	density brine
c_w	ρ_w	c_{br}	ρ_{br}
$\text{kJ}/(\text{kg K})$	kg/m^3	$\text{kJ}/(\text{kg K})$	kg/m^3
4.19	998	3.186	1016

The material properties of water are obtained from (VDI, 2006) at $p = 1$ bar and $\vartheta = 20$ °C. The brine properties had been taken from (Heimrath and Haller, 2007). In the simulations the properties remain constant, the pressure and/or temperature dependencies are neglected.

As mentioned before a common flat plate collector with selective coating is utilized for the simulations and modelled with Type832v5.00 (see section 2.3.1). The parameters required to define the collector model can be obtained from standard collector tests. Table 4.2 shows the utilized data.

Table 4.2: Collector parameters obtained from (IZES, 2010)

optical eff.	linear loss coeff.	quadratic loss coeff.	heat capacity	diffuse IAM
η_0	a_1	a_2	c_{eff}	K_D
-	W/(m ² K)	W/(m ² K ²)	J/(m ² K)	-
0.82	2.64	0.0275	8100	0.97

The geometrical data of the considered flat plate collector is given in table 4.3 according to (IZES, 2010) and should give an impression of the dimension but are not discussed in detail.

Table 4.3: Basic geometrical data of the collector obtained from (IZES, 2010)

gross area	aperture area	absorber plate area	height	length	width
A_{gr}	A_{ap}	A_p	H_{Coll}	L_{Coll}	W_{coll}
m ²	m ²	m ²	m	m	m
2.514	2.158	2.158	0.0988	1.829	1.374

In principle it would have been possible to model the collector array with just one instance of Type832v5.00. In order to maintain a certain amount of flexibility for possible changes in the hydraulic layout, five parallel connected collector types had been utilized according to figure 4.3. Each of these instances represent one collector row. It has to be said that these changes did not occur as expected for the following PCM systems but the layout remained the same throughout every simulation. Figure 4.3 should show the implementation of the collector array into a real environment with the building structure as it is considered in this work.

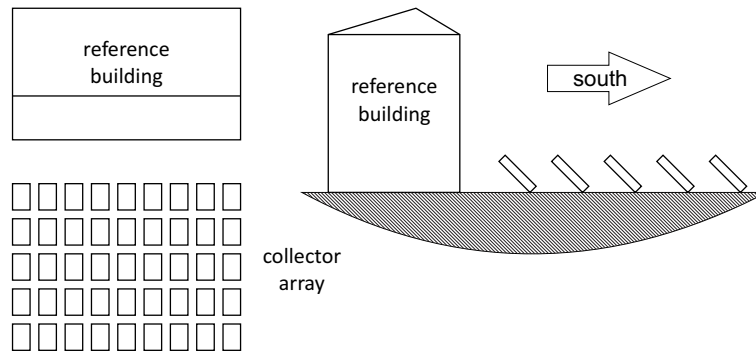


Figure 4.3: Location and layout of the collector array in respect to the building structure

The collectors had been considered as free standing and located on the south side of the reference building in order to avoid shading from the surrounding structures (see figure 4.3).

The angle of the collector planes (β) had been chosen to 45° and the collector azimuth angle had been selected to 0° which represents facing south. The appearance of self shading effects of the collector rows are not accounted for in this work but would of course decrease the useful energy gain. The required collector area had to be determined in order to meet the requested solar fraction and therefore is a result of several simulation runs with parameter variations (e.g. collector area and storage volume). Since the collector area (A_C) is considered as a result of the reference system analysis, it is not given at this point but will be in section 4.5. Also, the specific massflow per collector area ($\dot{m}_{C,spec}$) had been determined during the simulations and is considered as a result as well. The required massflow of the secondary side of the heat exchanger can be calculated once the specific massflow per collector area is found. (Heimrath and Haller, 2007) suggests that the capacitance flow rate (\dot{C}) should be equal on both sides of the heat exchanger. Hence the primary and secondary mass flow can be calculated as follows (Heimrath and Haller, 2007).

$$\dot{m}_{sec} = \dot{m}_{C,spec} \cdot A_C \cdot \frac{c_{br}}{c_w} \quad (4.1)$$

The next components are the pumps used in the solar unit. The consequence of two different heat transfer fluids, are two separate hydraulic loops and hence two circulating pumps are needed. As explained in section 2.3.6 all pumps are modelled with Type3d and considered as variable speed pumps. However in this work, only the states one and zero (pump signal δ_{SL}) and therefore either the maximum flowrate or no mass flow is considered. The pumps of the primary and secondary loop are controlled by a differential controller (Type2b) and share the same signal. For a general more detailed explanation of the controller type it is referred to (SEL, 2012), at this point only a short explanation is given. The pumps are switched on if the collector array outlet temperature (ϑ_{high}) (see figure 4.2) has risen 5 K (ΔT_{high}) above the temperature of a storage node at a relative height (H_{rel}) of 0.05 and is switched off again if the temperature falls to a value only 2 K (ΔT_{low}) higher than the control temperature (ϑ_{low}). The relative height of the storage node is determined as the relation between the actual height of the node location and the actual height of the storage (see section 4.4). The control signal is immediately set to zero if the outlet temperature of the collector field reaches 95°C . The selection of a lower temperature node had provided a more stable control signal since the temperature at the upmost node for example can change more rapidly due to heat removal by the DHW and SH loop. The problem of a possible mixing processes of a higher storage temperature with a lower temperature applied by the solar loop is accounted for by using a stratifying unit within the water storage for the solar loop inlet (see section 4.4). Table 4.4 should sum up the important parameters of the solar loop control strategy.

Table 4.4: Control parameters of the solar loop pumps

higher control temperature	ϑ_{high}	$^\circ\text{C}$	collector array outlet
lower control temperature	ϑ_{low}	$^\circ\text{C}$	storage node at $H_{rel} = 0.05$
higher temp. difference	ΔT_{high}	K	5
lower temp. difference	ΔT_{low}	K	2
monitoring temperature	ϑ_{mon}	$^\circ\text{C}$	collector array outlet
high limit cut-out	ϑ_{cut}	$^\circ\text{C}$	95

Determining the nominal electrical consumption of the pumps is necessary for efficiency considerations of the entire reference system. It is well known that the pump power depends on the pressure loss and the volume flow. Both parameters are varying with the required

collector area. To account for this effects but keep the effort low an empirical approach proposed by (Weiss et al., 2003) had been selected to estimate the nominal pump power. Equation (4.2) shows the empirical expression for the electrical consumption of the sum of the primary and secondary loop based on market inquiries of several sources. The relation is valid for collector field areas of $A_C \geq 75 \text{ m}^2$ (Weiss et al., 2003).

$$P_{el,pu,SL} = 196 \cdot e^{(0.0046 \cdot A_C)} \quad (4.2)$$

It is important to keep in mind that the pump power can not be found in the flow stream's enthalpy (see section 2.3.6), only a fraction is applied as heat due to friction. However the pump power is rather low compared to the incident solar radiation and therefore considered as an effort in the efficiency considerations.

As connection between the primary and secondary loop serves a counterflow heat exchanger modelled with Type5b (see section 2.3.4). The TRNSYS model requires the heat transfer coefficient $((U \cdot A)_{hx})$ of the heat exchanger as an input parameter. Since the heat retrieved from the collector increases linear with the collector area (compare to section 2.3.1) it is necessary to adapt the heat transfer coefficient in an appropriate way. In order to perform parameter studies it would be comfortable to apply a simple relation to determine the heat transfer coefficient depending on the collector area. Therefore an empirical expression could be found in (Heimrath, 2004) as a linear relation between the HTC and the collector area.

$$(U \cdot A)_{hx} = 88.651 \cdot A_C + 328.19 \quad (4.3)$$

An important aspect is, that equation (4.3) results in an heat transfer coefficient with the dimension kW/K.

As stated before, pipes serve as thermal masses in order to maintain stable calculation and heat losses can be considered. Type709 requests different geometrical parameters and fluid properties in order to calculate the heat transfer, the internal energy and the outlet temperature (compare to section 2.3.6). the selection of a pipe dimension is always connected to the pressure loss. The pressure loss depends amongst others on the flow velocity and hence the massflow (actually, to the second power of the velocity). A simple relation had been obtained from (Heimrath and Haller, 2007) since a detailed dimensioning of every pipe in every parameter scenario would have been to complex. Hence the inner diameter of the pipe (d_{iw} in m) can be calculated with equation (4.4).

$$d_{iw} = 0.8 \cdot \frac{\sqrt{\dot{m}_{max}}}{1000} \quad (4.4)$$

Where \dot{m}_{max} denotes the maximum flow rate that appears in the corresponding hydraulic loop. The background of equation (4.4) is the assumption that the flow velocity should be about 0.6 m/s. This expression had been applied for each pipe in the system simulations and is therefore only discussed at this point. The resulting parameters regarding the length of the pipes, material properties and others can be obtained from appendix A. In order to account for the heat losses of the pipes an ambient temperature has to be provided for Type709. The entire collector array is considered as free standing on the south side of the reference building as stated before. Therefore the piping is considered about 3m beneath the surface. The corresponding ground temperature had been modelled with the standard type "Type77" according to section 3.2.

4.2 Domestic hot water supply

The domestic hot water supply loop consists of a heat exchanger (Type805) a circulation pump (Type3d) and the pipe work. The schematic layout and the considered energy fluxes

are displayed in figure 4.4. The pipes are a special case in this loop since the hot water draw offs are very short and the temperature level is rather high (see section 3.1.2) which is resulting in high heat rates.

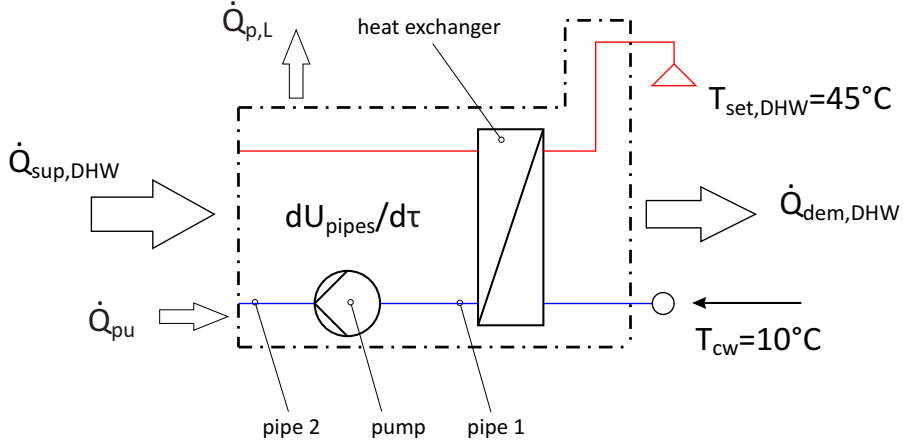


Figure 4.4: Components and energy fluxes of the DHW unit

Due to the thermal mass of pipes in the supply line and the short draw offs, the required temperature level on the demand side is very difficult to achieve. By taking a look back on the penalty functions of section 2.4.3 it becomes clear that the aforementioned effect has a strong influence on the solar fraction and furthermore the dimensioning of the system in terms of collector area, storage volume and auxiliary heater power. Considering that the user usually has to wait for some time until the hot water has the desired temperature in reality and the fact that this behaviour is not modelled by the hot water demand profile and neither by the penalty functions, led to the decision to neglect the piping in the supply line. The heat transfer coefficient $((U \cdot A)_{DHW})$ of the DHW heat exchanger had been calculated to meet an outlet temperature of $\vartheta_{return} = 15^\circ\text{C}$ on the storage side with a supply temperature of $\vartheta_{supply} = 60^\circ\text{C}$, a fresh water temperature of $\vartheta_{cw} = 10^\circ\text{C}$ and a massflow on the storage side of $\dot{m}_{DHW} = 1200 \text{ kg/h}$ according to (Bertsch et al., 2013). This results in a HTC for the DHW loop of $(U \cdot A)_{DHW} = 12766.4 \text{ W/K}$. The pipes are located as described in figure 4.4. In order to consider the heat losses caused by the pipes, their ambient temperature has to be defined. In case of pipe 1, the pipe is considered inside the building which results in an constant ambient temperature of 20°C . Pipe 2 is considered about 3m beneath the surface since the storage is located outside. The ground temperature is again modelled by the Type77. The inner diameter had been calculated according to equation (4.4) with a maximum flow rate of $\dot{m}_{DHW,max} = 1400 \text{ kg/h}$ on the storage side. The utilized pipe lengths and properties can be obtained from appendix A. The dimensioning of the pump power ($P_{DHW,pu}$ in W) had been again taken from (Weiss et al., 2003) who gives an empirical correlation between the pump power and the nominal burner power. The nominal burner power had been considered as the heat load \dot{Q}_D of the reference building according to the applied climate data multiplied with 1.2 as a safety factor. The resulting value shall be denoted as $\dot{Q}_{D,nom}$ with the dimension kW.

$$P_{DHW,pu} = 49.4 \cdot e^{0.0083 \cdot \dot{Q}_{D,nom}} \quad (4.5)$$

With a heat load of the reference building of 3.97kW obtained from (Bertsch et al., 2013), the pump power equals to $P_{DHW,pu} = 51.34 \text{ W}$. The pump control is realised in a way that the pump is switched on if a demand occurs. Since Type805 calculates the inlet massflow on

the storage iteratively by itself, the pump control had to be implemented via an EQUATION statement. According to section 2.3.6 the pump signal can be changed continuously. In order to ensure that the pump transfers the correct massflow ($\dot{m}_{DHW,805}$) to the following Types (in this case Pipe 2), the pump signal (δ_{DHW}) had been calculated as the relation between the maximum flow rate and the current flow rate calculated by Type805 and can be written as follows.

$$\delta_{DHW} = \frac{\dot{m}_{DHW,805}}{\dot{m}_{DHW,max}} \quad (4.6)$$

4.3 Space heating

The space heating loop is modelled as a standard admix circuit. The admix loop is necessary to adjust the inlet temperature of the radiator in a way that it corresponds to the heat demand of the building. The considered components and energy fluxes are shown in figure 4.5.

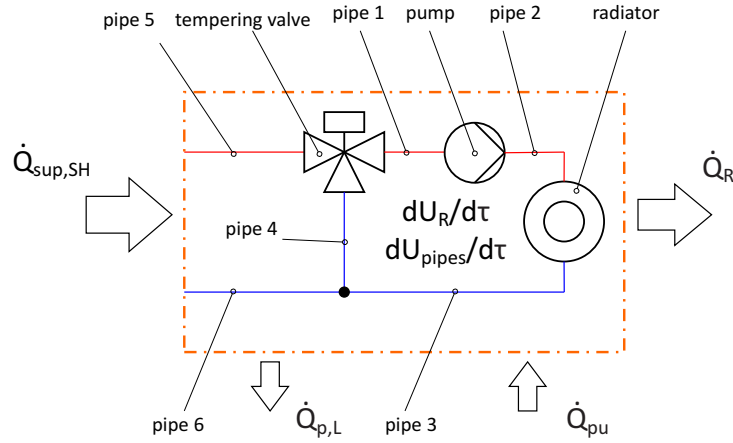


Figure 4.5: Components and energy fluxes of the SH unit

The admix circuit had been modelled with a tempering valve (Type11b, (SEL, 2012)), the already known radiator (see section 2.3.5), a pump (Type3d), a tee piece (Type11h) and the pipes (Type709). The space heating unit had been considered as a low temperature system with the design temperature range, the ambient temperature and the heat load for the location of Zurich and SFH45 given in table 4.5.

Table 4.5: Design parameter of the SH unit obtained from (Bertsch et al., 2013)

supply	return	ambient	heat load
$\vartheta_{D,sup}$	$\vartheta_{D,ret}$	$\vartheta_{D,amb}$	\dot{Q}_D
°C	°C	°C	kW
40	35	-10	3.97

It has to be said that the radiator dimensioning had been carried out before this thesis and was part of the simulation framework described in (Bertsch et al., 2013), a brief description however is given at this point. The massflow control of the radiator is performed by a PID controller (non standard Type320 (Holst, 1996)) which applies the signal to the pump and

the radiator. The control parameter of the PID controller are listed in table A.4 and can be found in appendix A. The control variable for the PID controller is considered as the mean room temperature of the first and second floor ($\vartheta_{room,act}$). The target value of the mean room temperature had been defined to $\vartheta_{room,set} = 21.2^\circ\text{C}$. The actual mass flow in the admix loop had been obtained by multiplying the resulting PID signal (δ_{SH}) with the maximum flow rate of the radiator. The maximum flow rate ($\dot{m}_{R,max}$) had been calculated with equation (4.7) considering the design temperature range and the heat load from table 4.5 (Holst, 1996).

$$\dot{m}_{R,max} = \frac{\dot{Q}_D}{c_f \cdot (\vartheta_{D,sup} - \vartheta_{D,ret})} \quad (4.7)$$

A special aspect has to be considered with Type362 if implemented. A set of nominal conditions is "hard coded" into the radiator model considering the supply and return temperature as well as a nominal temperature difference ($\Delta T_{N,362}$) between the radiator and the room temperature. This would represent a high temperature system with the actual values given in the table below (Holst, 1996).

Table 4.6: Hard coded nominal conditions of Type362 (Holst, 1996)

nominal supply	nominal return	nominal temp. difference
$\vartheta_{N,362,sup}$	$\vartheta_{N,362,ret}$	$\Delta T_{N,362}$
$^\circ\text{C}$	$^\circ\text{C}$	K
90	70	60

Furthermore it is necessary to provide the design radiator power ($\dot{Q}_{D,R}$) according to the actual design conditions as parameter for the TRNSYS type. Here is the point where it becomes necessary to transfer the hard coded nominal conditions (table 4.6) into the actual design conditions from table 4.5. Remembering equation (2.86) from section 2.3.5 this can be done as follows (Heimrath and Haller, 2007).

$$\dot{Q}_{N,R} = \dot{Q}_D \cdot \left(\frac{\Delta T_{N,362}}{\Delta T_D} \right)^n \quad (4.8)$$

The design temperature difference ΔT_D is expressed as the difference between the mean radiator and the room temperature set point (Heimrath and Haller, 2007).

$$\Delta T_D = \frac{\vartheta_{D,sup} + \vartheta_{D,ret}}{2} - \vartheta_{room,set} \quad (4.9)$$

It might be noticed that instead of the logarithmic temperature difference the arithmetic difference had been utilized. The reason had been the low temperature difference between the design inlet and outlet temperature. The radiator exponent (n) had been chosen to 1.3 (compare to section 2.3.5). Finally the resulting design parameter of the radiator can be summed up in table 4.7.

Table 4.7: Design parameter of the radiator

radiator power	max. flow rate	design temp. difference
$\dot{Q}_{N,R}$	$\dot{m}_{R,max}$	ΔT_D
kW	kg/h	K
21.6	682.2	16.3

In order to maintain an appropriate radiator inlet temperature a tempering valve (Type11b) is needed. According to figure 4.5, the tempering valve mixes the return flow stream of the radiator with the supply stream of the thermal storage in a way that a defined inlet temperature ($\vartheta_{in,act}$) is the result. This set point had been approximated according to (Heimrath and Haller, 2007) and had been implemented via an EQUATION statement. The first step had been the calculation of an actual required heat rate ($\dot{Q}_{R,act}$) as a fraction of the design heat load. This relation can be expressed with equation (4.10) (Heimrath and Haller, 2007).

$$\dot{Q}_{R,act} = \max \left(0; \frac{\vartheta_{room,set} - \vartheta_{amb}}{\vartheta_{room,set} - \vartheta_{D,amb}} \cdot \dot{Q}_D \right) \quad (4.10)$$

With ϑ_{amb} as the actual ambient temperature in the time step and the maximum function to maintain a switch off if the ambient exceeds the set point room temperature. Once the required heat is calculated an average radiator temperature ($\vartheta_{R,avg}$) can be estimated considering the radiator characteristic from equation (4.8) and the design temperature difference from equation (4.9), as follows (Heimrath and Haller, 2007).

$$\vartheta_{R,avg} = \vartheta_{room,set} + \left(\frac{\dot{Q}_{R,act}}{\dot{Q}_D} \right)^{\left(\frac{1}{n} \right)} \cdot \Delta T_D \quad (4.11)$$

Finally the actual required inlet temperature can be approximated with the relation given in equation (4.12).

$$\vartheta_{in,act} = \vartheta_{R,avg} + \frac{\dot{Q}_{R,act}}{2 \cdot \dot{m}_{R,max} \cdot c_f} \quad (4.12)$$

The factor of two in the denominator which represents a simplification of the right term might be noticed. It accounts for that only an average required radiator temperature had been considered and not the actual outlet temperature. The resulting inlet temperature is along with the heat source temperature, which is represented by the respective SH outlet of the thermal storage (inlet pipe 5 of figure 4.5), applied as inputs for Type11b. The pump power ($P_{el,pu,SH}$ in W) can be again given as a function of the nominal heat load according to (Weiss et al., 2003).

$$P_{el,pu,SH} = 90.476 + 0.203 \cdot \dot{Q}_{D,nom} \quad (4.13)$$

Where the nominal burner power can be obtained from the previous section. The piping had been again designed according to section 4.1, the geometrical properties are given in appendix A.

4.4 Water based thermal energy storage

The dimensioning of the water storage had been carried out according to (Heimrath, 2004) and (Heimrath and Haller, 2007). A cylindrical shaped water tank modelled with the already discussed Type840 had been utilized. A schematic sketch of the hydraulic layout as well as the energy fluxes for the systems evaluation is displayed in figure 4.6. It can be seen that three double ports are needed for the solar loop, the DHW loop and the SH loop respectively. Furthermore an electrical auxiliary heater had been installed if a lack of solar energy occurs.

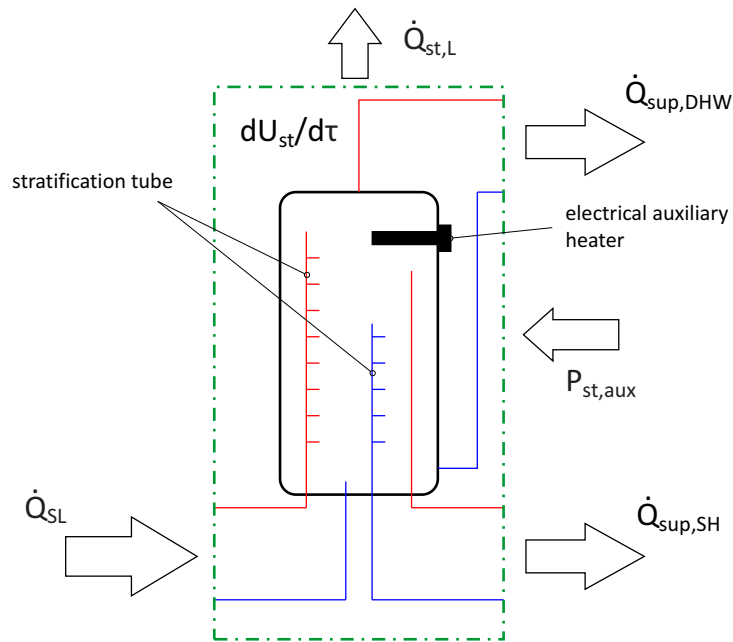


Figure 4.6: Considered water storage unit and energy fluxes

The height of the inlet and outlet ports for the different hydraulic circuits displays an important parameter in storage dimensioning. The heights had to be defined as relative heights as already mentioned. A detailed calculation for the appropriate double port heights had been obtained from (Heimrath and Haller, 2007). These relative heights are depending on the auxiliary heated volume (V_{aux}), the storage volume (V_{st}) as well as the maximum number of storage nodes (N_{max}) applied on the TRNSYS type. The results of this calculation and a descriptions of the utilized double ports of are given in table 4.8.

Table 4.8: Relative heights of double ports calculated according to (Heimrath and Haller, 2007)

description	type	relative height
		H_{rel}
-		
solar unit inlet	stratifier tube	0.992
solar unit inlet	standard	0.05
upper limit aux. volume	-	0.992
lower limit aux. volume	-	0.947
DHW loop inlet	stratifier tube	0.05
DHW loop outlet	standard	0.992
SH loop inlet	stratifier tube	0.15
SH loop outlet	standard	0.982

The basis for these results had been set by a maximum possible number of nodes $N_{max} = 190$ of Type840. According to (Heimrath and Haller, 2007), the auxiliary volume should cover 10 storage nodes independent of the storage volume and therefore the auxiliary volume limits in table 4.8. The stratifying units had been chosen to avoid mixing processes therefore increasing the energetic and exergetic performance. Similar to the previous sections, simple relations for the dimensioning are desired for parameter variations. Hence empirical expressions for the actual height of the storage based on a market research of applied storage systems made by (Heimrath, 2004) and simplified for TASK32, had been utilized. The empirical relations can be given as follows (Heimrath and Haller, 2007).

$$H_{st,1} = 0.32 \cdot V_{st} + 1.65 \quad (4.14)$$

Whereas $H_{st,1}$ denotes a storage height for storage volumes $V_{st} < 14 \text{ m}^3$. For larger storage volumes the following relation is given.

$$H_{st,2} = 0.09302 \cdot V_{st} + 4.698 \quad (4.15)$$

A dynamic selection for the simulations is maintained by the minimum function defined in equation (4.16). This minimum function accounts for the fact that the storage heights are increasing with a different proportion for larger and smaller storages (Heimrath and Haller, 2007).

$$H_{st} = \min(H_{st,1}; H_{st,2}) \quad (4.16)$$

The actual storage height is described with H_{st} and implemented as a parameter into Type840. The required storage volume had been a result of the different simulation runs made to meet the desired solar fraction. Once the geometry is defined the heat transfer coefficient ($U \cdot A_{st}$) can be calculated. The U-value of the store top and bottom ($U_{st,cap}$) had been calculated with the simple equation for a plane wall (compare to section 2.3.3 for example). The U-value of the side walls ($U_{st,sw}$) had been calculated with the relations of heat transfer for cylindrical shape (compare to section 2.3.6 for example). The necessary parameters are given in table 4.9, the steel containment is neglected (Heimrath and Haller, 2007).

Table 4.9: Storage properties according to (Heimrath and Haller, 2007)

convection outside	insulation thickness	therm. conductivity insulation	convection inside	effective therm. conductivity inside
α_{ow}	s_{ins}	λ_{ins}	α_{iw}	λ_{eff}
W/(m ² K)	m	W/(m K)	W/(m ² K)	W/(m K)
10	0.6	0.042	300	2

The overall storage heat transfer coefficient can be calculated with equation (4.17) according to (Heimrath and Haller, 2007).

$$(U \cdot A)_{st} = F_{corr,st} \cdot (U_{st,sw} \cdot A_{sw} + U_{st,cap} \cdot 2 \cdot A_{cap}) \quad (4.17)$$

With A_{sw} and A_{cap} are denoting the inside wall area and the top (or bottom) area respectively. The correction factor $F_{corr,st}$ should account for imperfect insulation and heat bridges. The empirical expression for this factor is again based on a market research of (Heimrath, 2004) and utilized in (Heimrath and Haller, 2007).

$$F_{corr,st} = \max [1.2; -0.01815 \cdot \ln (V_{st}) + 1.6875] \quad (4.18)$$

The location of the storage had been considered outside because of quite large storage heights. Hence the boundary temperature had been set to ambient. The last point in this section is the auxiliary heating control strategy. It had been realised again with a differential controller (Type2b). The important parameters are collected in table 4.10. The small temperature band realised with ΔT_{high} and ΔT_{low} ensures that the temperature of the respective height stays around 55 °C.

Table 4.10: Control parameters of the auxiliary heater

higher control temperature	ϑ_{high}	°C	set point temperature $\vartheta_{aux,set} = 55$ °C
lower control temperature	ϑ_{low}	°C	storage node at $H_{rel} = 0.947$
higher temp. difference	ΔT_{high}	K	2
lower temp. difference	ΔT_{low}	K	1
monitoring temepature	ϑ_{mon}	°C	upmost storage node
high limit cut-out	ϑ_{cut}	°C	95

The resulting storage dimensions are given in the next section.

4.5 Results of the reference system

In order to find a system configuration to meet the given target value for the solar fraction, a parameter variation had been performed. The basic parameters varied, had been the storage volume (V_{st}), the collector array area (A_C) and the installed auxiliary heater power ($P_{st,aux}$). The final parameter results as well as the obtained solar fraction are given in table 4.11.

Table 4.11: Resulting dimensions and solar fraction of the reference system

storage volume	storage height	collector area	spec. collector mass flow	aux. heater power	solar fraction
V_{st}	H_{st}	A_C	$\dot{m}_{C,spec}$	$P_{st,aux}$	f_{sol}
m ³	m	m ²	kg/(m ² h)	kW	%
50	9.349	100	30	2.8	95

With a storage volume of 50 m³ and a collector array area of 100 m², a solar fraction of 95 % can be reached which meets the target value perfectly. The required solar fraction can be achieved in different ways. An alternative had been for example a storage volume of 30 m³ with a collector area of 125 m². The reason for the selection of the higher storage volume had been the fact that this increase in volume had a smaller impact on economic considerations than the increase of the collector area. The increase of storage volume from 30 to 50 m³ requires a diameter increase of about 0.4 m and a height increase of about 2 m which had been considered as the more favorable variant than increasing the collector field area. The rather high specific mass flow had been chosen to keep the temperature on the secondary side of the solar loop below the evaporation temperature of water assumed at atmospheric pressure. As mentioned several times before, the components, subsystems and the overall system had been assessed energetically and exergetically. In the case of the reference system only the obtained system configuration showed in table 4.11 had been analysed since the focus lies on the PCM systems. In the following section this results are presented and discussed.

4.5.1 Quality of results

The first point should be a short discussion of the quality of the presented results. A well known fact is, that every simulation represents a simplified reality. The results obtained from such simulations have to be verified by experiments. However they can provide an estimation of magnitudes, parameter dependencies, trends and can support system design. Since measurements had not been available at the time of this work, a clear verification could not have been made. The plausibility of the gained results under the considered boundary conditions however had been performed by analysing the energy balances of the subsystems and the overall system. Figure 4.7 shows the annual integrated relative (blue) and absolute (red) deviation (ΔEB_j) of the energy balances from zero. The relative deviation had been calculated as the relation between the absolute deviation and the highest heat flux in the considered system (compare to section 3.4.1).

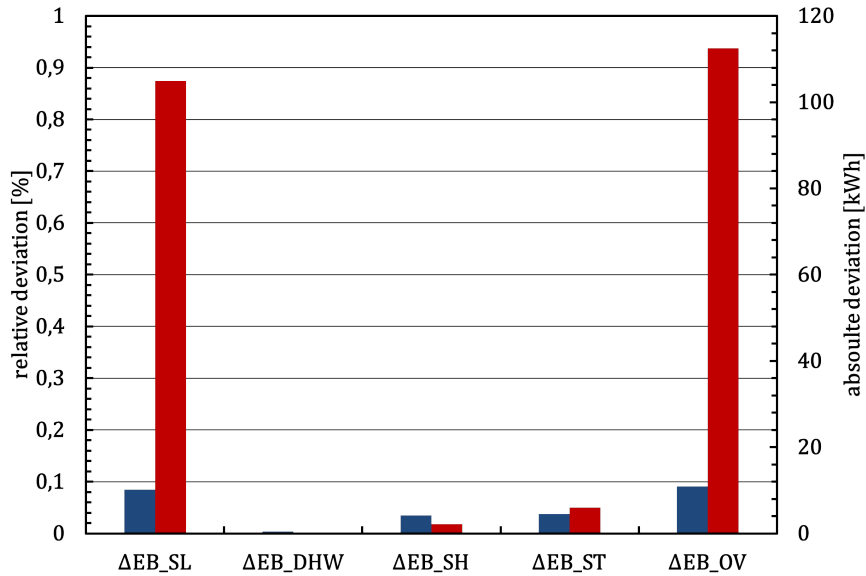


Figure 4.7: Annual integrated absolute and relative deviation of the reference system energy balances

The subscripts "*SL*", "*DHW*", "*SH*", "*ST*" and "*OV*" denote "solar loop", "domestic hot water loop", "space heating loop", "storage" and "overall system" respectively. The maximum deviation in the annual balance of the subsystems occurred within the solar loop with about 104 kWh which represents 0.08 % of the maximum value. The origin of the error is rather difficult to determine. One part might counted in to be round-off errors. Another point might lie within the calculation itself regarding internal time steps, since for example \dot{Q}_{SL} in figure 4.2 can only be calculated with the outlet temperature and the massflow of pipe 5 and the outlet temperature of the respective storage double port (see also section 3.4.2). The lowest deviation is shown by the DHW subunit with about 0.003 % resulting in an absolute value of 0.098 kWh and is almost not recognizable in figure 4.7. The overall system results in an absolute deviation of 112 kWh. Nevertheless the error lies beneath 0.1 % of the maximum in every subunit and the overall system, which had been considered as an acceptable value.

4.5.2 Energy and exergy considerations

In order to analyse the reference system energy and exergy balances had been set up. The resulting annual energy balances had been obtained by integrating the respective values of every time step. The first discussed subsystem should be the solar unit. The integrated annual energy balance for the solar loop is given in figure 4.8 according to the labels and system boundary in figure 4.2.

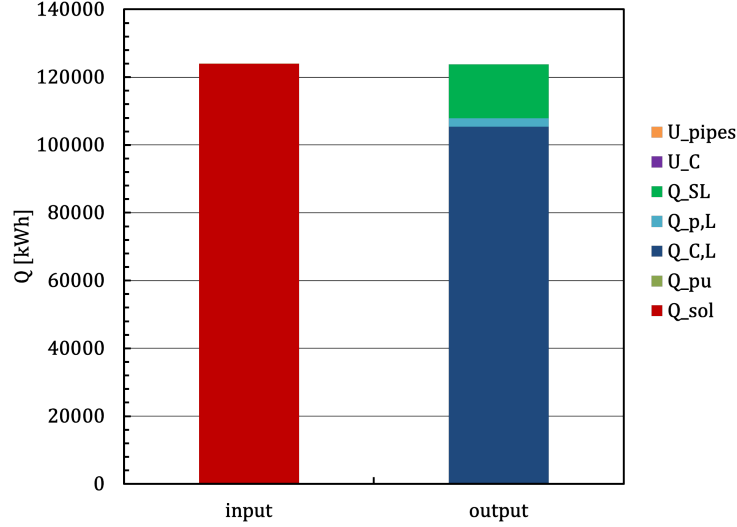


Figure 4.8: Annual energy balance of the solar unit

The ordinate displays the amount of energy Q in kWh. The abscissa divides the energy balance into applied (input) and retrieved (output) energy. The major input of course is the incident solar radiation on the collector plane multiplied with the according collector area. Therefore Q_{sol} stands for the entire available, but not necessarily used solar energy throughout one year. A second energy input is provided by the thermal energy of the circulation pumps (only the thermal energy can be accounted for, see section 2.3.6) which is negligible compared to the magnitude of the solar energy. The value of Q_{pu} equals 13.6 kWh. The actual consumed electrical work of the pumps had been considered in the efficiencies from section 4.5.3. The change in internal energy of pipes (U_{pipes}) and the collector field (U_C) are negligible as well because the initial state (e.g. solar radiation, ambient temperature) is reached again approximately at the end of the climate file. Therefore they are not recognizable in the annual energy balance. The actual values for U_{pipes} and U_C are -0.63 kWh and -10^{-5} kWh respectively. The governing parts on the output side are, the collector field losses (dark blue) $Q_{C,L}$, the pipe losses (light blue) Q_{pipe} and energy supplied to the storage Q_{SL} (dark green). The pipe losses are representing about 2.25% of the entire solar loop losses. The majority of the heat losses are caused by the large collector field area. An important aspect of the collector losses in this calculation, is that they include losses which occur during stagnation times. This and the consideration of the aforementioned solar energy shows a rather pessimistic point of view. Hence figure 4.8 shows to what extent the incoming solar energy per year is harnessed by the applied solar loop (see also next section). A similar aspect appears in the exergetic analysis. An annual exergy balance had been set up according to the energy balance of figure 4.8 since every energy has a corresponding exergy. The resulting exergy balance is displayed in figure 4.9

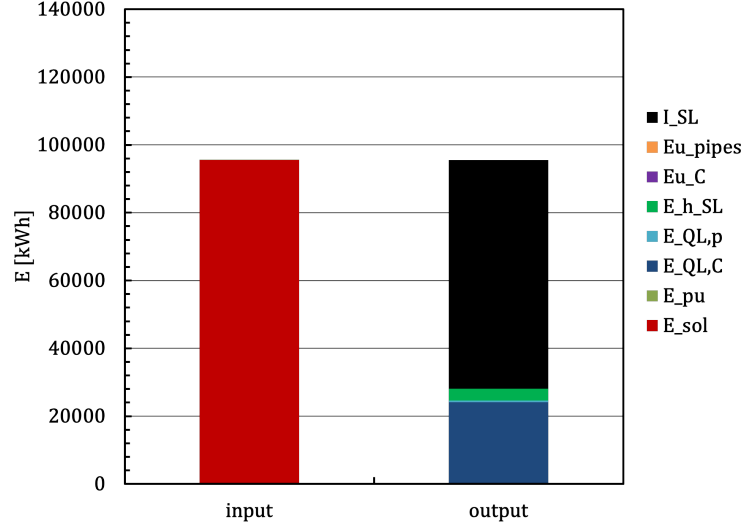


Figure 4.9: Annual exergy balance of the solar unit

The structure of the exergy balance is similar to the energy balance. The ordinate denotes the amount of exergy E in kWh. The exergies are again divided into input and output values. The first thing which stands out compared to the energy balance is the exergy values are of course lower than the energy values. The exergy of the incident solar radiation E_{sol} can again be found on the input side. The exergy of the pump and the internal energies are even lower than the corresponding energies and therefore also not notable in figure 4.9. An interesting aspect is that the exergy of the collector heat losses $E_{QL,C}$ has decreased unproportionally compared to E_{sol} or $E_{h,SL}$. The reason can be found in the model used to assess the solar radiation. If equation (2.29) and (2.49) are reconsidered it can be observed that the relation between the reference state temperature and the temperature of the sun is very small and hence the factor η_G is far more closer to one than the respective carnot factor calculated with the mean plate temperature. That means that high solar exergy and the rather small temperature level (maximum 100 °C) of the storage supply side ($E_{h,SL}$) and the mean absorber temperature is mainly responsible for the high irreversibility I_{SL} of the solar loop. For instance the irreversibility of the utilized heat exchanger only covers 0.15% of I_{SL} . As stated before, figure 4.9 displays to what extent the solar exergy is converted into useful exergy by the applied solar loop.

The same procedure had been used for the DHW loop. The annual energy balance is shown in figure 4.10 and had been set up according to figure 4.4. The thermal energy of the pump is again negligible as well as internal energy of the pipes because of the aforementioned reasons.

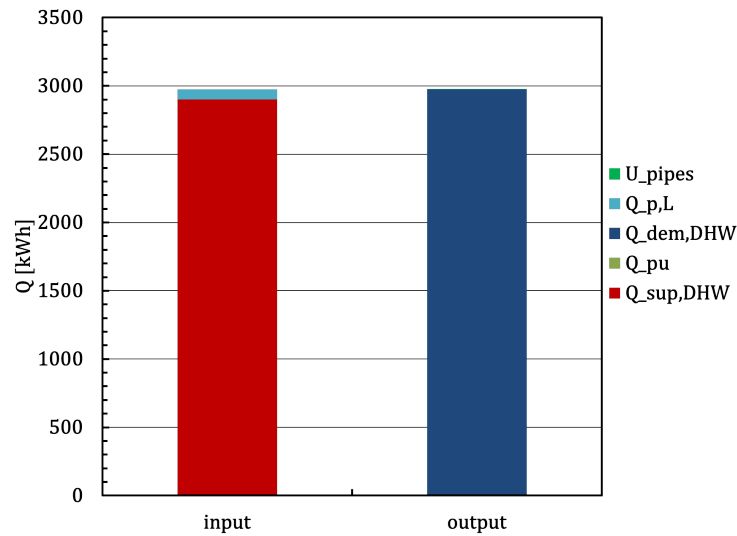


Figure 4.10: Annual energy balance of the domestic hot water supply

The red bar on the left side shows the energy supplied by the storage ($Q_{sup,DHW}$). What might be confusing is the fact that the pipe losses $Q_{p,L}$ are accounted for as input (light blue). The reason can be found in the definition of the boundary temperatures for the pipes according to section 4.2. Pipe 1 had been defined as located inside the building and therefore receives heat from ambient since the heat exchanger outlet temperature on the hot side can fall below 20 °C. Pipe 2 is considered underground hence the heat leaves the system. Since pipe 1 is considered much longer than pipe 2 (see appendix A) the sum of the heat losses is positive. It can be observed that no thermal losses are modelled by the heat exchanger type and the entire heat supplied is transferred to the demand side ($Q_{dem,DHW}$). The exergy considerations show a different picture. The annual exergy balance is therefore displayed in figure 4.11.

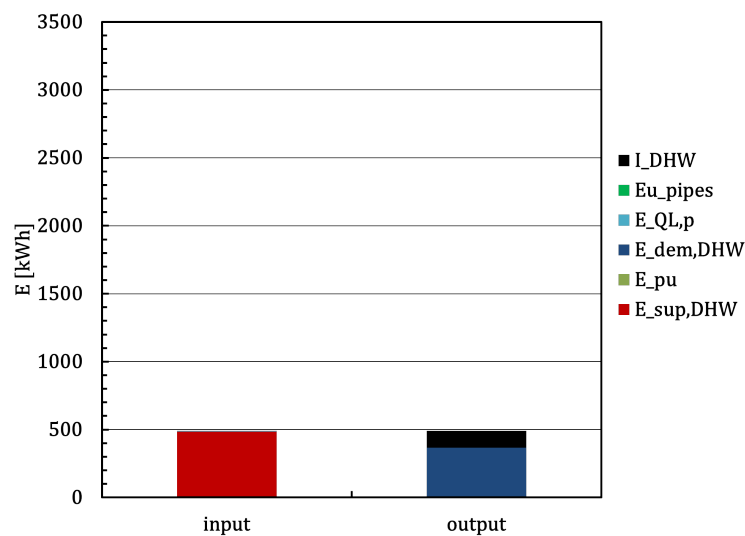


Figure 4.11: Annual exergy balance of the domestic hot water supply

The first interesting point is that the exergy supplied to the DHW loop ($E_{sup,DHW}$) represents only about 17% of the energy. The exergy provided due to pipe losses is almost worthless because of the low temperature level (maximum 20 °C). The same statement can be made for the pump's thermal exergy E_{pu} and the internal exergy of the pipes $E_{u,pipes}$. Hence the dominant part for the irreversibility I_{DHW} can be identified with the heat transfer in the DHW heat exchanger. As stated in section 4.1 every heat transfer carries an intrinsic irreversibility within even if the heat losses of the heat exchanger are not accounted for.

The pipe losses ($Q_{p,L}$) of the space heating unit are more significant compared to the DHW loop which is clear since pipes are utilized in the supply lines as well. The according energy balance can be found in figure 4.12.

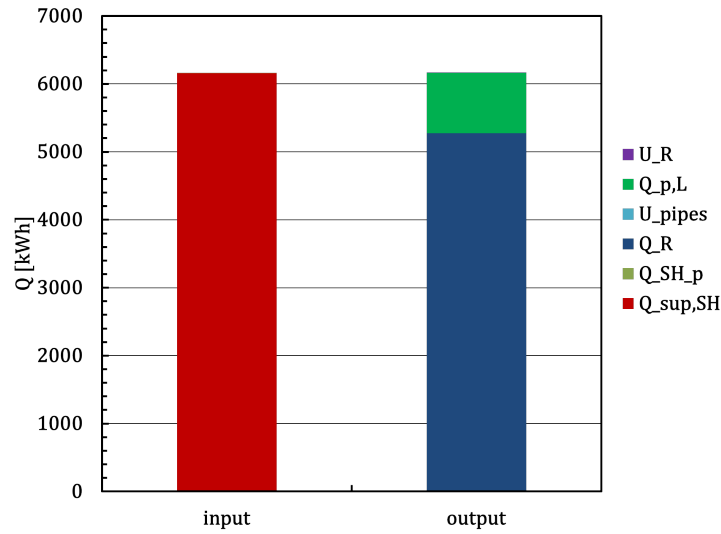


Figure 4.12: Annual energy balance of the space heating unit

The internal energies (U_R and U_{pipes}) and the thermal pump energy (Q_{pu}) are again negligible. The input is represented with $Q_{sup,SH}$ (red) which denotes the supplied energy from the thermal energy storage. A remarkable similarity can be found between the supply exergy of the DHW loop and the SH loop ($E_{sup,SH}$). Both exergies cover about 17% of the corresponding supply energy which indicates a similar average temperature difference between the supply and return lines of both circuits (compare to section 2.2.6). The according exergy balance of the space heating loop is shown in figure 4.13.

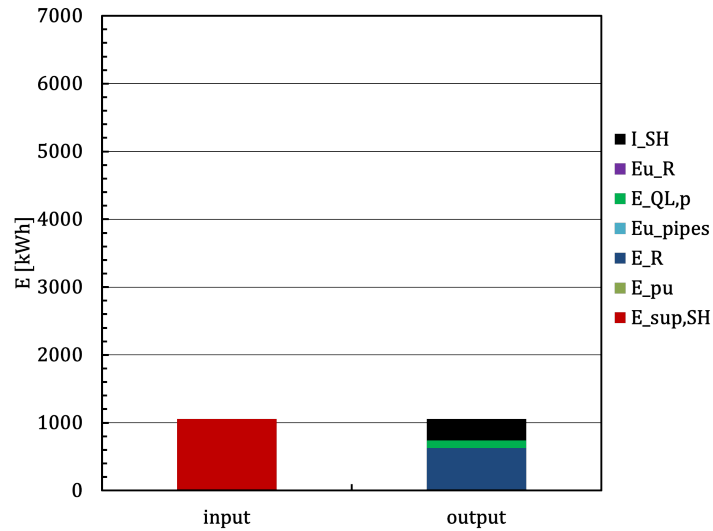


Figure 4.13: Annual exergy balance of the space heating unit

The exergy of pipe losses ($E_{QL,p}$) also becomes more significant because of a higher temperature level in the supply lines. Irreversibilities in the space heating unit appear due to pipe losses, the mixing processes and the heat transfer of the radiator. The mixing processes covers the highest fraction of the irreversibility I_{SH} with about 61 % of the total amount, followed by the radiator with about 21 % and the pipes with 18 %. Mixing processes are always highly irreversible and due to the higher temperature level of the supply inlet (from storage, see figure 4.5) and the rather low level on the return side (from radiator), the high fraction can be explained. The slightly higher irreversibility of the radiator is caused by the fact that the temperature level of the transferred heat (Q_R) is rather low due to a low transition temperature (see section 2.3.5) and a lower amount of pipe losses compared to the transferred heat of the radiator as can be seen in figures 4.12 and 4.13.

The energy and exergy balances for the water storage had been performed according to section 2.3.2 and figure 4.6. The results are shown in figure 4.14. The first thing which stands out is that the change of internal energy over the yearly storage period can be neglected again due to the aforementioned reasons.

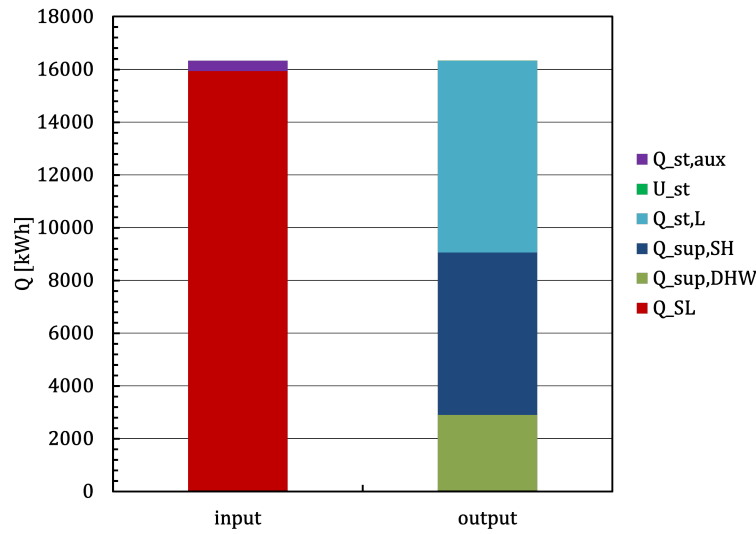


Figure 4.14: Annual energy balance of the water storage

The two inputs on the left side are the supplied heat from the solar unit (Q_{SL}) and the necessary auxiliary heat ($Q_{st,aux}$ with about 403 kWh). Compared to figure 4.8 it can be seen that only 13% of the incoming solar energy can be conveyed to the TES system with the utilized assumptions and control strategies. The rather high loss fraction ($Q_{st,L}$, light blue) can be explained with the outside location of the storage and the ambient temperature as boundary condition. The recovered energy supplied for the DHW and SH together are making up 57% of Q_{SL} . The exergetic considerations are given in figure 4.14. The auxiliary energy had been set identical to the auxiliary exergy since electrical work can be entirely transformed in to heat.

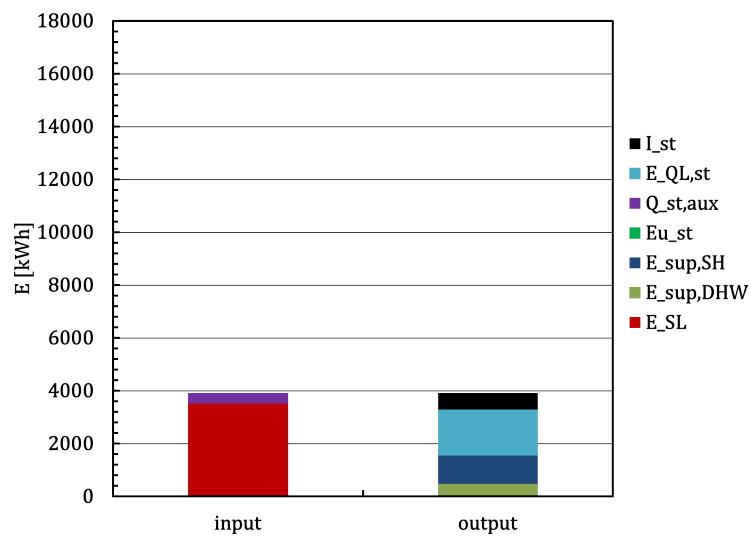


Figure 4.15: Annual exergy balance of the water storage

The input exergy (E_{SL}) represents about 22% of the actual applied energy. Therefore the average temperature level of the solar side is slightly higher than the DHW and SH side (only

17 % as stated before). The exergy leaving the system due to heat losses ($E_{QL,st}$) equals 24 % of its energy which indicates a similar temperature level to the solar side double port. The irreversibility I_{st} is only caused by the heat transfer to the environment and the the exergy destruction due to the conversion of electrical work into heat. Therefore I_{st} can be split into two parts, the auxiliary part which makes up 65 % and the heat transfer which covers 35 %. Hence the additional electrical heating represents the main cause for the irreversibility.

The last point should sum up the results of the subunits. Therefore the overall system energy balance can be seen in figure 4.16. The thermal energy of the utilized pumps ($\Sigma Q_{pu} \approx 18 \text{ kWh}$) as well as the entire change of internal energy ($\Sigma U \approx 0.023 \text{ kWh}$) are not recognizable in the energy balance.

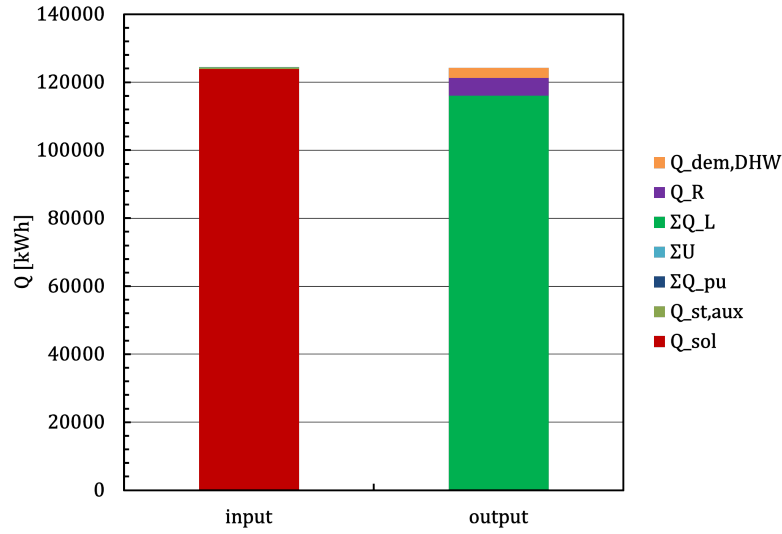


Figure 4.16: Annual energy balance of the overall system

The red bar on the left shows the solar energy (Q_{sol}) as discussed in the solar unit part. It can be seen that only a small part of the available solar energy is utilized with the considered system and solar systems in general. An important point is that stagnation times are included in the loss calculation as already mentioned. That means that if the solar unit pumps are switched off because of, for example excess temperatures in summer, losses due to the stagnated collector are counted in. This fact contributes amongst others to a very low overall efficiency (or better: degree of utilization, see next section). Another aspect is the effect of the control strategy, the more time the pumps are switched on the more solar energy can be utilized. The exergy balance in figure 4.17 shows a very similar behaviour.

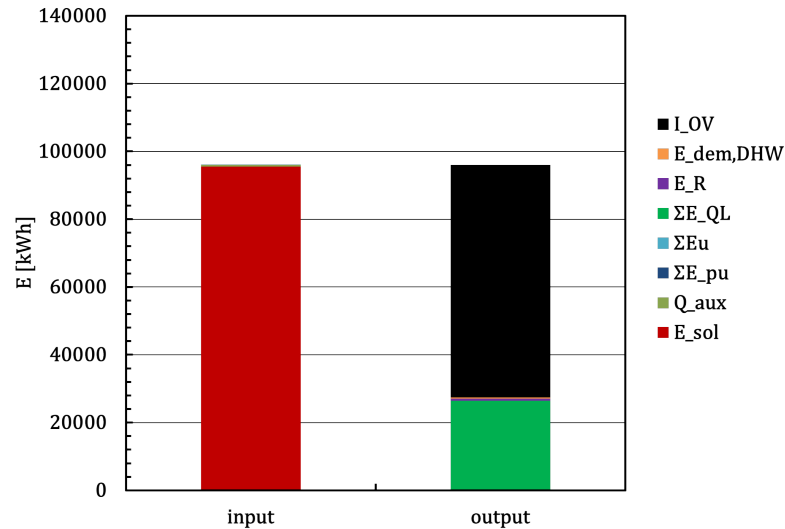


Figure 4.17: Annual exergy balance of the overall system

The useful exergy ($E_{dem,DHW} \approx 627.4 \text{ kWh}$ and $E_R \approx 368 \text{ kWh}$) is almost not recognizable between the high irreversibility I_{OV} and the exergy of heat losses ΣE_{QL} . The total irreversibility is mainly caused by the solar unit as displayed in figure 4.18. The other subsystems are only covering 0.18 % for the DHW, 0.46 % for the SH and 0.9 % for the storage system.

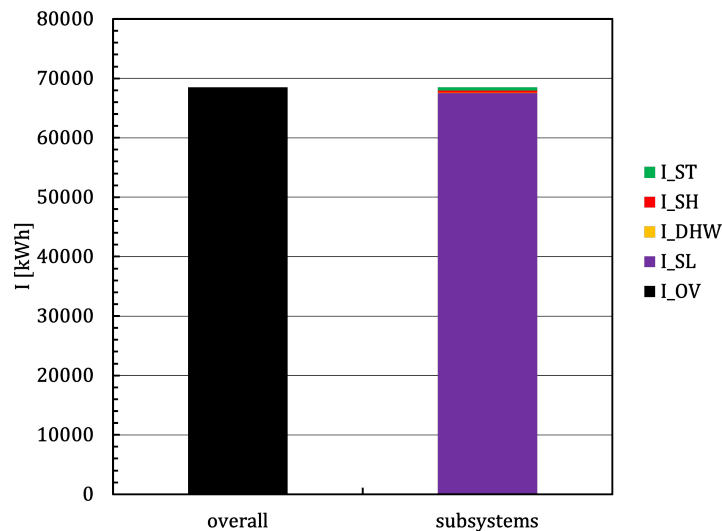


Figure 4.18: Detailed irreversibility distribution of the overall system

The evaluation approach chosen, shows a very pessimistic picture when it comes to solar thermal systems. Of course it can be discussed if the chosen evaluation is suitable to determine the energetic and exergetic performances. Another interesting point is the exergetic assessment of the solar radiation which is already a quite discussed topic (see section 2.2.4). For example (Blanco, 2012) states that the useful energy gain retrieved from the solar collectors should be seen as primary energy in terms of energetic and exergetic assessment.

4.5.3 Performance indicators

The utilized performance indicators had been already introduced in section 2.4 and the resulting solar fraction is given in table 4.11. In this work, the defined penalty functions are influencing the resulting solar fraction (see section 2.4.3). The amount of penalty energy represents to what extent the user requirements are fulfilled. Figure 4.19 shows a good performance in terms of user comfort since the DHW penalties represent only 2.5% of the required auxiliary heat.

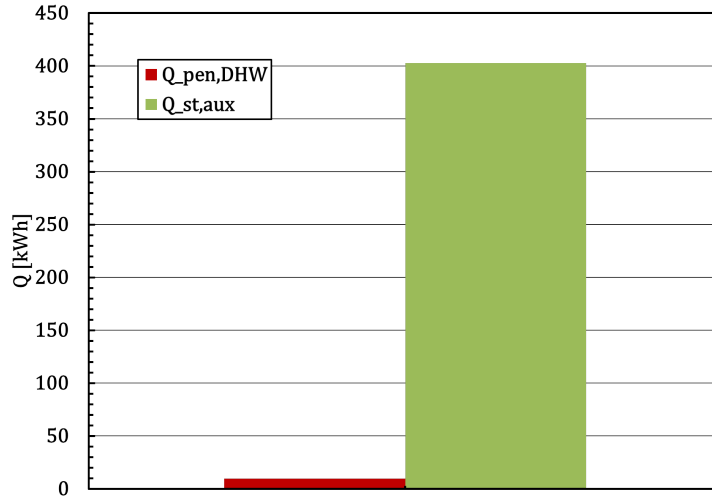


Figure 4.19: Comparison between auxiliary energy and penalties of the reference system

Penalties for the space heating did not occur. The reason can be found in the lower temperature level and a continuous demand compared to a short DHW draw off which requires a temperature above 45 °C. Another point of course is the higher penalty exponent $x_{DHW} = 4$ which represents a very strict position. The efficiency definition used for every subsystem and the overall system except the storage follows equations (2.112) and (2.113) where the effort always contains the applied fluxes (solar energy, electrical pump work etc.) and the gain always considers the retrieved thermal energy to fulfill the required energy demand (DHW demand, SH demand).

The seasonal efficiencies of the subunits and the overall system are given in figure 4.20. The energetic efficiencies are displayed in red, exergetic efficiencies are blue. An important fact is that the displayed efficiencies are calculated with the entire electrical energy consumed by the pumps in contradiction to the energy balances brought in section 4.5.2 where only the thermal part had been considered. The reason for this method, as already stated in section 2.3.6, is that only the thermal part is accounted for in the flow stream enthalpy. In order to estimate the systems performance more realistic and the fact that the fraction of electrical energy consumed by the pumps is rather low, the entire pump energy (W_{pu}) had been considered as an effort according to equations (2.112) and (2.113).

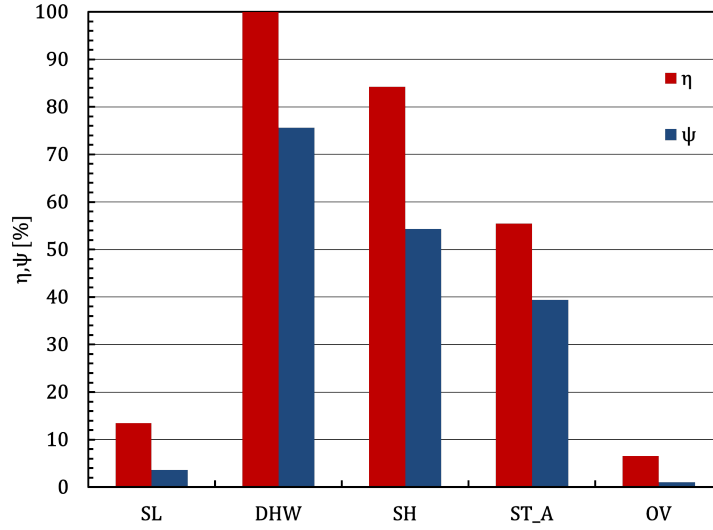


Figure 4.20: Overview of the annual energetic and exergetic efficiencies of the subunits and overall system

The first thing that stands out in figure 4.20 is that the energetic DHW efficiency reaches 100% which of course is impossible in reality. The reason can be found in the fact that no pipes are modelled in the supply line, the heat exchanger type does not account for heat losses and the energy consumption of the pump is negligible compared to the energy supplied from storage. Interesting however is the lower exergetic efficiency of 75.6% which shows perfectly the intrinsic irreversibility caused by heat transfer processes. Figure 4.20 also illustrates quite clear that the limiting factor is the solar loop with an energetic efficiency of only $\eta_{SL} = 13.5\%$ and an exergetic efficiency of $\psi_{SL} = 3.7\%$. The efficiency values are illustrating the problem of utilization and conversion of solar radiation as discussed in the previous section. The space heating loop shows an annual efficiency of $\eta_{SH} = 84.3\%$ which is caused mainly due to pipe losses since the radiator model is considered loss free and the pump energy fraction is again very small. The exergetic efficiency of the SH loop is significant lower than in DHW which has its reasons in the additional mixing processes and the heat transfer of the pipes at a higher temperature level (see section 4.5.2). The overall system finally results in an energetic efficiency of $\eta_{OV} = 6.5\%$ and an exergetic efficiency of only $\psi_{OV} = 1\%$.

A special case provides the storage efficiency. Remembering section 2.4, four efficiency definitions are available for thermal energy storage. In figure 4.20 definition A had been utilized since the change of internal energy is almost zero after a one year period (one entire storage cycle) hence it results in $\eta_{ST,A} = 55.5\%$ for the energetic and $\psi_{ST,A} = 39.5\%$ for the exergetic efficiency. The annual evaluation of the different efficiency cases is given in figure 4.21.

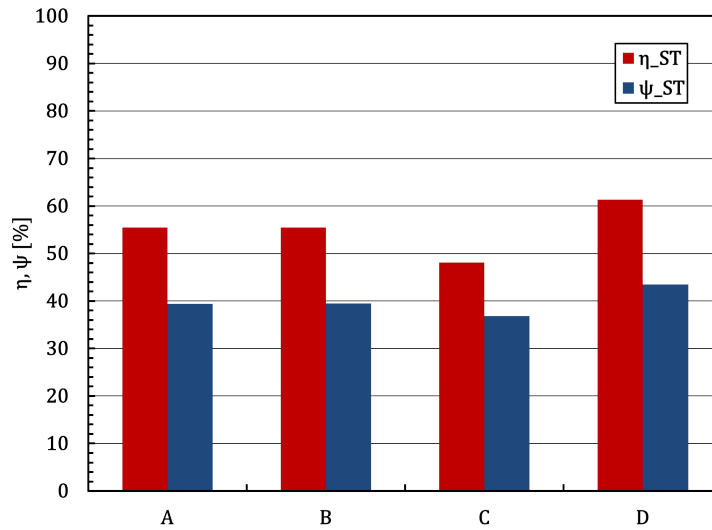


Figure 4.21: Annual evaluated efficiency cases of the storage system

Case A and B are identical if the internal energy change is zero. Case C would have underestimated the storage process since it only considers the initial energy content as an effort. Case D would have over estimated the performance since the final state is accounted for as a benefit and the initial state as an effort. If the internal energy is small or zero no irregular values can occur. This is the case, because one simulated year can be seen as a complete storage cycle where the initial state is reached again. Problems appear in shorter evaluation periods like months or weeks where the initial state can not be reached again. Figure 4.22 shows the monthly calculated energetic efficiencies for the thermal storage.

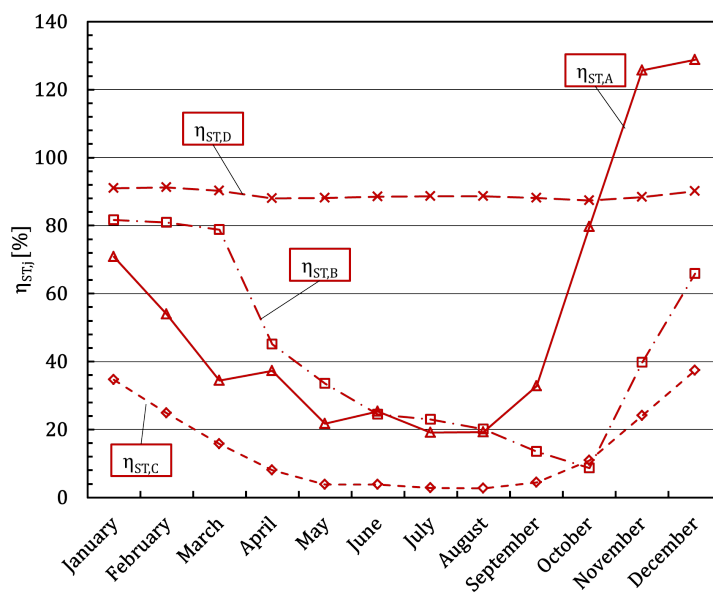


Figure 4.22: Monthly evaluated energetic storage efficiencies according to section 2.4

It can be observed that in November and December energetic efficiencies greater than 100 % are achieved with definition A because the internal energy change is not accounted for (see equation (2.114)). Therefore the use of Case A might be problematic although it can be explained reasonably with its definition. Another point might be case B. Although it brings reasonable values throughout the months one problematic case can occur if the losses exceed the charging energy. In October the fraction of losses becomes the magnitude of the charging energy and resulting in a very low efficiency of 8.6 %. The reason can be found in a low ambient temperature (see figure 3.5 and 3.6) an increasing demand (see figure 4.25) but at the same time a storage energy level which does not require that much charging energy (consequence: decrease of internal energy). This becomes especially a problem for the exergetic efficiency of case B in figure 4.23 which results in an irregular value of -10.8% .

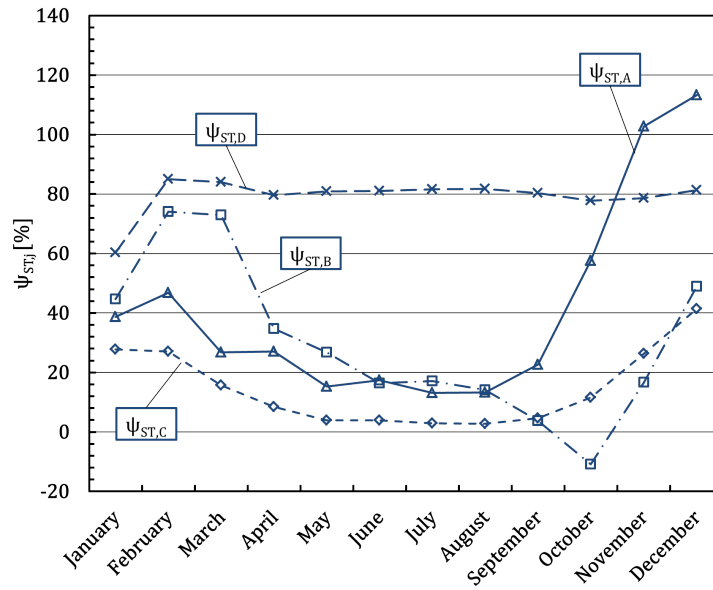


Figure 4.23: Monthly evaluated storage exergetic efficiencies according to section 2.4

Definition C shows a rather low efficiency level and no irregular values occur because of the dominant initial internal energy in the denominator. The problem with case C is however, that the resulting exergetic efficiency is almost identical in its magnitude to the energetic efficiency which can be misleading since it would indicate that no irreversibility occurs. The results of case D show a rather static behaviour in both evaluations. If the definition of case D is reconsidered, it becomes clear that the dominant values in the numerator and denominator are the initial and final internal energy respectively. The high internal energy values are flattening the charge and discharge deviations and therefore case D results in the highest values of about $\eta_{ST,D} = 90\%$ and $\psi_{ST,D} = 80\%$. Another interesting point can be observed if both evaluations are compared. Figures 4.22 and 4.23 show in principle similar efficiency characteristics except in January where an exergetic efficiency drop can be observed throughout every definition. This lower values are a result of assuming the auxiliary heat as pure exergy. Therefore, as discussed in section 4.5.2, the absolute amount of the auxiliary energy remains the same but the fraction compared to the charge and discharge exergy increases which causes lower efficiencies and higher irreversibilities. The analysis of the different storage evaluation cases illustrates very clearly that it is difficult to find appropriate efficiency parameters for a dynamic analysis where the initial state of the storage

can not be reached again. For the periodical analysis only case D remains with reasonable values in every period but might also misleading due to the quite high efficiency level and the aforementioned static behaviour. For full storage cycles ($\Delta U = 0$) the traditional efficiency definition according to equation (2.112) can be utilized without problems.

In order to provide an overview on the monthly performance of the remaining subsystems and overall system efficiencies are given in figures 4.24 and 4.26. Compared to annual efficiencies, monthly values are of course higher in winter months since the degree of utilization of the incident solar radiation is higher. The energetic efficiencies are again almost 100 % according to the before mentioned reasons.

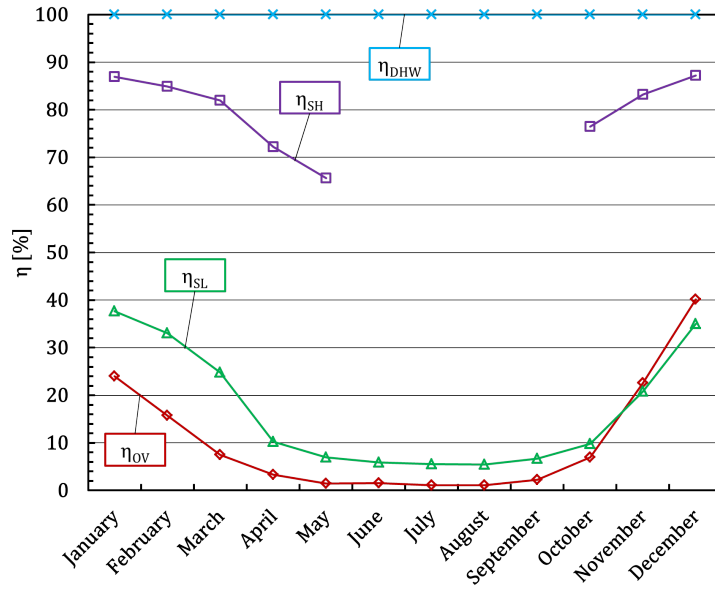


Figure 4.24: Overview of the monthly energetic efficiencies of the subunits and overall system

The solar loop shows a maximum efficiency of $\eta_{SL} = 37.6\%$ in January and a minimum value 5.5% in August as displayed in figure 4.26. The space heating loop shows a maximum value of $\eta_{SH} = 87\%$ in January and a minimum value 65.6% in May because of a decreasing demand. From June to September no space heating demand occurs and therefore the efficiency values are undefined. The critical factor is clearly the low solar loop performance which causes a maximum overall efficiency of $\eta_{OV} = 41.9\%$ in December and a very low level in summer with an average of $\eta_{OV} = 1.5\%$. An important consequence of the utilized efficiency definition can be seen if the overall and solar loop efficiency in November and December are compared. In principle the overall value can not exceed the solar loop value but technically the overall system has the characteristics of a solar thermal storage since the internal energy change is not negligible. The chosen definition for the overall system is identical to case A of section 2.4. This and the energy distribution of the storage system given in figure 4.25 for each month can explain the higher overall values in November and December.

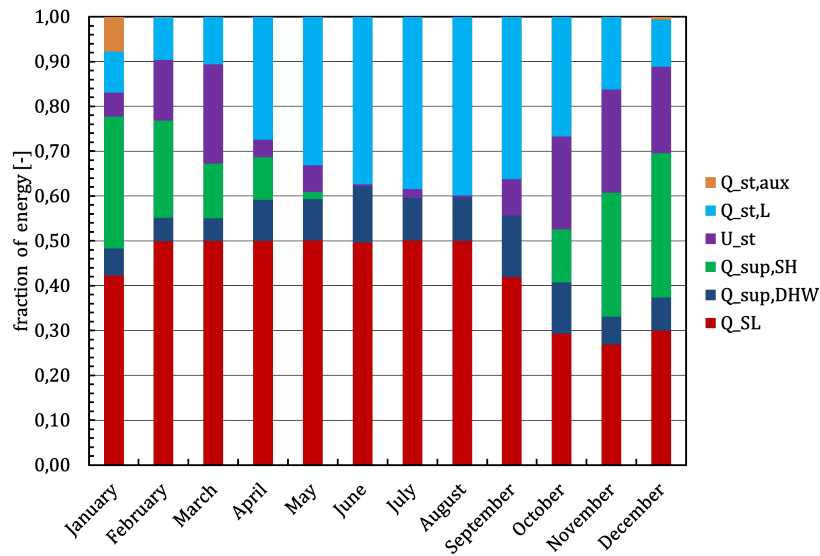


Figure 4.25: Fraction of monthly energy fluxes of the storage system

The abscissa of figure 4.25 describes the fraction of the different entering and leaving energy fluxes and the internal energy change of the storage. Important is that the internal energy change are given as absolute values (purple bars). Now taking a look on the distributions in November and December, it can be seen that the fraction of supplied heat (red bars) is rather low, the demand is increasing (sum of blue and green) and hence the energy has to be retrieved from the storage (purple fraction). Therefore the overall efficiency can exceed the solar loop values according to the utilized definition. The main part of the auxiliary heat (orange bar) is required in January because of a lower internal energy of the storage, the lowest ambient temperature (see section 3.2) and a high energy demand. In December, an almost not recognizable amount of auxiliary heat has to be utilized since the remaining internal energy from charging during summer and the applied solar energy is sufficient to meet the demand. An interesting point is the higher loss fraction during summer (light blue bars). The reason is that due to the decreasing demand and an averagely higher temperature difference between the storage and the ambient in summer than in winter the fraction of losses rises. Similar exergetic efficiency characteristics are given in figure 4.26. Where the DHW efficiency decreases in summer due to a averagely higher temperature difference between the supply side (storage side) and the static temperature level on the load side (see section 4.2). Another obvious point is a generally lower magnitude than the energetic values.

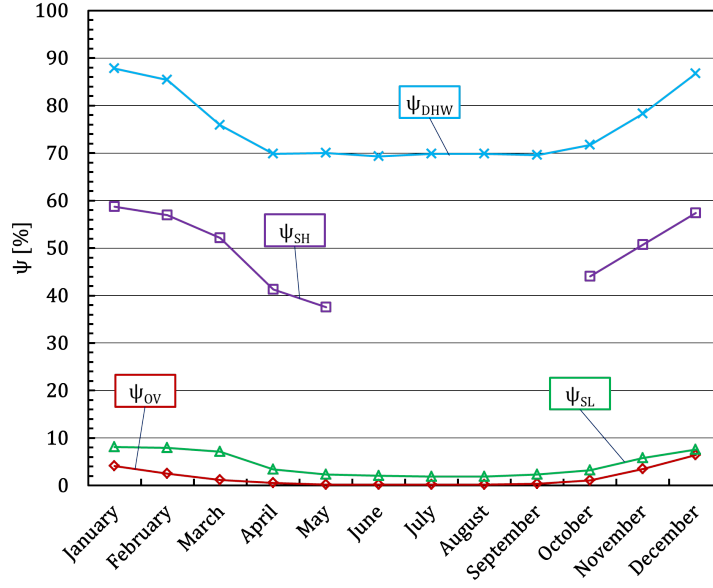


Figure 4.26: Overview of the monthly exergetic efficiencies of the subunits and overall system

The exergetic efficiency of the overall system is very low with a maximum value of only $\psi_{OV} = 6.5\%$ in December and minimum value of only $\psi_{OV} = 0.17\%$ in August. This poor performance, as explained in previous statements, is caused by a very high temperature level of the solar radiation ($T_S \approx 5900\text{ K}$) and the very low temperature level of the system's load side (maximum $45\text{ }^\circ\text{C}$) and again the decreasing exergy demand during summer.

The last point to provide comparability to the following PCM systems is the storage density according to section 2.4.2, however it is only possible to give an estimation on storage densities according to the mathematical models used. In reference to definitions given in section 2.4.2, reasonable temperature limits have to be defined in order to calculate the storable energy Q_{med} . In this work a minimum temperature limit (ϑ_{low}) had been found considering the design inlet temperature of the space heating loop according to table 4.7 with $40\text{ }^\circ\text{C}$. The upper value (ϑ_{up}) had been chosen to $95\text{ }^\circ\text{C}$ considering a safety difference to the boiling point at atmospheric pressure. The storable energy as well as the water mass according to the storage volume given in table 4.11, utilized for the storage density calculations are summed up in table 4.12.

Table 4.12: Parameter for storage density calculation of the reference system

storable energy	water mass	water volume	upper limit	lower limit
Q_w	m_w	V_w	ϑ_{up}	ϑ_{low}
kWh	kg	m^3	$^\circ\text{C}$	$^\circ\text{C}$
3194.29	49900	50	95	40

The next step is the definition of the according storage volumes. For the storage volume (V_{st}) the insulation thickness had been taken into account and a cylindrical storage shape had been assumed. The periphery (V_{per}) in the reference case had been considered only as the stratifying units used for the double port inlets and the auxiliary heater since no pumps

or internal heat exchangers had been modelled. For the calculation of the stratification unit volume, the outer pipe diameters of the subsystem return lines and a pipe length according to the relative storage height of the DHW inlet (see table 4.8) had been utilized. The volume of the auxiliary heater had been assumed as cylinder with a diameter of 0.03 m and a length of 0.5 m. The resulting volumes are given in table 4.13.

Table 4.13: Volume distribution for storage density calculations according to section 2.4.2

volume type	medium	insulation	stratifying units	auxiliary heater	unusable space	sum
	V_{med}	V_{ins}	V_{su}	V_{aux}	V_{un}	Σ
	m ³	m ³	m ³	m ³	m ³	m ³
V_{st}	50	63.4	-	-	-	113.4
V_{per}	-	-	0.025	0.00035	-	0.025
V_{eff}	-	-	-	-	-	113.42
V_{act}	-	-	-	-	0	113.42
$V_{act,alt}$	-	-	-	-	222.38	335.80

It stands out that the volume for a probable unusable space (V_{un}) had been set to zero for one case. The reason had been the assumption that the storage is free standing and not integrated in the building structure or kept in some kind of housing. Another assumption had been made that in case of maintenance no additional space is required to execute the required work. On the other hand it is necessary to keep a certain space always available even if it is outside. Therefore a second case had been defined with an assumed additional unusable volume of table 4.13 with a quadratic cross section reduced by the storage area. The length of the quadrat had been assumed in a way that the distance between the storage and the four lateral edges on each side is one meter which results in an area of $A_{un,alt} = 33.75 \text{ m}^2$. The unusable height had been chosen to the storage height with insulation $H_{st,ins} = 9.949 \text{ m}$. Finally the resulting storage densities are given in 4.27 for the three considered categories and the two cases.

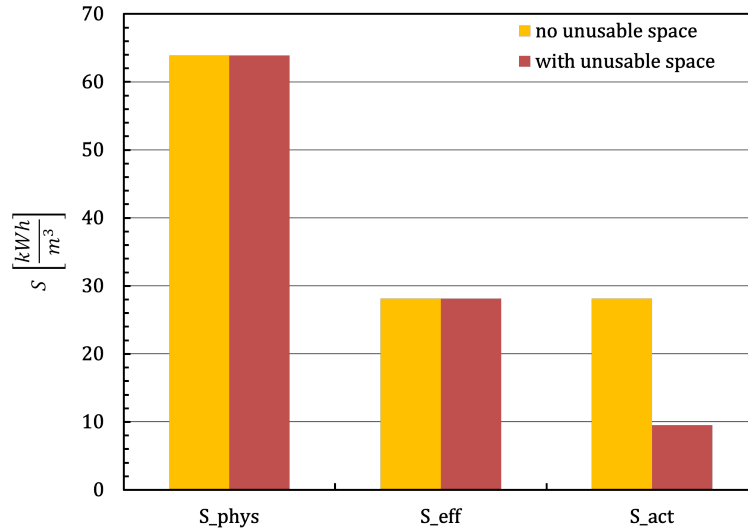


Figure 4.27: Estimated storage density of the water based TES in the reference system

The physical storage density states of course the highest value with $S_{\text{phys}} = 63.88 \text{ kWh/m}^3$. The actual and the effective storage density share a value of 28.16 kWh/m^3 in the first case (orange bars). The second case shows of course a drastic decrease in the actual storage density by considering the described unusable space (red bars). The main cause for the lower storage density in this assumption can be found in the high insulation thickness installed and the unusable space if considered. In addition to the considerations given, the storage can be located beneath the surface which would reduce the unusable volume to zero and the storage effect of the surrounding soil might even be taken into account.

5 PCM SYSTEMS

In order to find an appropriate layout integration of the PCM storage, three different system configuration had been investigated. The PCM storage systems had been integrated according to figure 5.1 by practically replacing the water based storage (green system boundary). The remaining subsystem basically stayed the same as described in section 4, changes are described in the respective sections. Therefore system changes had mainly been performed within the green system boundary.

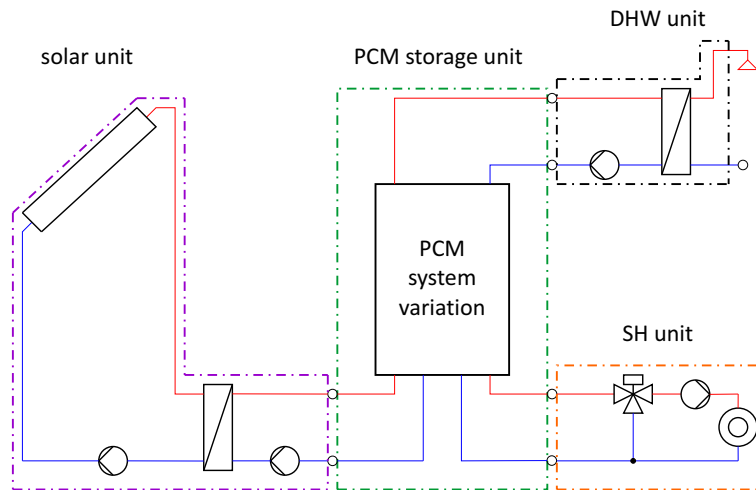


Figure 5.1: Layout of the overall PCM system

A short description of the three considered PCM storage variations are listed in the following enumeration:

- Version A: Direct integration of the PCM storage for space heating and domestic hot water supply (simply replacing the water storage with PCM system).
- Version B: The PCM storage system charges an auxiliary water storage for space heating and DHW preparation.
- Version C: Bypassing the PCM storage with a part of the solar loop supply into an auxiliary water storage to cover the demand in summer.

The following sections should give a description of the utilized PCM storage and the aforementioned system variants. In section 5.1 the actual utilized PCM storage is described in terms of structure, basic function and parameters used for the simulations. Sections 5.2, 5.3 and 5.4 are describing the different PCM integrations as well as their control strategies and results.

5.1 The PCM storage

The mathematical model and the basic structure of the PCM storage had already been discussed in section 2.3.3. This section should cover the more practical information. The box shaped modules are insulated and combined on a storage rack as schematically displayed for example in figure 5.3 of section 5.2. In this work the modules are hydraulically connected in a way that one module cannot be charged and discharged simultaneously but it is possible to charge one module and discharge another at the same time. The PCM storage provides one double port for the source side (solar side) and for the load side (SH and DHW, or

auxiliary storage). The heat exchanger on the top and bottom of the storage modules are in parallel connection, the entering flow stream is distributed equally between both heat exchangers for charging as well as discharging. On the left side of figure 5.2, a sketch of the utilized modules and its dimensions is displayed.

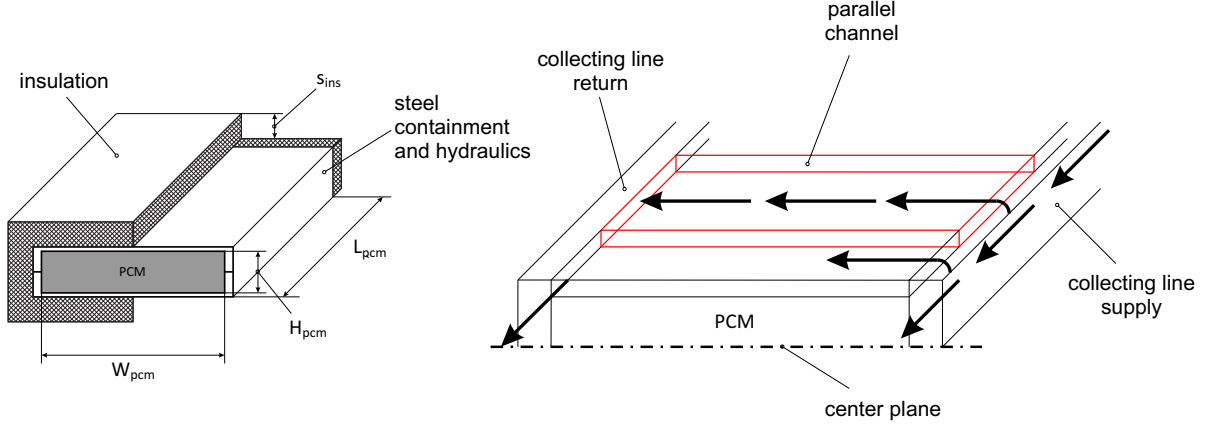


Figure 5.2: Structure and dimensions of a PCM module (left) and detail of a top heat exchanger section (right)

The channels of the heat exchangers are supplied by a collecting line and flow through parallelly into the return collecting line as can be seen on the right side of figure 5.2 for the top heat exchanger. A selection of the necessary storage parameters and module dimensions used for the simulations are given in table 5.1.

Table 5.1: PCM module parameter and dimensions

PCM height	PCM width	PCM length	channel height	insulation thickness	wall thickness	conductivity insulation	conductivity steel
H_{pcm}	W_{pcm}	L_{pcm}	s_{hx}	s_{ins}	s_w	λ_{ins}	λ_{st}
m	m	m	m	m	m	W/(m K)	W/(m K)
0.05	1.5	2.5	0.002	0.1	0.002	0.042	50

The dimensions given in the table above are approximately the same as a real PCM module which had been tested at the IWT at the same time as this thesis was written. Interesting might be the very small channel height of only 2 mm (see also (Furbo et al., 2012)) to increase the temperature lift across the heat exchanger area and improve the heat transfer. Hence also a small PCM layer thickness of 5 cm is utilized which is necessary because of the low thermal conductivity of the PCM. In total, a number of 24 modules had been used in the simulations which results in the following storage parameters of table 5.2.

Table 5.2: PCM storage parameter

number of modules	total PCM volume	total PCM mass
n_{mod}	V_{pcm}	m_{pcm}
-	m ³	kg
24	4.5	5760

It might stand out that the total PCM volume is only a tenth of the reference water storage which has its reasons in a higher energy density and the phase change enthalpy, but not entirely. Earlier calculations performed by project partners of the Technical University of Denmark (DTU) showed that a PCM volume of about 6 m^3 might be sufficient to cover the heat demand of a low energy house (Furbo et al., 2012). This assumption resulted in a total number of 24 modules with the module dimensions of an earlier prototype generation (Furbo et al., 2012). In order to maintain a compact storage system the considered number of storage modules remained 24 for the current module prototype which resulted in a lower PCM volume given in table 5.2. In fact the number has not been changed throughout the calculations, the reasons will be discussed in the results sections. The last important point is the selection strategy of an appropriate module. A selection algorithm is implemented into the additional controller Type8889 (see section 2.3.3). The controller decides upon different parameters which module should be selected in charging and discharging cases. A detailed description of the algorithm should not be given in this work but some important aspects shall be mentioned. The first one considers the subcooling ability of the considered phase change material. The mathematical model has to determine somehow when the subcooled state is possible or not since in reality the system is very sensible to any appearing nucleus. Experiments performed at the IWT during the COMTES project showed that it is essential to avoid any nuclei otherwise the material would "activate" itself after a short period of time or wouldn't even reach the subcooled state. One possibility to improve the subcooling behaviour is to hold the temperature way above the melting temperature for a certain period of time to ensure total melting throughout the entire module. This threshold temperature had been chosen to $\vartheta_{thr} = 75^\circ\text{C}$ and the time period to $\Delta\tau_{thr} = 1\text{ h}$. The second aspect is the possibility to define a sequence of charging and discharging cases and their priority which are applied for the module selection. Important for this work should only be that in summer charging and in winter discharging is prior. The last point is that the mathematical model provides the possibility to define a minimum usable temperature level of one PCM module ($T_{heat,min}$). If this level is fallen below the control algorithm switches to another module which is above the defined limit or triggers a subcooled one. This limit temperature is also used to calculate a usable energy $Q_{supply,pcm}$ which represents the energy content of a PCM module above the defined threshold. The last aspect is especially interesting to define control strategies for the storage load side in sections 5.3 and 5.4. Finally the PCM storage is considered to be located outdoors in every system variation which defines the ambient temperature as boundary condition.

5.2 Version A: Direct integration

The first logical step in order to integrate a PCM storage into the considered solar thermal system is to simply replace the water storage. Therefore some minor changes in the hydraulic layout had to be performed in the simulation setup. Type8888 provides a double port for the source side therefore no changes had to be made for the solar unit. On the load side the resulting massflow had to be distributed to the DHW and the SH loop according to their request. Hence an additional controllable flow diverter (Type11f, (SEL, 2012)) for the supply line and a tee piece (Type11h) for the return line had to be integrated. Figure 5.3 shows the layout and corresponding heat fluxes of the PCM storage system which can be imagined replacing the black box within the green system boundary in figure 5.1. The PCM modules are combined on a rack and form the final PCM storage as indicated in the figure below.

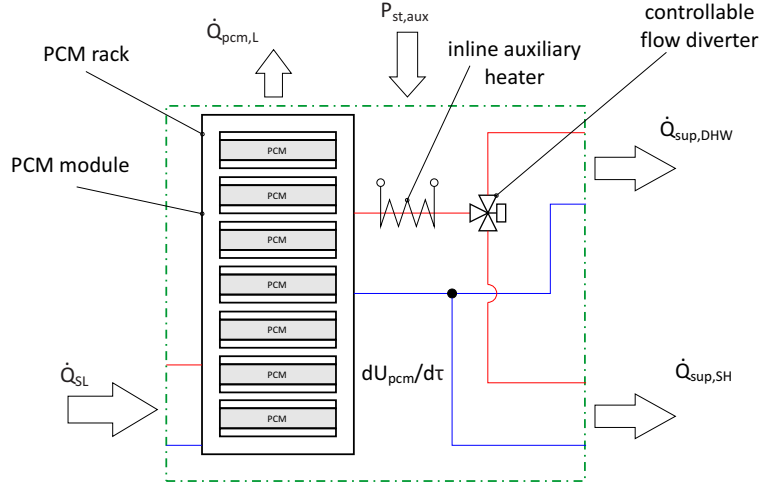


Figure 5.3: Schematic layout of the directly integrated PCM storage

Furthermore the auxiliary heater of the water storage had to be replaced by an inline electrical heater (Type6) with a set point temperature of $\vartheta_{set,aux,A} = 55^\circ\text{C}$ and a maximum heat rate of $P_{aux,A} = 10\text{ kW}$. The auxiliary heater operates all year long and is always switched on if the set point temperature is fallen below. The high heat rate should have ensured that penalty functions are mainly avoided which had been not the case as discussed later on. The control of the flow diverter had to be applied manually. The control function (δ_A) had been calculated within an EQUATION statement according to the mathematical model of Type11f which can be found in (SEL, 2012). The signal is then given by equation (5.1).

$$\delta_A = \frac{\dot{m}_{SH}}{\dot{m}_{SH} + \dot{m}_{DHW}} \quad (5.1)$$

Where \dot{m}_{SH} and \dot{m}_{DHW} denoting the massflow required by the SH and the DHW loop respectively. Every other control strategy or parameter had been left the same according to the reference system of section 4 except the solar loop control had to be adapted. The solar loop pump control had been again modelled with a differential controller according to section 4.1. The control parameters used, can be obtained from table 5.3.

Table 5.3: Control parameters of solar loop pumps in Version A

higher control temperature	ϑ_{high}	$^\circ\text{C}$	collector array outlet
lower control temperature	ϑ_{low}	$^\circ\text{C}$	mean temperature of chosen module
higher temp. difference	ΔT_{high}	K	10
lower temp. difference	ΔT_{low}	K	5
monitoring temperature	ϑ_{mon}	$^\circ\text{C}$	collector array outlet
high limit cut-out	ϑ_{cut}	$^\circ\text{C}$	95

The first difference to the reference system is ϑ_{low} because a water storage temperature is not available anymore. Therefore the mean PCM temperature of a module selected by the internal control algorithm is available instead (see previous section). The control signal is determined analogous to section 4.1. A major difference to the reference system can be found in higher values of ΔT_{high} and ΔT_{low} . The reason lies within the problem that in almost every charging case the flow stream cooled down the module in about the second half of the charging period. In other words in some cases the PCM temperature exceeded the supply temperature

of the solar loop. The fact that there is a timeshift between ϑ_{high} and ϑ_{low} because of the PCM's thermal mass and that ϑ_{low} is defined as a mean PCM node temperature which implies the possibility that a boundary node might have a higher temperature, causes the control system not to shut off. Hence higher temperature thresholds had been set to avoid this behaviour accepting that this method results in a rougher control function. The direct integration caused by far the most stability problems during the simulation. Hence a higher number of iterations had been defined to 1500 which resulted in about 680 not converged timesteps (108 h) over two years. Also the interaction between the controlled flow diverter and the short DHW draws caused numerical stability problems similar to section 3.4.1.

5.2.1 Results of Version A

The direct integration of the PCM storage caused major problems in terms of user comfort since the penalties had been massive throughout the simulations. Therefore no further evaluations considering energetic or exergetic assessment had been made but the problems and the origin of the resulting penalties should be discussed in this section. The considered system had the parameters given in table 5.4.

Table 5.4: System parameters of Version A

pcm volume	collector area	spec. collector mass flow	aux. heater mass flow	solar fraction
V_{pcm}	A_C	$\dot{m}_{C,spec}$	$P_{st,aux}$	f_{sol}
m ³	m ²	kg/(m ² h)	kW	%
4.5	100	30	10	-

Basically the reference system configuration had been taken with 24 PCM modules instead of the water tank. The high power of the inline auxiliary heater had been chosen to avoid those high penalties which apparently did not work out as illustrated in figure 5.4.

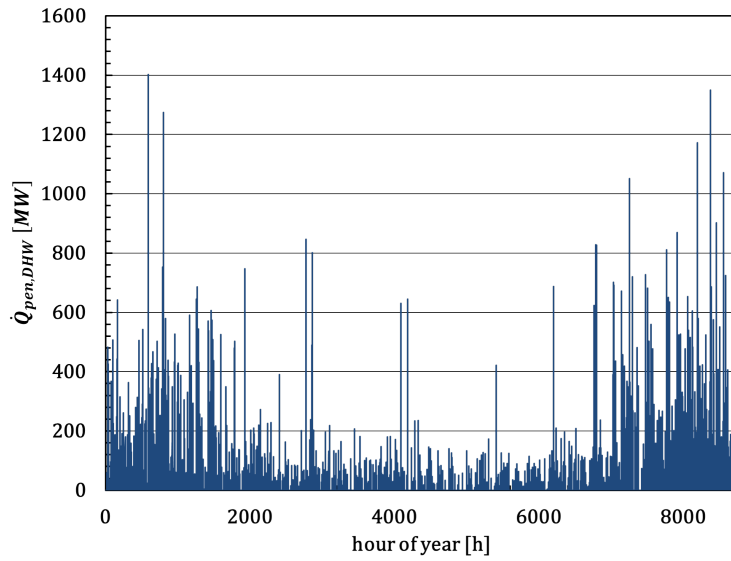


Figure 5.4: DHW penalties of Version A during the year

Almost every DHW draw off resulted in penalty energies. In certain timesteps penalties in a Megawatt magnitude occurred, especially in the winter months where the space heating demand has to be covered additionally. Interesting is again that no SH penalties appeared throughout the year which can be explained with lower heat rates and a lower temperature level. In order to explain the difficulties regarding the domestic hot water preparation a best case scenario should be considered. Therefore a draw off in July is discussed in detail. During this draw off, no space heating demand has to be covered and the mean PCM temperature is about 70 °C. Figure 5.5 shows temperature and mass flow characteristics during the draw off.

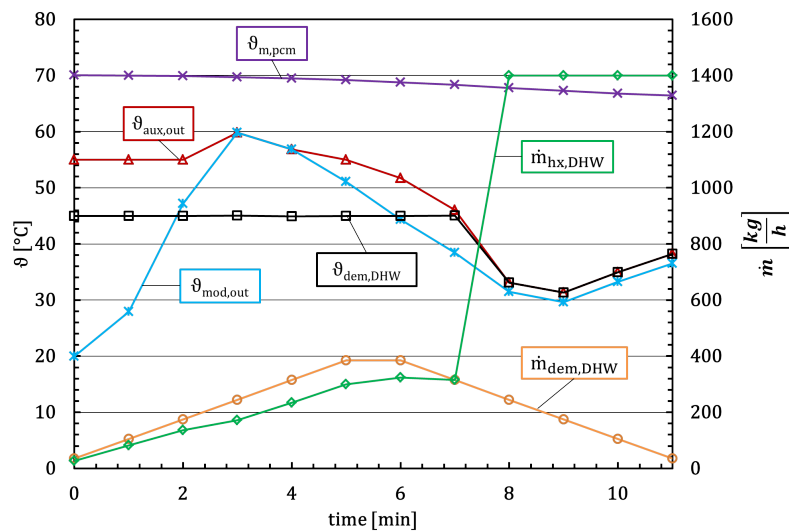


Figure 5.5: Relevant temperature and mass flow characteristics during a DHW draw off in July

The left ordinate shows the temperature and the right ordinate the mass flow. The abscissa denotes the time during the draw off in minutes. The purple curve displays the mean PCM temperature. The light blue line denotes the module outlet and the red line the auxiliary heater outlet temperatures. The black characteristic stands for the DHW heat exchanger outlet on the demand side (see section 4.2). The orange massflow represents the hot water demand according to section 3.1.2. Finally, the green characteristic shows the source side massflow of the DHW heat exchanger calculated within Type805 and representing the massflow through the PCM module. Due to the high PCM temperatures the heat rate is sufficient to meet the DHW setpoint of 45 °C in the first 6 minutes (black line). The section where $\vartheta_{mod,out}$ is identical to the auxiliary outlet temperature indicates that during this time no heater power is required. After the third minute the module outlet temperature starts decreasing and the auxiliary heat rate is insufficient to hold the outlet temperature at 55 °C at the peak of the draw off. The mean PCM temperature decreases steadily as well causing the decrease of the module outlet temperature. At minute seven, $\vartheta_{aux,out}$ drops down to about 45 °C which forces the Type805 control to increase the massflow in order to provide the required heat rate. But with the already low level of the PCM outlet temperature and a not sufficient auxiliary heat rate it is not possible to provide the DHW demand temperature. The characteristic of the estimated module heat transfer coefficient $(U \cdot A)_{mod}$ illustrates that it is necessary to increase the heat transfer coefficient of the PCM module in order to avoid these difficulties.

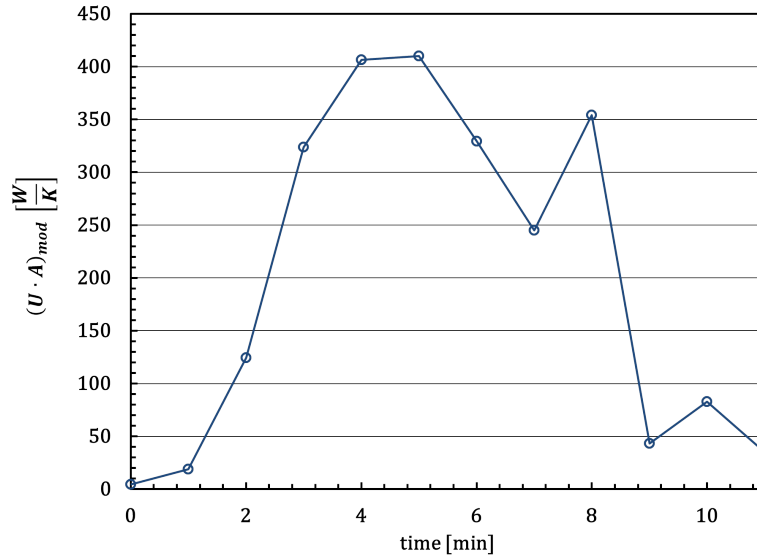


Figure 5.6: Estimated heat transfer coefficient of the PCM module

The HTC rises due to the increasing massflow and reaches a critical point around 5 minutes. The following drop might be caused by the decrease of the mean PCM temperature. It indicates that the temperature of the boundary nodes is lower and therefore the heat flux decreases. The subsequent raise can be explained with the increasing massflow of the DHW heat exchanger but has no effect because of the already low temperature level of the module outlet. The maximum value of about 430 W/K has to be maintained throughout the entire draw off to avoid penalties. As stated above the considered case represents a module at high temperature level. If a subcooled module after crystallization is considered, the hot water

preparation might be even more problematic. Increasing the auxiliary heat rate may reduce the penalties but can cause again poor solar fractions due to a shift in the numerator of the utilized solar fraction definition to the auxiliary side.

5.3 Version B: Auxiliary water storage

Considering the results of Version A it had been necessary to decouple the PCM storage from the load side. Therefore an auxiliary water storage with an electrical heater identical to the reference system had to be integrated between the PCM storage and the demand side according to figure 5.7. An additional pump had to be installed to circulate the HTF between the two storages. The PCM system charges the subsequent water storage which provides the heat source for DHW and SH. The solar unit charges therefore the PCM storage. Figure 5.7 shows the according hydraulic layout and also the considered heat fluxes.

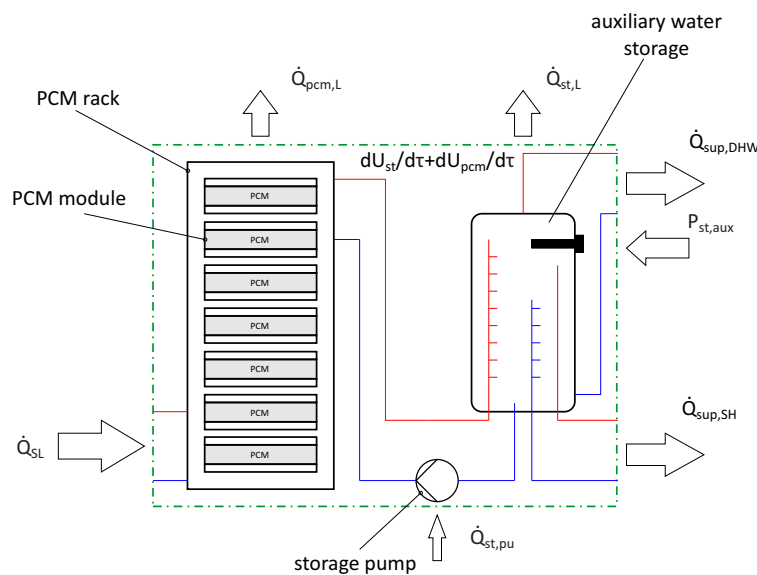


Figure 5.7: Schematic layout of the PCM storage with an auxiliary water storage

The new storage system replaces again the black box in figure 5.1. The other subunits could have been left the same and had been dimensioned identical to section 4. The only difference to the reference system can be found again in the solar loop control which had to be adapted according to section 5.2. The auxiliary storage dimensioning according to section 4.4 had been implemented into TRNSYS via an EQUATION statement to automatize the storage adaption during parameter variations. The parameter of the water storage of table 4.9 had been also left unaltered except the insulation thickness had been reduced to 0.06 m. The reduction of the insulation thickness followed the decision that the auxiliary storage is located inside the building with room temperature as boundary condition. The PCM storage had been left outside of the building to maintain the comparability to the reference system. An indoor installation for refurbishments and new built structures is, due to the modular and compact structure of the PCM systems possible of course and should be carried out in further investigations. The control strategy for the storage pump states a very important influence on systems performance. Considering a phase change material for a control strategy can be a bit more complex than for a single phase material. The additional factor is the state of the PCM which has to be considered. During the development of Type8888 the idea came up to define a control value which describes the usable energy content of one module or the entire PCM storage (see also section 5.2) to simplify the necessary control strategy. Therefore the

already mentioned threshold temperature $T_{heat,min}$ is used. The pump control had again been implemented with a differential controller but instead of a temperature threshold the aforementioned energy had been considered. Table 5.5 provides the according parameters.

Table 5.5: Control parameters of the storage pump in Version B

higher control value	Q_{high}	kJ	$Q_{supply,pcm}$ output of Type8888
lower control value	Q_{low}	kJ	0
higher energy difference	ΔQ_{high}	kJ	10000
lower energy difference	ΔQ_{low}	kJ	500
monitoring energy	Q_{mon}	kJ	-
high limit cut-out	Q_{cut}	kJ	-

Hence the control signal is 1 if the usable energy content of the PCM storage has risen above 10 000 kJ and 0 again if it falls below 500 kJ. The rather distant threshold values had been chosen to avoid too strong oscillations of the control signal. Not only the energy content is important but also the temperature level of the available energy to avoid mixing processes in the auxiliary storage. As stated in the previous section $Q_{supply,pcm}$ is calculated with $T_{heat,min}$ as lower limit. Fortunately Type8888 allows the definition of $T_{heat,min}$ as a dynamic input value. This input value had been connected with a storage temperature at a relative height of $H_{rel} = 0.05$. The consequence of this method is that the usable energy content is dependent on the specified storage temperature which ensures that only energy with an appropriate temperature level is provided for the auxiliary storage at any time. Furthermore a stratification unit avoids any mixing processes. The resulting control function had then been multiplied with a schedule given in figure 5.8 which ensures that in the first simulation year no PCM discharge occurs. In other words, PCM storage is charged in advance to the actual evaluated simulation year.

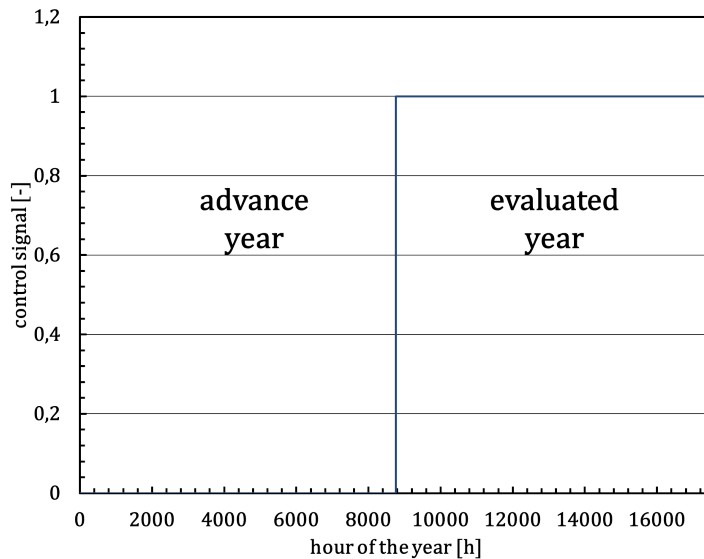


Figure 5.8: Storage pump schedule over two simulation years

The pump power had been set as a constant value to $P_{st,pu} = 55$ W since the pump energy

impact in every subsystem had been almost negligible according to section 4.5. The auxiliary heater control function had been set identical to section 4.4 as well. The heater power had to be increased to $P_{aux} = 4 \text{ kW}$ to keep penalty functions low.

5.3.1 Results of Version B

Similar evaluations as for the reference system had been performed to assess the PCM systems. In order to find the most optimum system parameters, a parameter variation had been carried out. The collector area remained constant with 100 m^2 during the variation since it had been sufficient to reach the requested solar fraction in the reference system and therefore considered as an upper limit. The number of PCM modules also remained constant since during operation the PCM storage control only needs three different modules as can be observed in the hourly mean temperature characteristics given in figure 5.9.

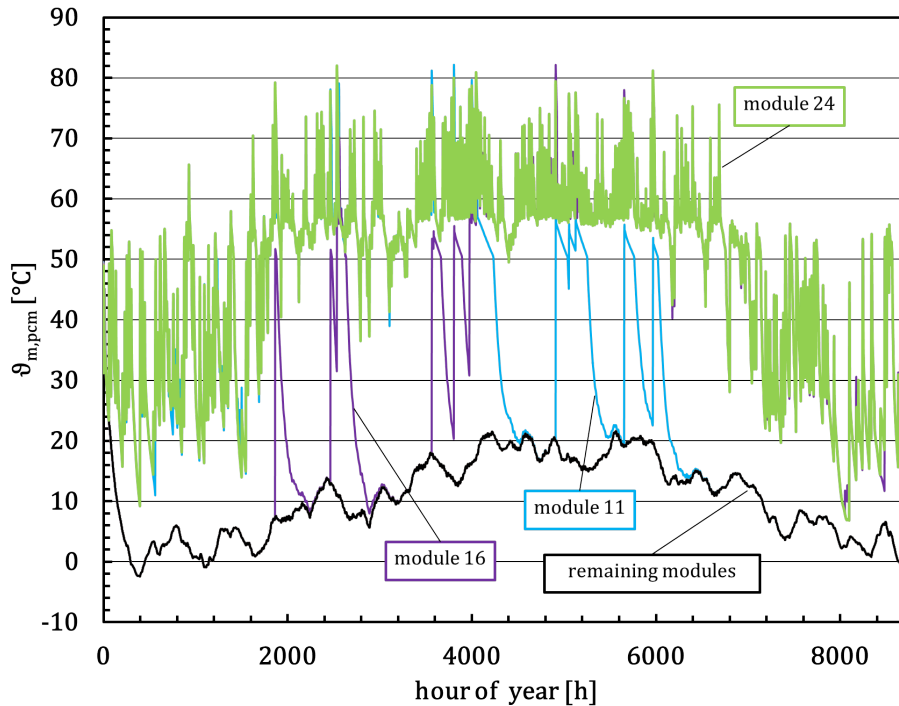


Figure 5.9: Hourly mean temperature characteristics of PCM storage modules

The green, purple and light blue line show the actually operating modules. The black characteristic displays the untouched PCM modules changing with the ambient temperature. This fact and the restricted scope of this thesis led to the decision to leave the module number constant. Another interesting point can be observed in figure 5.9. Apparently no module has met the time threshold for stable subcooling. This is indicated by the absence of spontaneous temperature peaks from ambient to approximately melting temperature. For further investigations it is of course necessary to consider a change in PCM volume. Therefore only the auxiliary storage volume ($V_{st,aux}$) and the charging massflow (\dot{m}_{st}) between the PCM and the water storage had been varied. A trend of the resulting solar fraction depending on the relation between \dot{m}_{st} and V_{st} for different auxiliary volumes is given in figure 5.10.

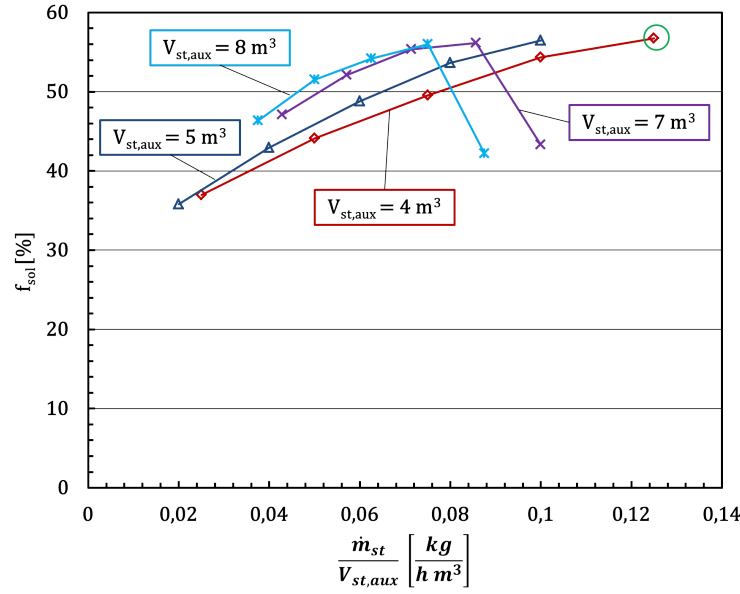


Figure 5.10: Achieved solar fraction of the different parameter variations

It can be observed that in general the solar fraction increases with the charging mass flow. Interesting however are the light blue and purple characteristic which show a drop at a critical massflow/volume relation. The increasing massflow causes a smaller supply temperature from the PCM storage and a higher mass removal which might be responsible for a averagely lower storage temperature level. This fact and the already higher storage volumes are responsible for a higher auxiliary heat request for 7 and 8 m³ at the highest massflow rate. Due to a high auxiliary heater power the penalty energies are very low and averagely 10 kW h throughout the variants which also shows that the consumed auxiliary energy is the dominant factor in the solar fraction definition (see section 2.4). It is most likely that such a critical point might be reached with the lower storage volumes as well (red and dark blue characteristic). Another interesting aspect is that the optimum massflow-volume ratio had been achieved with a massflow of either 500 or 600 kg/h almost independently of the auxiliary storage volume which might indicate a optimum massflow for the PCM module side lying between those values. Unfortunately figure 5.10 shows that with the chosen assumptions and boundary conditions a maximum solar fraction of only $f_{sol,B} = 57\%$ (green circle) can be achieved. The main problem as discussed in section 5.2.1 is the low heat transfer coefficient limited by the rather low thermal conductivity of the PCM and hence a rather low temperature level of the PCM load side. Although the main premise is not met with these systems, chosen results shall be given for the best investigated system (green circle) in the following part. Discussing all configurations in detail would go beyond the scope of this thesis. The configuration of the best system is therefore given in table 5.6.

Table 5.6: Resulting dimensions and solar fraction of the best Version B configuration

PCM volume	auxiliary volume	collector area	spec. collector massflow	charging massflow	aux. heater power	solar fraction
V_{pcm}	$V_{st,aux}$	A_C	$\dot{m}_{C,spec}$	\dot{m}_{st}	$P_{st,aux}$	f_{sol}
m ³	m ³	m ²	kg/(m ² h)	kg/h	kW	%
4.5	4	100	30	500	4	57

As stated above the main impact on the low solar fraction is the required temperature level to avoid penalty functions and therefore required auxiliary heat. The yearly integrated auxiliary energy results in $Q_{aux,B} = 3532.8$ kWh which is about ten times higher than the calculated value for auxiliary heat in the reference system. The penalty function for space heating is again zero and the DHW penalties are very low with only $Q_{pen,DHW,B} = 9.82$ kWh which shows a good user comfort behaviour. The quality of the results is given in figure 5.11 with the yearly integrated absolute values (red bars) and the relative values (blue bars). Again the yearly energy balances show a deviation below 0.1% of the highest values respectively which is considered as acceptable. As stated in section 3.4.1 the monthly energy balances showed higher deviations due to the explanations given.

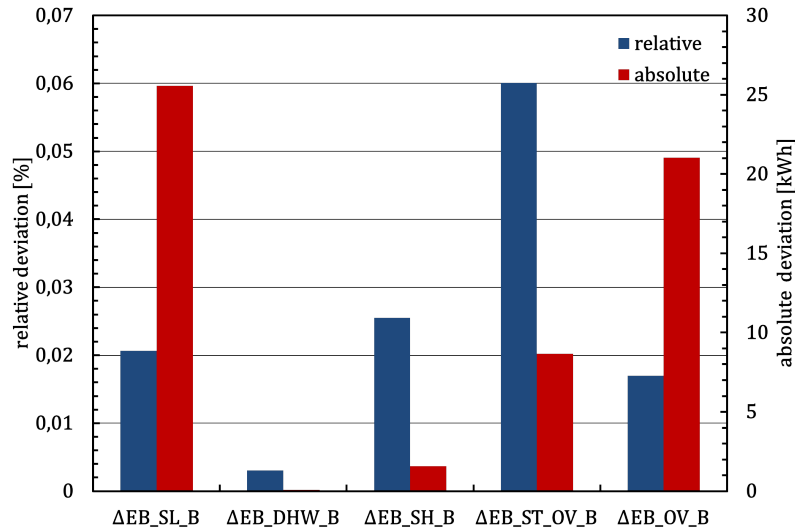


Figure 5.11: Yearly integrated absolute and relative energy balance deviations of Version B

Since the demand side of Version B remained the same compared to the reference system no major changes in efficiencies should occur in the SH and DHW loop. Slight changes, especially for exergetic consideration might occur due to a different temperature level inside the much smaller auxiliary storage. Therefore the subunit and overall yearly efficiencies are given in figure 5.12 to identify changes due to the new control strategies and of course the new PCM storage system. The storage efficiencies for the PCM and water storage alone are considered with PCM, B, A and W, B, A respectively as well as the combined system with subscript ST, A . The label "A" stands for Case A in efficiency definition since it was

found the most appropriate, according to the statements made in section 4.5. Red bars show energetic and blue bars show exergetic efficiencies.

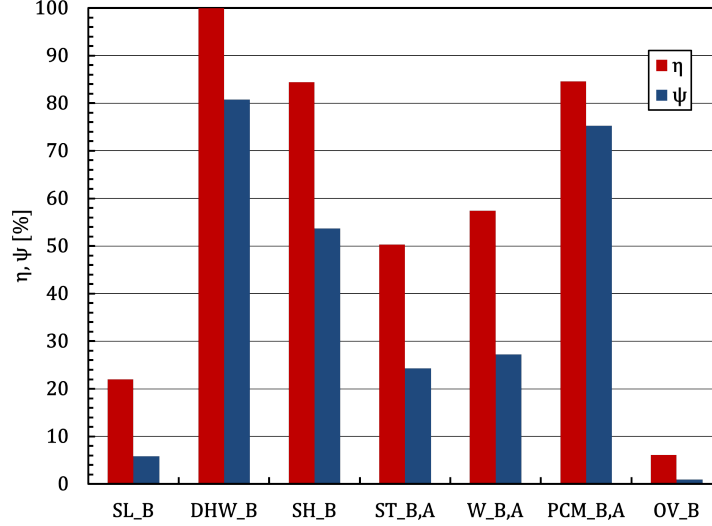


Figure 5.12: Yearly efficiencies of subunits and overall system of Version B

The first thing which stands out is an increased solar loop performance due to the PCM storage utilization compared to the reference system. The reason can be found in a higher degree of utilization in summer since modules are undergoing subsequent charge and discharge periods as can be seen in the temperature characteristics of figure 5.9. The energetic efficiency of the solar loop results in $\eta_{sl,B} = 22\%$ and the exergetic efficiency results in $\psi_{sl,B} = 5.8\%$. The combined storage efficiencies had decreased to values of $\eta_{st,B,A} = 50.3\%$ and $\psi_{st,B,A} = 24.3\%$ due to a higher auxiliary energy effort. The PCM storage alone shows high efficiencies both energetic and exergetic with $\eta_{pcm,B,A} = 84.6\%$ and $\psi_{pcm,B,A} = 75.3\%$. The high PCM values in contradiction to the lower water results show perfectly the major influence of the applied auxiliary heat especially in the exergetic point of view. Another point is a better loss behaviour of the PCM storage most likely due to the low thermal conductivity of the material. DHW and SH units show similar values as the reference system which is clear as mentioned above. The overall systems performance is slightly lower than the reference system although the fraction of solar radiation utilized has increased. The problem is the lower temperature level of the PCM load side energy and hence a higher auxiliary heat fraction to maintain the required set point temperature. The overall efficiencies result in $\eta_{OV,B} = 6.1\%$ and $\psi_{OV,B} = 0.99\%$.

The last considered point is the storage density of Version B. The calculation had been carried out similar to section 4.5 and as stated before only an estimation can be given according to the mathematical models utilized. As displayed in figure 5.7 the PCM system within the green system boundary consists of the PCM rack, the water storage and a circulating pump. In order to simplify the estimation pipes as well as the hydraulic connection of the PCM modules are neglected. The pump volume had been assumed to a volume of $V_{pu} = 0.003\text{m}^3$ (common circulating pump). For both systems the already defined limit temperatures are applied to calculate the storable energy (see section 4.5). The parameters are given in table 5.7.

Table 5.7: Parameters for storage density calculation of Version B

storable energy	storable water	storable energy	water mass	water volume	PCM mass	PCM volume	upper limit	lower limit
Q_w	Q_{pcm}	Q_w	m_w	V_w	m_{pcm}	V_{pcm}	ϑ_{up}	ϑ_{low}
kW h	kW h	kW h	kg	m ³	kg	m ³	°C	°C
255.54	538.14	538.14	4	3992	5400	4.5	95	40

In order to calculate the necessary volume a certain PCM storage layout had to be defined. The idea was to divide the storage rack into two piles with 12 modules each. Between the modules of each pile there has to be a certain vertical spacing for any kind of module support. This spacing had been chosen to $z_{mod} = 0.05$ m (figure 5.13, red volume). Between the piles, a corridor had been assumed of $z_{corr} = 0.5$ m for maintenance or montage (figure 5.13, green volume). The resulting volume had been considered as unusable space.

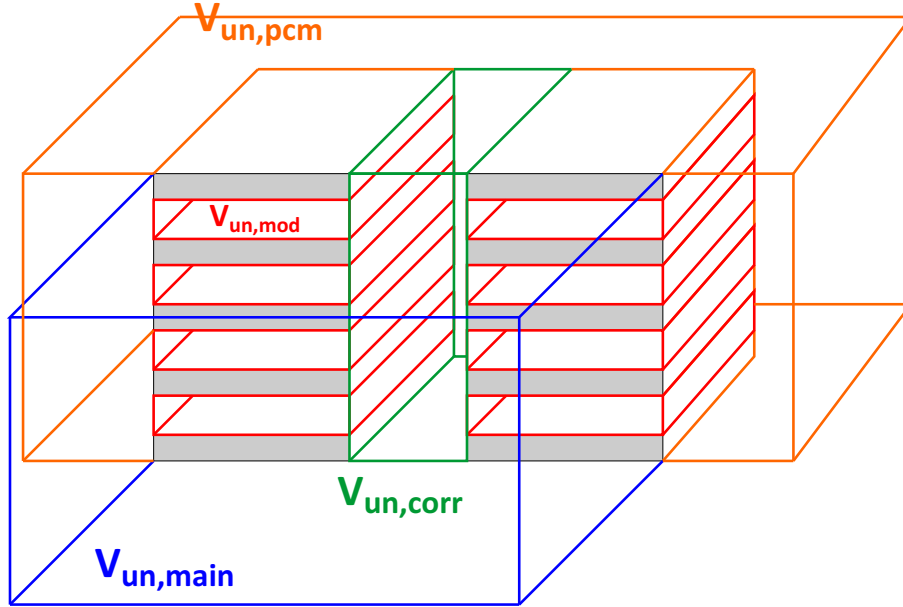


Figure 5.13: Definition of unusable volume for the PCM rack

If it is necessary to replace one module due to malfunction or maintenance, an additional volume has to be accessible to manipulate the considered module properly ($V_{un,main}$, blue volume). This unusable volume has to be equal to at least the PCM storage volume since any module can be defect. Similar to section 4.5, a space around the storages has to be accessible. Therefore a rectangular area had been defined where the lengths are defined by a one meter distance from the storage edges (for water and PCM) perpendicular to the lateral edges of the defined rectangle (orange volume). The resulting unusable volumes can be obtained from table 5.8.

Table 5.8: Unusable volumes in storage Version B

number of modules	around water	around PCM	PCM maintenance	module spacing	pile corridor
N	$V_{un,w}$	$V_{un,pcm}$	$V_{un,main}$	$V_{un,mod}$	$V_{un,corr}$
-	m^3	m^3	m^3	m^3	m^3
24	30.49	61.69	39	5.06	4.99
3	30.49	15.67	4.08	0.46	0

The auxiliary water tank volumes are calculated similar to section 4.5 with the utilized dimensions in Version B. A second case should be defined accounting for, that only 3 modules are actually in operation during the year (table 5.8, red bars in figure 5.14). Finally, the resulting storage densities are given in figure 5.14.

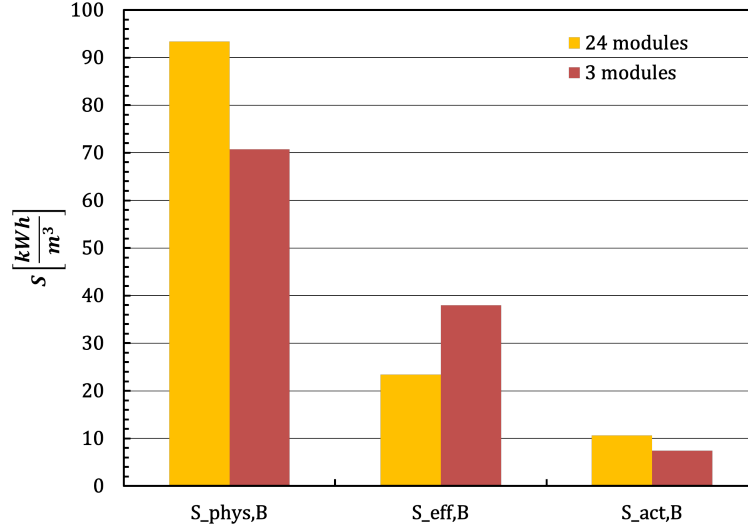


Figure 5.14: Estimated storage density of Version B

The orange bars display the original case with 24 modules and the red bars consider 3 modules. According to the definitions in section 2.4.2 the physical storage density $S_{phys,B}$ considers only the medium volume. $S_{eff,B}$ accounts for insulation, module heat exchanger, stratifying units and the pump. The actual storage density $S_{act,B}$ considers a probable unusable space as described above. The physical storage density states of course the highest values with 93.37 kWh/m^3 for the orange case and 70.75 kWh/m^3 in the red case. Interesting however, is that the latter value is lower than the original case which can be explained with the lower fraction of latent heat in the red case. The effective storage density of 3 modules shows better values since the ratio between medium volume and insulation volume is more dominant on the PCM side and since the auxiliary water storage is left unaltered and the PCM module number is reduced, a better effective storage density results. The fraction of unusable space however increases for the red case and causes a lower actual storage density. Additionally, similar considerations to section 2.4.2 regarding storage locations below the surface can be made.

5.4 Version C: Auxiliary water storage and bypass

The last version considers a bypass of the solar supply line to operate the PCM storage only in charge mode during summer and cover the DHW demand with the auxiliary storage. Therefore a controllable flow diverter (Type11f) had been installed in the supply line of the PCM rack which delivers a certain part of the massflow to the auxiliary storage. The return line of the respective water storage double port is then connected with a tee piece to the return line of the PCM storage. The hydraulic configuration and the energy fluxes are illustrated in figure 5.15

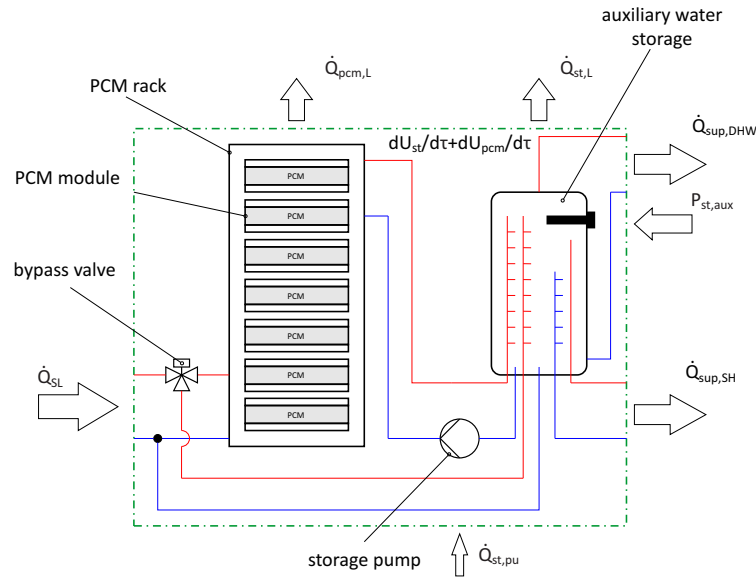


Figure 5.15: Schematic layout of the PCM storage with an auxiliary water storage and solar bypass

The basic dimensioning of the subsystems had again been adopted from the reference system. The control strategy of the solar loop can be exactly taken from section 5.2 or 5.3 as well as the auxiliary heater control from section 4.4. The basic storage pump control can be entirely obtained from the description in section 5.3 except the yearly schedule. The schedule for the storage pump in this version is displayed in figure 5.16.

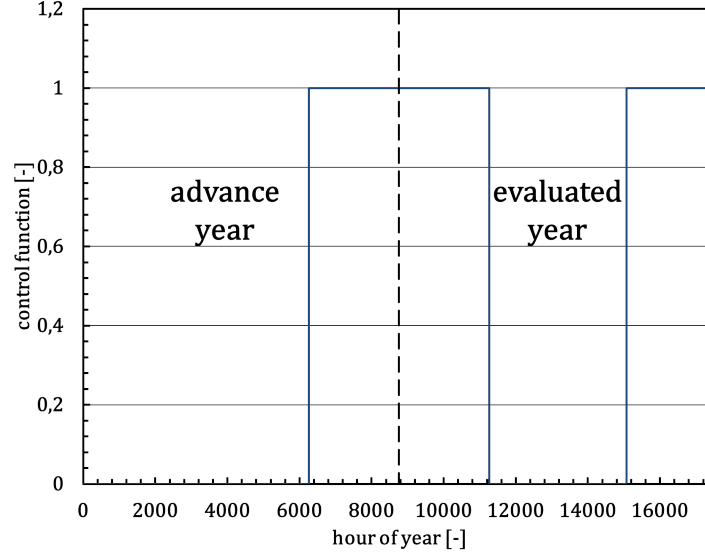


Figure 5.16: Storage pump schedule over two simulation years

In this case the discharge is avoided in summer periods where the demand should be covered by the solar bypass energy and the installed auxiliary heater. The flow diverter control signal consists of a bypass fraction f_{BP} and a yearly schedule similar to figure 5.16. The bypass fraction is defined as follows.

$$f_{BP} = \frac{\dot{m}_{BP}}{\dot{m}_{SL}} \quad (5.2)$$

Where \dot{m}_{BP} as bypass massflow and \dot{m}_{SL} as supply massflow from the solar loop. The bypass fraction had been among the changed factors during the parameter study. In order to increase the amount of supply energy during a charging period another control signal had been utilized to ensure that the bypass is only open if a temperature of a certain height in the water storage is lower than a defined set point. This signal had been determined with a differential controller. The required parameters are given in table 5.9.

Table 5.9: Control parameters of the solar bypass valve

higher control temperature	ϑ_{high}	°C	65
lower control temperature	ϑ_{low}	°C	storage node at $H_{rel} = 0.05$
higher temp. difference	ΔT_{high}	K	10
lower temp. difference	ΔT_{low}	K	5
monitoring temperature	ϑ_{mon}	°C	solar loop heat exchanger outlet
high limit cut-out	ϑ_{cut}	°C	98

Finally the bypass signal consists of f_{BP} multiplied with the differential signal from table 5.9. The bypass inlet of the water storage is again defined as stratified with the same relative height as the solar loop supply of the reference system.

5.4.1 Results of Version C

The results of Version B showed the best solar fraction with an auxiliary volume of 4 m^3 and a massflow of 500 kg/h . Therefore this configuration had been chosen as a starting point. The intention was to decrease the auxiliary heater power needed with the additional bypass supply. The collector area and the PCM volume remained the same, only the bypass fraction had been varied. A second storage volume of 5 m^3 had been considered to show the storage volume influence. The results of the variation are given in figure 5.17.

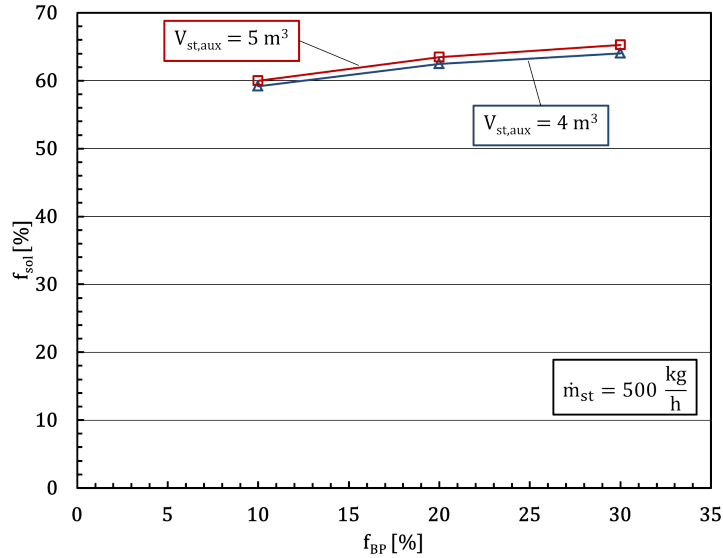


Figure 5.17: Resulting solar fraction (f_{sol}) of Version C in dependence of bypass fraction (f_{BP})

The blue line displays the solar fraction of a variation with 4 m^3 and the red characteristic shows a configuration with 5 m^3 auxiliary volume. The X-axis displays the bypass fraction. The solar fractions increase with increasing bypass massflow since penalties during summer are decreasing. Furthermore lower auxiliary energies are needed as expected in every case. The penalties are again about 10 kWh which is similar to Version B. The high auxiliary heater power can be identified as reason for the low penalties because of this similarity. The bypass energy only reduces the required auxiliary energy. Another problem might be the fact that the bypass mass flow is coupled with the solar loop pumps. An individual solar support circuit may provide more flexibility and enhance the control strategy which might lead to a further decrease of the auxiliary heat. An increase of the auxiliary volume shows a slight improvement of about 1% in every case. In order to achieve further improvement of the solar fraction, higher auxiliary volumes might be more effective since the bypass energies are rather high. Therefore a higher water storage volume might be necessary to store the supplied bypass energy and avoid a faster temperature drop because of smaller standby capacities and hence higher auxiliary energies. This would also provide more capacity for energy on a lower temperature level supplied from the PCM storage which would increase the degree of utilization of the PCM storage and a shift from bypass to PCM supply due to a more distinguished stratification. But still the solar fraction is far below the desired value of 95% . Nevertheless some results of the best operating bypass system should be discussed in the following. The main parameters of the considered configuration is given in table 5.10.

Table 5.10: Resulting dimensions and solar fraction of the best Version C configuration

PCM volume	auxiliary volume	collector area	spec. collector mass flow	bypass fraction	charging massflow	aux. heater power	solar fraction
V_{pcm}	$V_{st,aux}$	A_C	$\dot{m}_{C,spec}$	f_{BP}	\dot{m}_{st}	$P_{st,aux}$	f_{sol}
m^3	m^3	m^2	$kg/(m^2 h)$	%	kg/h	kW	%
4.5	5	100	30	30	500	4	64

The quality of the results can be seen in figure 5.18 with the blue colored relative and the red colored absolute deviations of the energy balance from zero.

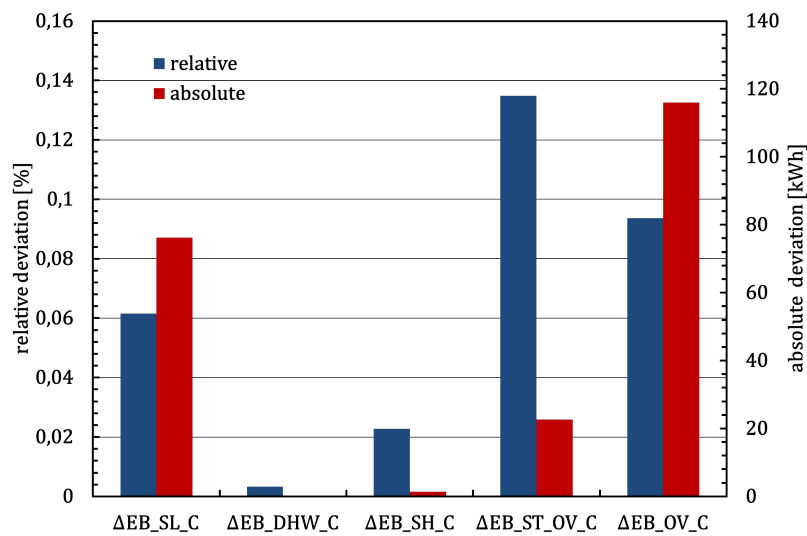


Figure 5.18: Annual relative and absolute energy balance deviations of Version C

The absolute and relative deviations values of the overall system and the storage have slightly increased in comparison to Version B but can be still considered as acceptable with an absolute deviation of the overall system with about 116 kWh. The resulting annual efficiencies shall again help to identify changes in the behaviour of subsystems and the overall system compared to previously discussed versions. Figure 5.19 provides the annual energetic (red bars) and exergetic (blue bars) efficiencies of the considered parts. The storage efficiency is again split up into PCM, water and the combined efficiency. As expected the DHW and SH efficiencies are almost identical to version B due to the fact that no changes of the demand side had been performed. A slight drop can be noticed in the exergetic efficiency of the DHW which is most likely caused by a averagely lower supply temperature level due to the different storage configuration.

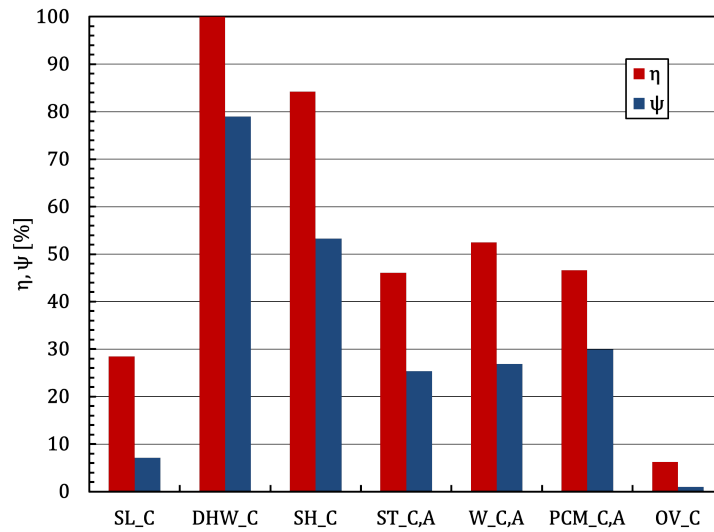


Figure 5.19: Annual energetic and exergetic efficiencies of the best Version C configuration

The space heating loop shows no recognizable changes. Very obvious differences can be observed in the solar loop values. The energetic efficiency has increased to $\eta_{SL,C} = 28.5\%$ and the exergetic value resulted in $\psi_{SL,C} = 7.1\%$. At the same time the PCM efficiency has dropped drastically to only $\eta_{pcm,C,A} = 46.7\%$ and $\psi_{pcm,C,A} = 29.8\%$. The water storage stayed in the same magnitude but with slightly lower values than version B. Hence the resulting combined storage efficiencies are slightly lower than Version B with $\eta_{st,C,A} = 46.7\%$ and $\psi_{st,C,A} = 29.8\%$. The reason for the decrease in storage and an increase of solar loop efficiencies can be found in figure 5.20 displaying the mean PCM temperatures of each module. The high degree of utilization of the solar radiation can be found in the charging period of the PCM modules until every module is subcooled. When every module is subcooled the control chooses a module to charge which is then left to cool against ambient without purpose because no discharge demand is given in summer (see figure 5.16).

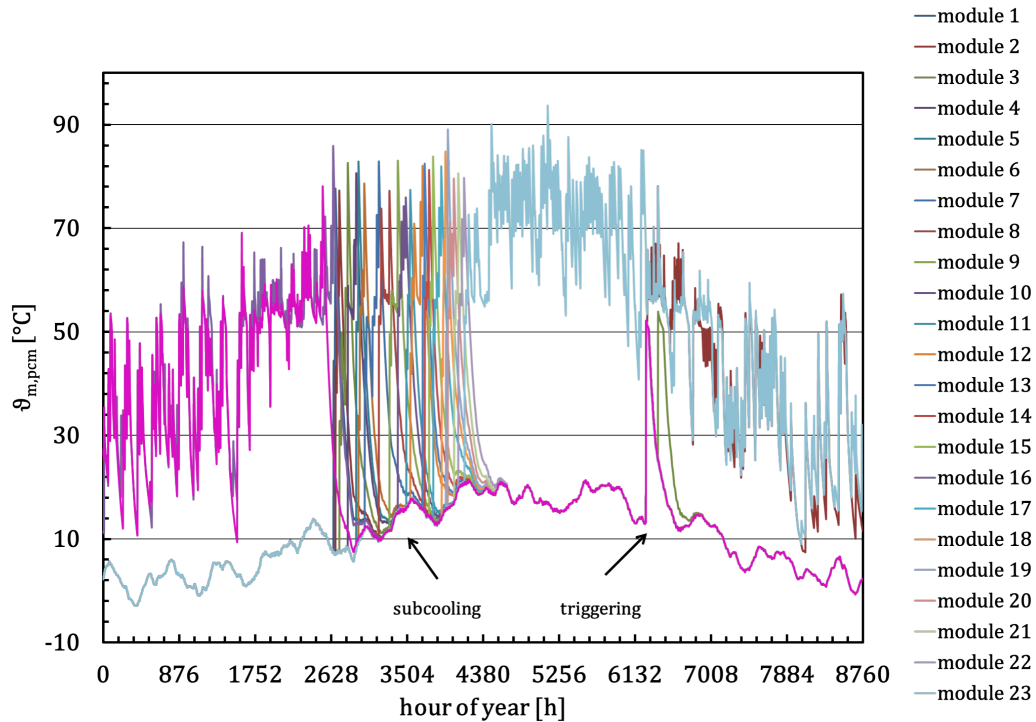


Figure 5.20: Hourly average mean PCM temperatures of Version C

Hence the degree of utilization of the solar loop increases because of the unnecessarily charged module in the second half of summer, the charged and subcooled modules and the constantly used bypass energy. At the same time, losses of the PCM storage are high because of the not utilized sensible heat of subcooling modules and the unnecessarily charged module which loses its energy without being harnessed. Since the bypass massflow had been rigidly connected with solar pump signal, a switch to avoid this "dummy charge" had not been implemented in the bypass control strategy. Therefore a more flexible and maybe independent bypass circuit has to be considered instead of the rigid implemented control strategy where the bypass massflow depends on the solar unit pump control. It is clear that with the high collector area and no discharging during summer every module is fully charged and subcooled already before the summer period has ended. This can be seen in figure 5.20 where all modules are subcooled after approximately 4500 hours of the year, which is about in the middle of July. For future investigations it might be essential to consider a higher number of storage modules. But figure 5.20 may also show a different picture. The spontaneous temperature peaks appearing at the start of the discharge period are showing up only in the beginning. In fact, the control strategy triggers the subcooled modules because of a discharge massflow, but very close after another, which indicates that the useful energy of a triggered module might not be sufficient (in terms of temperature level for example) and therefore subsequently the next module is triggered and so on. Furthermore only three modules are in actual operation during the discharge period similar to section 5.3 In conclusion, the subcooled modules might not bring the desired additional advantage during a discharge period and may therefore be omitted in favor of a lower storage volume. It is very important to carry out further investigation in this regard.

The last discussed aspect shall be the storage density. The calculations had been carried out according to the previous section with the identical unusable volume definition and simplifications. Additionally the tee piece and the flow diverter had been neglected as well.

Two cases should be considered again. The first case considers 24 modules (orange bars), see also tables 5.7 and 5.8. The second case considers only the three operating modules (red bars). Hence the PCM storage density is left unaltered compared to section 5.3 just the auxiliary volume has changed to 5 m^3 . The resulting values are given in figure 5.21.

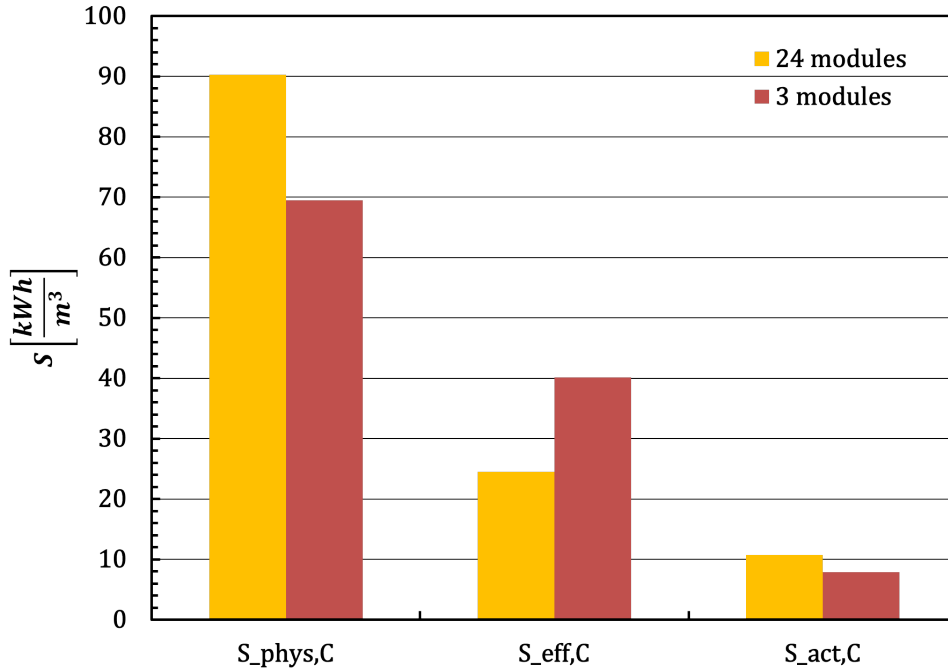


Figure 5.21: Storage density of Version C

The physical density results in 90.27 kWh/m^3 and 69.51 kWh/m^3 in the orange and red case respectively which is slightly lower than Version B because of the higher auxiliary volume. The effective storage density results in 24.51 kWh/m^3 for the orange case and 40.14 kWh/m^3 for the red case. This states an improvement compared to Version B and illustrates that the major impact in terms of insulation and built-in components lies on the PCM side. Finally the actual storage density shows values of 10.71 kWh/m^3 for the orange case and 7.86 kWh/m^3 for red case which is a minor decrease due to the additional unusable space in the same magnitude of the auxiliary volume.

6 CONCLUSION

The objective of this thesis was to carry out a basic performance estimation of a newly developed PCM storage concept in seasonal solar thermal systems context. It was the aim to find promising ways of system integration and to point out strengths, weak points and improvement potential in order to support future decisions in construction and development. The main premise therefore had been to achieve a solar fraction of 95 %. Transient system simulations in combination with first and second law analysis has been utilized for the performance evaluation as well as storage density definitions and penalty functions. Therefore the simulation environment TRNSYS17.1 has been chosen to perform the calculations. The energy and exergy analysis had been directly implemented into TRNSYS via equation statements. In order to provide a mathematical model of the considered PCM storage a new TRNSYS Type had been developed by Christoph Moser at the same time of this thesis.

To maintain comparability a predefined reference system with a conventional water storage had been set up within TRNSYS17.1. A Parameter variation had been carried out in order to find a configuration which meets the defined target value. A storage volume of 50 m^3 with a collector field area of 100 m^2 resulted in a solar fraction of 95 %. The energetic and exergetic analysis had identified the energy conversion of the solar collector as the major loss factor both energetically and exergetically. The overall degree of utilization of the available solar irradiation on the collector area throughout one simulated year resulted in 6.5 % and an exergetic efficiency of 1 %. Especially the exergetic consideration of solar radiation in this context is a highly discussed topic. Problems with exergetic analysis using TRNSYS could have been pointed out where the assumptions of transition temperatures and the modelling of internal exergies are the most challenging. Furthermore difficulties of efficiency definitions in non steady systems had been discussed.

On the basis of the reference system three different PCM integration versions had been defined and analysed. The first variant was a direct integration of a PCM storage rack consisting of 24 modules box shaped modules with an inline auxiliary heater located in the demand supply line (Version A). The results showed massive penalty functions for the DHW loop caused by an insufficient heat transfer coefficient. An estimation showed that a HTC of approximately $450\text{ W}/(\text{m}^2\text{ K})$ throughout an entire draw off has to be maintained to avoid high penalty function. Since the solar fraction resulted in negative values throughout due to the massive penalties no further analysis had been made. The second configuration had been a combination of the PCM storage on the source side and an auxiliary water tank with an integrated auxiliary heater on the demand side (Version B). The PCM storage charges the water storage. Charging massflows and storage volumes had been varied. The best performing configuration had been found in a storage volume of 4 m^3 and a charging massflow between the auxiliary tank and PCM of 500 kg/h . This configuration resulted in a solar fraction of only 57 %. The reason might again be the additional heat transfer and the resulting low temperature level. The PCM showed a very good loss behaviour which resulted in an annual energetic efficiency of about 84 %. Version B showed promising values in physical and actual storage densities compared to the reference system but fell below if the effective case is considered. For the third configuration a bypass line into the auxiliary water tank had assumed to support the charging in winter and takeover the entire DHW demand during summer (Version C). The results showed an improvement in solar fraction up to 64 % for a 5 m^3 auxiliary tank. It might be necessary to increase the water storage in order to provide a higher standby capacity. An enhanced system control strategy is essential to avoid unnecessary losses and to increase the solar fraction.

In conclusion it can be said that a basic performance estimation had been carried out. Non

of the investigated PCM systems could provide the requested solar fraction of 95 % where the bypass system showed the highest potential. The results showed that it is difficult to provide DHW draw offs at a high temperature level and high heat rates therefore an additional auxiliary water storage might be inevitable for further system development. It will be necessary to develop enhanced discharge strategies to optimize the PCM and auxiliary store interaction and therefore the entire systems performance. Decoupling the hot water preparation from the PCM storage might be a further possibility to improve the system performance since SH penalties remained zero throughout the entire calculations. Furthermore the use of a floor heating system based on a lower temperature level, for example with a supply temperature of 37 °C or 35 °C and a maximum floor temperature of 29 °C (Recknagel et al., 2007), can increase the PCM system performance instead of the utilized radiator system and might be therefore a more suitable alternative. One of the major challenges is to improve the heat transfer coefficient of the PCM module. Optimizing the heat transfer coefficient within the given box shaped design regarding the effective heat exchanger area is a necessary task for future investigations.

The advantage of a subcooled module might not be as effective as assumed due to a low temperature level after triggering and the limited heat transfer coefficient, follow up investigations have to be performed in this regard. But again with a floor heating system the temperature level after the triggering can be sufficient, which can result in a major improvement regarding systems performance. Furthermore the appropriate number of storage modules has to be found in following work concerning a possible DHW decoupling, enhanced discharge control strategies and the effectiveness of subcooled modules. In terms of system parameter like storage volume further research has to be carried out since only basic estimations had been performed. To improve storage densities further improvement in terms of insulation and minimizing unusable space will be necessary to maintain the advantage of compactness.

This thesis provides basic knowledge regarding system integration and performance of an innovative PCM storage system for seasonal application. Furthermore improvement potential and important functional aspects could be pointed out which can support future design and integration decisions.

LITERATURE

- Araki, N., Futamura, M., Makino, A., and Shibata, H. (1995). Measurements of thermo-physical properties of sodium acetate hydrate. *International Journal of Thermodynamics*, 16(6):1455–1466.
- Baehr, H. D. and Kabelac, S. (2009). *Thermodynamik Grundlagen und technische Anwendungen*. Springer, Berlin; Heidelberg.
- bbsolar (2014). Powertank-die neue Latenzellen-Generation. Online. <http://www.bbsolar.ch/paraffinspeicher-powertank.html>, 21.01.2014.
- Bertsch, F., Fumey, B., Heimrath, R., Dröscher, A., and Schranzhofer, H. (2013). COMTES Deliverable 1.2: Description of boundary conditions for each storage technology and of the models for the reference system. Internal project report, unpublished.
- Blanco, H. T. (2012). *Comparison and optimization of building energy supply systems through exergy analysis and its perspectives*, volume 11. Fraunhofer Institute fuer Bauphysik IBP, <https://www.morebooks.de/store/de/book/comparison-and-optimization-of-building-energy-supply-systems-through-exergy-analysis-and-its-perspectives/isbn/978-3-8396-0452-6>.
- Brandstätter, C. (2014). Energy and exergy analysis of thermal energy storage systems. Bachelorthesis, Institute of Thermal Engineering, Graz University of Technology.
- Candau, Y. (2003). On the exergy of radiation. *Solar Energy*, 75(3):241 – 247.
- COMTES (2011). Annex I to the Grant Agreement (description of work). unpublished. EU-Project number: 295568.
- Dincer, I. and Rosen, M. A. (2011). *Thermal Energy Storage*. Wiley & Sons, 2 edition.
- Dröscher, H. (2012). The chemical system of sodium acetate / water as phase change material (PCM) for the use in seasonal energy storage. Master’s thesis, Institute of Thermal Engineering, Graz University of Technology.
- Duffie, J. A. and Beckman, W. A. (2006). *Solar Engineering of Thermal Processes*. John Wiley & Sons, 3. auflage edition.
- Ezan, M. A., Ozdogan, M., Gunerhan, H., Erek, A., and Hepbasli, A. (2010). Energetic and exergetic analysis and assessment of a thermal energy storage (TES) unit for building applications. *Energy and Buildings*, 42(10):1896 – 1901.
- Fan, J., Furbo, S., Chen, Z., Andersen, E., and Perers, B. (2010). Heat transfer capacity of a heat exchanger module for seasonal heat storage. *Department of Civil Engineering, Technical University of Denmark, Kgs. Lyngby, Denmark*, -:12.
- Farahat, S., Sarhaddi, F., and Ajam, H. (2009). Exergetic optimization of flat plate solar collectors. *Renewable Energy*, 34:1169–1174.
- Furbo, S., Fan, J., Andersen, E., Chen, Z., and Perers, B. (2012). Development of seasonal heat storage based on stable supercooling of a sodium acetate water mixture. *Energy Procedia*, 30(0):260 – 269. 1st International Conference on Solar Heating and Cooling for Buildings and Industry (SHC 2012).

- Gunerhan, H. and Hepbasli, A. (2007). Exergetic modeling and performance evaluation of solar water heating systems for building applications. *Energy and Buildings*, 39:509–516.
- Haller, M. (2012). *TRNSYS Type832v5.00 "Dynamic Collector Model by Bengt Perers" Updated Input- Output Reference*. Hochschule für Technik Rapperswil.
- Heimrath, R. (2004). *Simulation, Optimierung und Vergleich solar thermischer Anlagen zur Raumwärmenutzung für Mehrfamilienhäuser*. PhD thesis, Institute of Thermal Engineering, Graz University of Technology.
- Heimrath, R. and Haller, M. (2007). The reference heating system, the template solar system of task 32. Technical Report Report A2 of Subtask A, Institute of Thermal Engineering, Graz University of Technology.
- Heinz, A. (2007). *Application of Thermal Energy Storage with Phase Change Materials in Heating Systems*. PhD thesis, Institute of Thermal Engineering, Graz University of Technology.
- Heinz, A. and Schranzhofer, H. (2007). *Type840: Model for the transient simulation of water- or PCM slurry tanks with integrated PCM modules*. Insitute of thermal engineering TU-Graz.
- Heinz, A. and Schranzhofer, H. (2010). Thermal energy storage with phase change materials in solar combisystems - a promising solution? In *Proceedings of the EuroSun - ISES-Europe Solar Congress*. ISES Europe EuroSun, ISES Europe.
- Heizkörper (2013). Thermobatterie. Online. <http://www.thermobatterie.net/thermobatterie.html>, 21.06.2013.
- Holst, S. (1996). *TRNSYS- Models for radiator heating systems*. Bayrisches Zentrum für angewandte angewandte Energieforschung e.V. (ZAV). unpublished.
- Incropera, F. P., Bergman, T. L., DeWitt, D. P., and Lavine, A. S. (2011). *Fundamentals of Heat and Mass Transfer*. John Wiley Sons, New York, 7th edition.
- IZES (2010). Prüfbericht Nr.: KT10/14, Velux CLI U12 5000 Kollektor. Technical report, Institut für Zukunftstenergiesysteme (IZES), Testzentrum Saarbrücken (tzb). unpublished.
- Kendrick, C. and Walliman, N. (2007). Removing unwanted heat in lightweight buildings using phase change material in building components: Simulation modelling for pcm plasterboard. *Architectual Science Review*, 50(265-273):9.
- Lane, G. A. (1983). *Solar Heat Storage: Latent Heat Material Volume I: Background and Scientific Principles*, volume 1. CRC Press , Inc.
- Lane, G. A. (1986). *Solar Heat Storage: Latent Heat Material Volume II: Technology*, volume 2. CRC Press , Inc.
- Mehling, H. and Cabeza, L. F. (2008). *Heat and cold storage with PCM*. Springer.
- Moser, C. (2012). Optimierte Einbindung von Energiespeichern in industrielle Prozesse. Master's thesis, Institute of Thermal Engineering, Graz University of Technology.
- Moser, C. (2014). Phase change material (PCM) storage model-type 8888. Internal project report, unpublished.

- Örtel, K. (2004). Vorrichtung und Verfahren zur Kühlung des Wärmematerials eines Latentwärmespeichers, patent number: DE 103 03 498 A1 2004.08.12.
- Petela, R. (2003). Exergy of undiluted thermal radiation. *Solar Energy*, 74(6):469 – 488.
- Rathgeber, C. and Eberhard, L. (2013). TASK42/29 presentation: Working Group c1, c1.3-Economical limits. Ljubljana, unpublished.
- Recknagel, H., Sprenger, E., and Schramek, E. R. (2007). *Taschenbuch für Heizung und Klimatechnik*. Oldenbourg Industrie Verlag, 73 edition.
- Remund, J., Müller, S., Kunz, S., Huguenin-Landl, B., Schmid, C., and Schilter, C. (2013). *Metenorm Global Meteorological Database Handbook Part 2 : Theory*. Meteotest, 7 edition.
- Rubitherm (2014). Produktbeschreibung CSM Platte & PCM Kompaktspeicher. Online. <http://www.rubitherm.de>, 21.01.2014.
- Sandnes, B. (2003). *Exergy Efficient Production, Storage and Distribution of Solar Energy*. PhD thesis, Department of Physics Faculty of Mathematics and Natural Sciences University of Oslo.
- SEL (2012). *TRNSYS 17 User Manual*. Solar Energy Laboratory, University of Wisconsin, Madison Wisconsin, USA.
- SketchUp (2014). Google sketchup. Online. <http://www.sketchup.com/de/products/sketchup-pro>, 31.01.2014.
- Sole, Medrano, Castell, Nogues, Mehling, and Cabeza (2008). Energetic and exergetic analysis of a domestic water tank with phase change material. *International Journal of Energy Research*, 32(3):204–214.
- Stieglitz, R. and Heinzl, V. (2012). *Thermische Solar Energie*. Springer.
- TESS (2012). *TESSLibs 17: Component Libraries for the TRNSYS Simulation Environment*. Thermal Energy Systems Specialists (TESS), Madison Wisconsin, USA.
- VDI (2006). *VDI-Wärmeatlas*. Springer Verlag, 10 edition.
- Weiss, W., Streicher, W., Suter, J.-M., Kovacs, P., Letz, T. and BerLetz, I., Jordan, U., and Vajen, K. (2003). *Solar heating systems for houses, A design Handbook for solar combisystems*. James & James.
- Wilhelms, Zass, Vajen, Kerskes, and Mueller-Steinhagen (2009). Bewertung verschiedener Wärmespeicherkonzepte hinsichtlich ihres effektiven Raumbedarfs. Technical report, UNI Kassel, UNI Stuttgart.
- Zalba, B., Marin, J., Cabeza, L. F., and Mehling, H. (2003). Review on thermal energy storage with phase change: materials, heat transfer analysis and applications. *Applied Thermal Engineering* 23, 23(3):251–283.
- Zamfirescu, C. and Dincer, I. (2009). How much exergy one can obtain from incident solar radiation? *Journal of Applied Physics*, 105(4):–.

LIST OF FIGURES

2.1	Simple thermodynamic system	7
2.2	Change of state	7
2.3	Carnot cycle of a heat engine (Baehr and Kabelac, 2009)	9
2.4	Conversion model for the exergy of solar radiation according to (Candau, 2003)	11
2.5	Comparison of exergy approaches for the total horizontal radiation during one day	12
2.6	Ideal h/T -characteristic of a PCM	13
2.7	Energy and exergy fluxes of a flat plate collector	15
2.8	Mathematical approach of the Type840 model according to (Heinz and Schranzhofer, 2007)	18
2.9	Energy balance of a considered storage node (Moser, 2012)	18
2.10	Global energy and exergy fluxes of a water storage	20
2.11	Mathematical approach of the T8888 model according to (Moser, 2014)	21
2.12	Interaction between heat exchanger nodes (k) and PCM node (j)	22
2.13	h/T characteristics of Type8888 (Moser, 2014)	25
2.14	Energy and exergy fluxes of a PCM storage module	26
2.15	Exergy/ T characteristics of Type8888 (Moser, 2014)	27
2.16	Energy and exergy fluxes of counterflow heat exchanger	29
2.17	Schematic T/x characteristics of a counter flow heat exchanger according to (Incropera et al., 2011)	29
2.18	Schematic T/x characteristics of an ideal heat exchanger and $\dot{C}_h < \dot{C}_c$	29
2.19	Schematic T/x characteristics of an ideal heat exchanger and $\dot{C}_h > \dot{C}_c$	29
2.20	Energy and exergy fluxes of a radiator	31
2.21	Energy and exergy fluxes of a mixing valve	34
2.22	Energy and exergy fluxes of a Pipe	35
2.23	Plug flow approach of Type709 according to (TESS, 2012)	36
2.24	Model of circulation pump	38
2.25	Screenshot of the Simulation Studio	44
2.26	Proforma of a TRNSYS type	44
2.27	GUI of the EQUATION statement	45
2.28	Regime data of a building Airnode within TRNBUILD	46
3.1	Geometrical model of the reference building (Bertsch et al., 2013)	47
3.2	Weekly integrated energy demand for hot water preparation	50
3.3	Daily heat gain and occupation obtained from (Heimrath and Haller, 2007)	51
3.4	Weekly schedule of electrical gains (Heimrath and Haller, 2007)	51
3.5	Monthly horizontal irradiation and average temperature of Zurich	52
3.6	Ambient temperature characterisitic over the year and calculated sinus curve	53
3.7	h/T measurement of SAT 46 % with DSC	54
3.8	Subcooling process displayed in an ideal h/T -diagram	55
3.9	Energy balance deviation due to pump activation in PCM systems	57
3.10	Detailed look on the first pump activation of figure 3.9	57
4.1	Sketch of the considered reference system according to (Bertsch et al., 2013)	60
4.2	Components and energy fluxes of the solar unit	61
4.3	Location and layout of the collector array in respect to the building structure	62
4.4	Components and energy fluxes of the DHW unit	65
4.5	Components and energy fluxes of the SH unit	66
4.6	Considered water storage unit and energy fluxes	69

LIST OF FIGURES

4.7	Annual integrated absolute and relative deviation of the reference system energy balances	73
4.8	Annual energy balance of the solar unit	74
4.9	Annual exergy balance of the solar unit	75
4.10	Annual energy balance of the domestic hot water supply	76
4.11	Annual exergy balance of the domestic hot water supply	76
4.12	Annual energy balance of the space heating unit	77
4.13	Annual exergy balance of the space heating unit	78
4.14	Annual energy balance of the water storage	79
4.15	Annual exergy balance of the water storage	79
4.16	Annual energy balance of the overall system	80
4.17	Annual exergy balance of the overall system	81
4.18	Detailed irreversibility distribution of the overall system	81
4.19	Comparison between auxiliary energy and penalties of the reference system .	82
4.20	Overview of the annual energetic and exergetic efficiencies of the subunits and overall system	83
4.21	Annual evaluated efficiency cases of the storage system	84
4.22	Monthly evaluated energetic storage efficiencies according to section 2.4 . . .	84
4.23	Monthly evaluated storage exergetic efficiencies according to section 2.4 . . .	85
4.24	Overview of the monthly energetic efficiencies of the subunits and overall system	86
4.25	Fraction of monthly energy fluxes of the storage system	87
4.26	Overview of the monthly exergetic efficiencies of the subunits and overall system	88
4.27	Estimated storage density of the water based TES in the reference system . .	90
5.1	Layout of the overall PCM system	91
5.2	Structure and dimensions of a PCM module (left) and detail of a top heat exchanger section (right)	92
5.3	Schematic layout of the directly integrated PCM storage	94
5.4	DHW penalties of Version A during the year	96
5.5	Relevant temperature and mass flow characteristics during a DHW draw off in July	96
5.6	Estimated heat transfer coefficient of the PCM module	97
5.7	Schematic layout of the PCM storage with an auxiliary water storage	98
5.8	Storage pump schedule over two simulation years	99
5.9	Hourly mean temperature characteristics of PCM storage modules	100
5.10	Achieved solar fraction of the different parameter variations	101
5.11	Yearly integrated absolute and relative energy balance deviations of Version B	102
5.12	Yearly efficiencies of subunits and overall system of Version B	103
5.13	Definition of unusable volume for the PCM rack	104
5.14	Estimated storage density of Version B	105
5.15	Schematic layout of the PCM storage with an auxiliary water storage and solar bypass	106
5.16	Storage pump schedule over two simulation years	107
5.17	Resulting solar fraction (f_{sol}) of Version C in dependence of bypass fraction (f_{BP})	108
5.18	Annual relative and absolute energy balance deviations of Version C	109
5.19	Annual energetic and exergetic efficiencies of the best Version C configuration	110
5.20	Hourly average mean PCM temperatures of Version C	111
5.21	Storage density of Version C	112
A.1	Hourly average storage node temperatures of different relative heights	123

LIST OF FIGURES

A.2	Annual energy balance of the overall system in Version B	124
A.3	Annual exergy balance of the overall system in Version B	124
A.4	Annual energy balance of the combined storage in Version B	125
A.5	Annual exergy balance of the combined storage in Version B	125

LIST OF TABLES

2.1	Resulting parameters for a Type840 example	19
3.1	Wall areas of the reference building according to their orientation (Bertsch et al., 2013)	48
3.2	Thermal properties of the respective wall types and windows (Bertsch et al., 2013)	48
3.3	Basic data of the DHW demand (Heimrath and Haller, 2007)	49
3.4	Heat gain distribution per person seated at rest according to (Heimrath and Haller, 2007)	50
3.5	Material properties of the considered PCM	54
3.6	Phase transition properties of the utilized PCM	55
3.7	Utilized simulation parameter	56
4.1	Properties of the solar loop HTF (VDI, 2006; Heimrath and Haller, 2007) . .	61
4.2	Collector parameters obtained from (IZES, 2010)	62
4.3	Basic geometrical data of the collector obtained from (IZES, 2010)	62
4.4	Control parameters of the solar loop pumps	63
4.5	Design parameter of the SH unit obtained from (Bertsch et al., 2013)	66
4.6	Hard coded nominal conditions of Type362 (Holst, 1996)	67
4.7	Design parameter of the radiator	68
4.8	Relative heights of double ports calculated according to (Heimrath and Haller, 2007)	70
4.9	Storage properties according to (Heimrath and Haller, 2007)	71
4.10	Control parameters of the auxiliary heater	71
4.11	Resulting dimensions and solar fraction of the reference system	72
4.12	Parameter for storage density calculation of the reference system	88
4.13	Volume distribution for storage density calculations according to section 2.4.2	89
5.1	PCM module parameter and dimensions	92
5.2	PCM storage parameter	92
5.3	Control parameters of solar loop pumps in Version A	94
5.4	System parameters of Version A	95
5.5	Control parameters of the storage pump in Version B	99
5.6	Resulting dimensions and solar fraction of the best Version B configuration .	102
5.7	Parameters for storage density calculation of Version B	104
5.8	Unusable volumes in storage Version B	105
5.9	Control parameters of the solar bypass valve	107
5.10	Resulting dimensions and solar fraction of the best Version C configuration .	109
A.1	Properties of the solar loop pipes for $\dot{m}_{Coll,spec} = 30 \text{ kg}/(\text{m}^2 \text{ h})$	122
A.2	Thermal properties of pipe material and insulation	122
A.3	Properties of the DHW loop pipes for $\dot{m}_{DHW,max} = 1400 \text{ kg}/\text{h}$	122
A.4	PID controller parameter	122
A.5	Properties of the DHW loop pipes for $\dot{m}_{SH,max} = 682.2 \text{ kg}/\text{h}$	123

A APPENDIX

Additional Solar loop properties

Table A.1: Properties of the solar loop pipes for $\dot{m}_{Coll,spec} = 30 \text{ kg}/(\text{m}^2 \text{ h})$

No.	length	inner diameter	wall thickness	insulation diameter
n	L_p	d_{iw}	s_p	d_{ins}
-	m	m	m	m
Pipe 1	14	0.0438	0.002	0.131
Pipe 2	1	0.0438	0.002	0.131
Pipe 3	28	0.0438	0.002	0.131
Pipe 4	11	0.0382	0.002	0.114
Pipe 5	11	0.0382	0.002	0.114

Table A.2: Thermal properties of pipe material and insulation

thermal conductivity steel	thermal conductivity insulation
λ_{st}	λ_{ins}
W/(m K)	W/(m K)
50	0.042

Additional DHW loop properties

Table A.3: Properties of the DHW loop pipes for $\dot{m}_{DHW,max} = 1400 \text{ kg}/\text{h}$

No.	length	inner diameter	wall thickness	insulation diameter
n	L_p	d_{iw}	s_p	d_{ins}
-	m	m	m	m
Pipe 1	11	0.0299	0.002	0.0898
Pipe 2	1	0.0299	0.002	0.0898

Additional SH loop properties

Table A.4: PID controller parameter

proportional	integral	differential	Temperature width
γ_P	γ_I	γ_D	ΔT_{PID}
-	-	-	K
0.8	0.05	0	3

Table A.5: Properties of the DHW loop pipes for $\dot{m}_{SH,max} = 682.2 \text{ kg/h}$

No.	length	inner diameter	wall thickness	insulation diameter
n	L_p	d_{iw}	s_p	d_{ins}
-	m	m	m	m
Pipe 1	8	0.0208	0.002	0.0626
Pipe 2	7	0.0208	0.002	0.0626
Pipe 3	1	0.0208	0.002	0.0626
Pipe 4	1	0.0208	0.002	0.0626
Pipe 5	15	0.0208	0.002	0.0626
Pipe 6	12	0.0208	0.002	0.0626

Additional results of the reference system

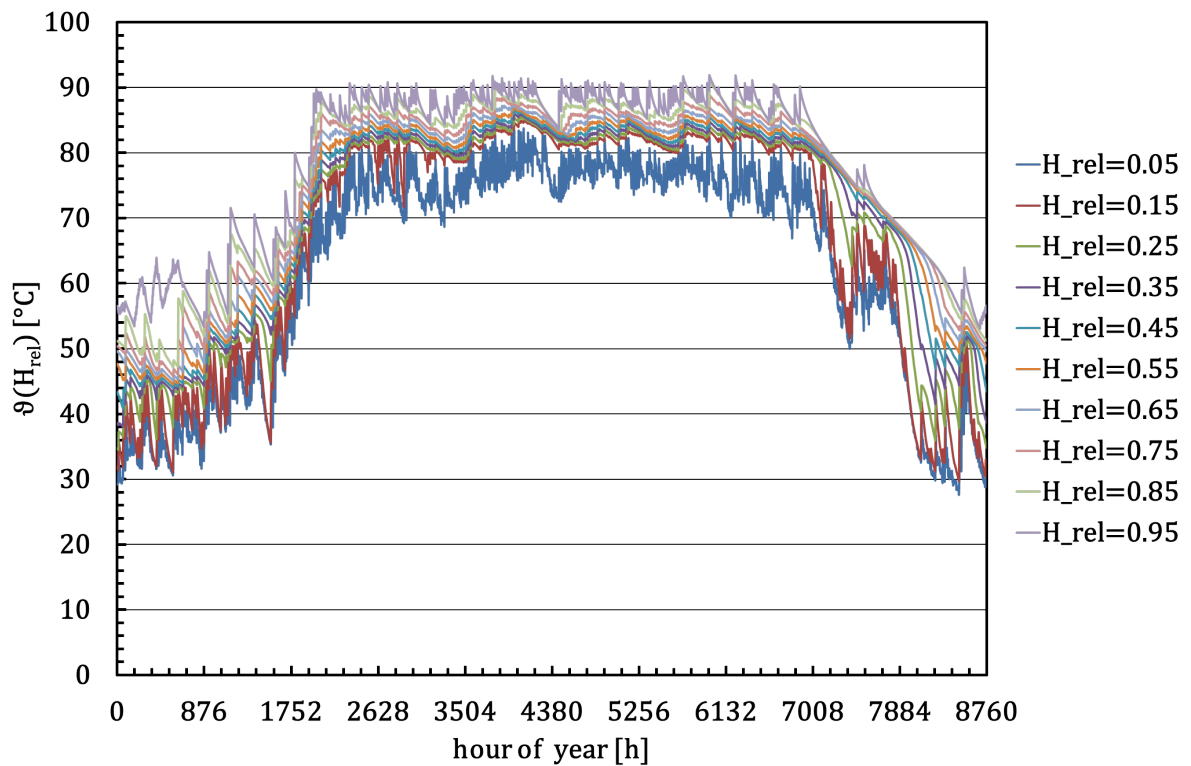


Figure A.1: Hourly average storage node temperatures of different relative heights

Additional results of Version B

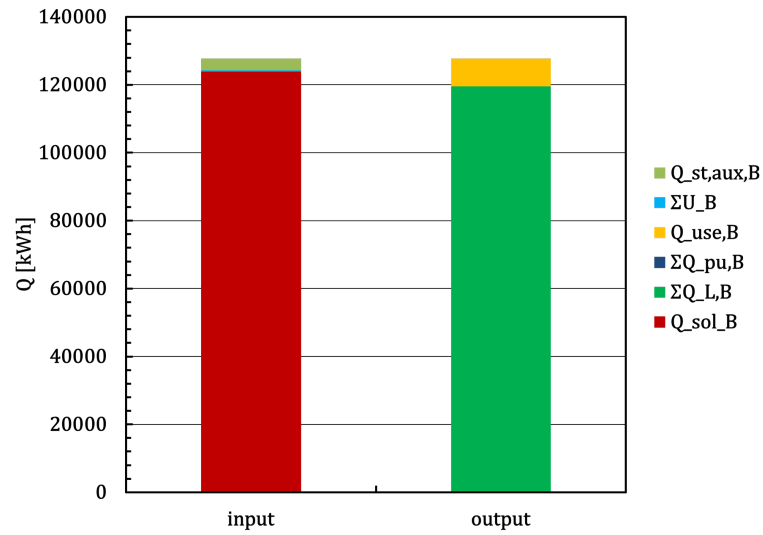


Figure A.2: Annual energy balance of the overall system in Version B

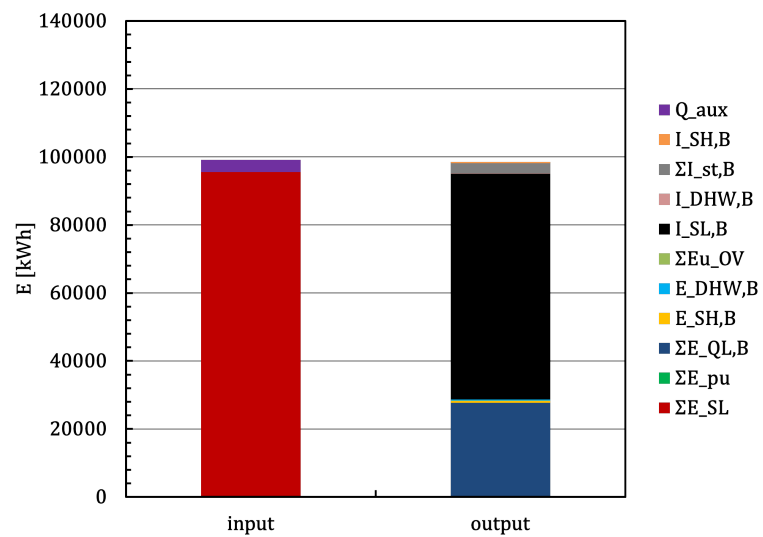


Figure A.3: Annual exergy balance of the overall system in Version B

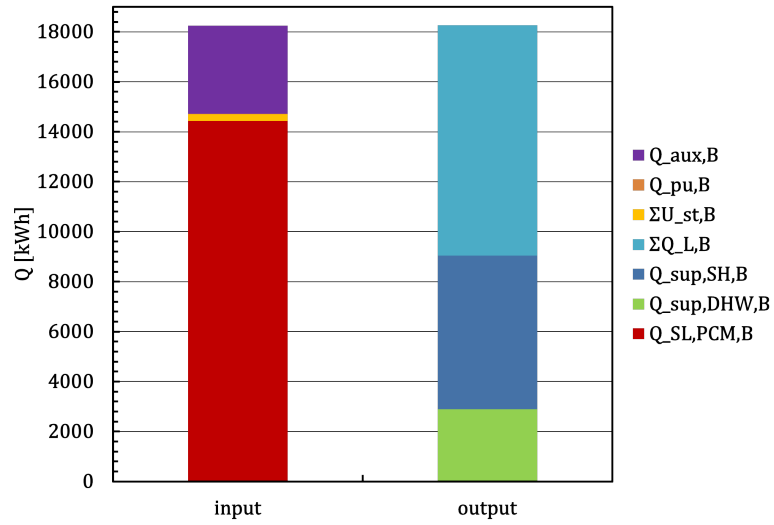


Figure A.4: Annual energy balance of the combined storage in Version B

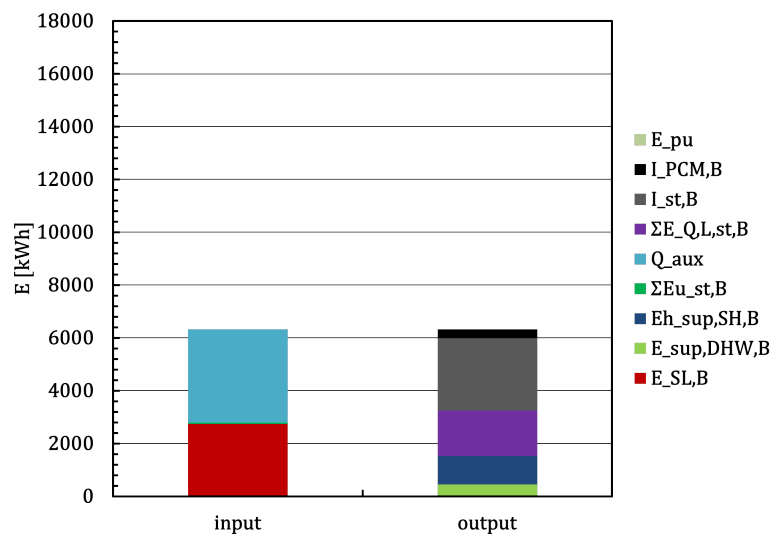


Figure A.5: Annual exergy balance of the combined storage in Version B

Zürich

Location name

47.37

Latitude [°N]

8.539

Longitude [°E]

413

Altitude [m a.s.l.]

III, 3

Climate region

Standard

Radiation model

Standard

Temperature model

Perez

Tilt radiation model

2000–2009

Temperature period

1986–2005

Radiation period

Additional information

Uncertainty of yearly values: Gh = 3%, Bn = 6%, Ta = 0,5 °C

Trend of Gh / decade: 2,0%

Variability of Gh / year: 5,2%

Radiation interpolation locations: Reckenholz (7 km), Zuerich-Kloten (12 km), Zuerich-SMA (2 km), Waedenswil (19 km), Buchs-Suhr (35 km), Taenikon (30 km)

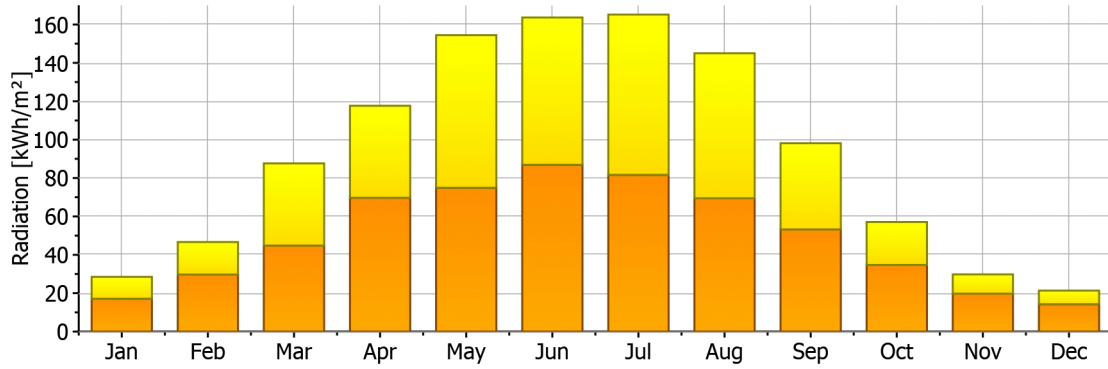
Temperature interpolation locations: Zuerich-Kloten (12 km), Waedenswil (19 km), Buchs-Suhr (35 km), Schaffhausen (36 km), Zuerich-SMA (2 km), Taenikon (30 km)

Month	G_Gh	G_Bn	G_Dh	Lg	Ld	N	Ta	Td
	[W/m2]	[W/m2]	[W/m2]	[lux]	[lux]	[octas]	[C]	[C]
January	38	52	23	4118	2836	7	2.0	-2.2
February	69	66	44	7456	5189	6	3.0	-1.7
March	118	114	60	12628	7285	6	5.6	0.7
April	163	120	97	17770	11530	6	9.3	3.7
May	208	173	101	22730	12376	6	13.9	8.6
June	227	173	121	25020	14890	5	17.5	11.7
July	222	183	110	24515	13853	5	18.5	12.9
August	195	167	93	21562	11688	5	18.4	13.2
September	136	118	74	15157	9177	6	14.8	10.3
October	77	70	47	8565	5850	6	10.9	7.5
November	41	43	27	4616	3468	7	5.6	2.2
December	29	36	19	3182	2351	7	2.7	-1.1
Year	127	110	68	13943	8374	6	10.2	5.5

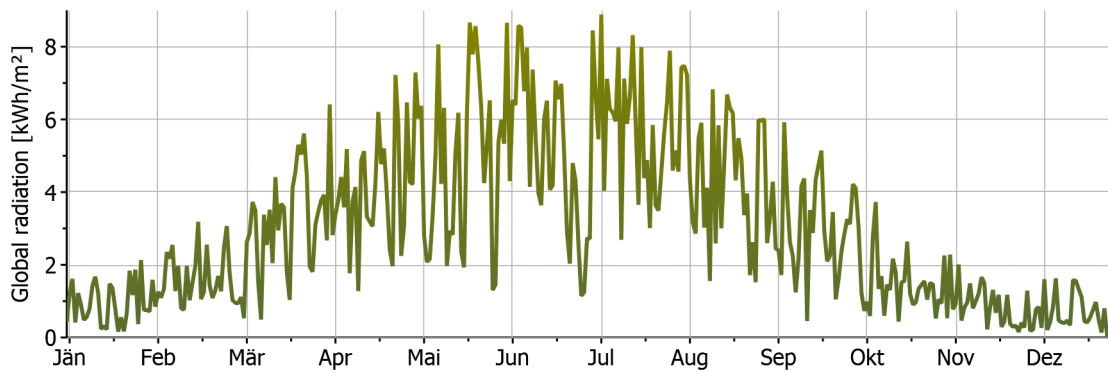
Month	RH	p	DD	FF
	[%]	[hPa]	[deg]	[m/s]
January	73	965	232	3.2
February	71	965	220	3.3
March	71	965	255	3.4
April	68	966	242	3.1
May	70	966	201	3.1
June	69	967	263	2.9
July	70	967	278	3.0
August	72	967	267	2.7
September	74	967	269	2.8
October	80	966	251	2.7
November	79	965	240	2.9
December	76	965	205	3.2
Year	73	966	243	3.0

Gh: Mean irradiance of global radiation horizontal
 Bn: Irradiance of beam
 Dh: Mean irradiance of diffuse radiation horizontal
 N: Cloud cover fraction
 Lg: Global luminance
 Ta: Air temperature
 RH: Relative humidity
 Td: Dewpoint temperature
 DD: Wind direction
 FF: Wind speed
 p: Air pressure

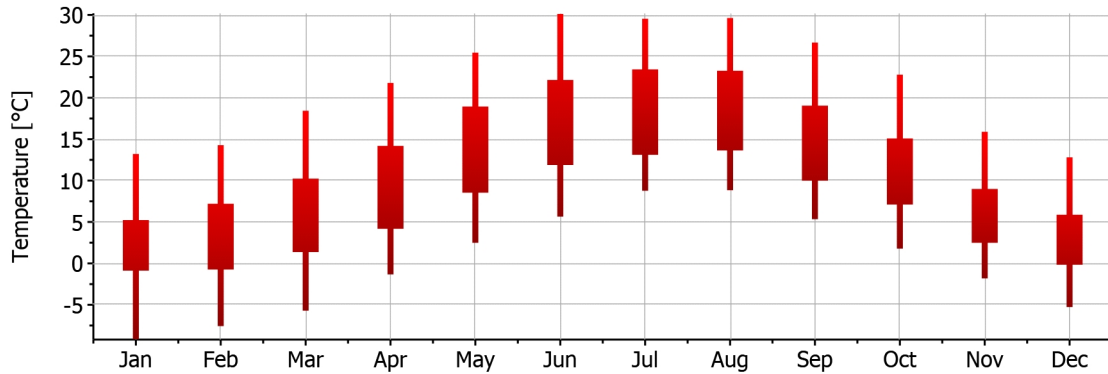
Monthly radiation



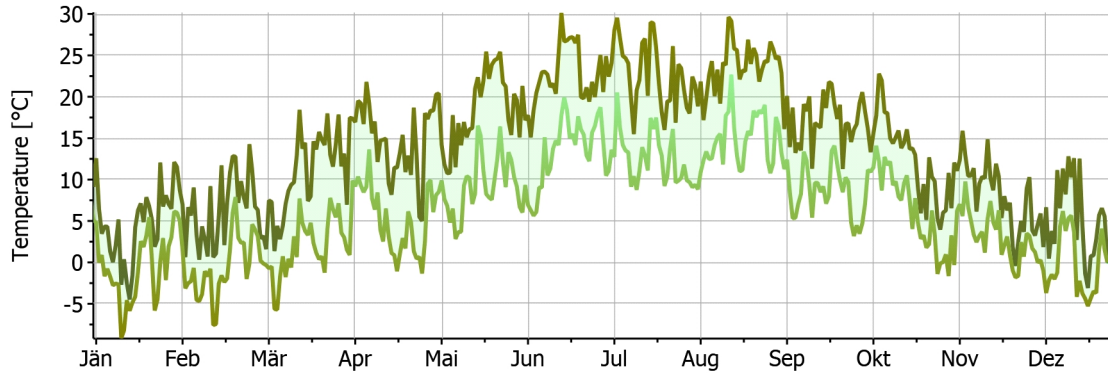
Daily global radiation



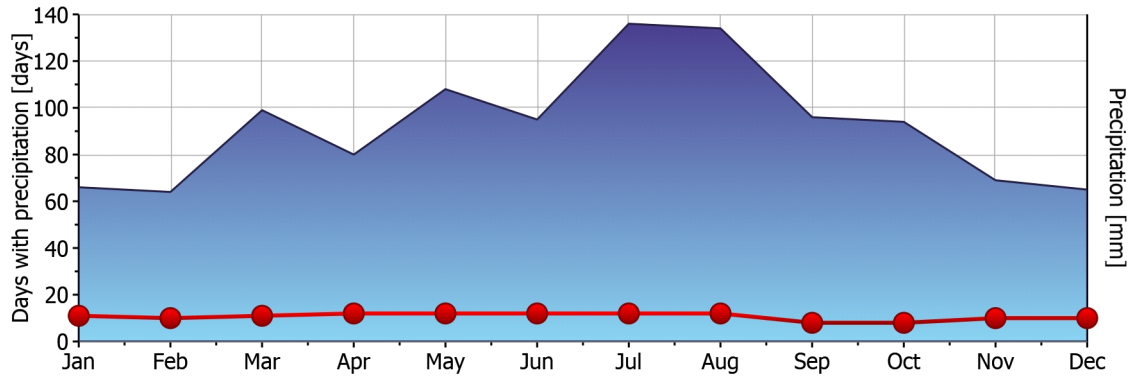
Monthly temperature



Daily temperature



Precipitation



Sunshine duration

